UCRL-LR-143344

Use of a Superconducting Tunnel Junction for X-Ray Fluorescence Spectroscopy

L. J. Hiller

March 6, 2001

U.S. Department of Energy
Lawrence Livermore National Laboratory

DISCLAIMER

This work was performed under the auspices of the U. S. Department of Energy by the University of California, Lawrence Livermore National Laboratory under Contract No. W-7405-Eng-48.

UCRL-LR-XXXXX
Distribution Category UC-XXX

Use of a Superconducting Tunnel Junction for X-Ray Fluorescence Spectroscopy

By

LAWRENCE JAMES HILLER
B.S. (Washington State University) 1992
M.S. (University of California, Davis) 1994

DISSERTATION

Submitted in partial satisfaction of the requirements for the degree of

DOCTOR OF PHILOSOPHY

in

Applied Science

in the

OFFICE OF GRADUATE STUDIES

of the

UNIVERSITY OF CALIFORNIA

DAVIS

Approved:

_____

_____

_____

Committee in Charge

2001

UCRL-LR-XXXXX
Distribution Category UC-XXX

[redacted] Superconducting Tunnel Junction for X-Ray Fluorescence Spectroscopy

By

LAWRENCE JAMES HILLER
B.S. (Washington State University) 1992
M.S. (University of California, Davis) 1994

DISSERTATION

Submitted in partial satisfaction of the requirements for the degree of

DOCTOR OF PHILOSOPHY

in

Applied Science

in the

OFFICE OF GRADUATE STUDIES

of the

UNIVERSITY OF CALIFORNIA

DAVIS

Approved:

_____

_____

_____

Committee in Charge

2001

Lawrence James Hiller
June 2001
Applied Science

[redacted] Superconducting Tunnel Junction for X-Ray Fluorescence Spectroscopy

Abstract

A superconducting tunnel junction (STJ) in combination with a superconducting absorber of radiation may function as a highly resolving x-ray spectrometer. Electronic excitations, or quasiparticles, are created when a superconductor absorbs an x ray and are detected as an excess tunnel current through the junction. The number of quasiparticles created and the magnitude of the excess current is proportional to the energy of the absorbed x ray. This is similar to existing semiconductor-based spectrometers that measure electron-hole pairs, but with 1000 times more excitations. The energy measurement therefore can be up to 30 times more precise with a superconducting detector than with a semiconductor detector.

This work describes the development and testing of an STJ spectrometer design for x-ray fluorescence applications. First, the basic principles of the STJ spectrometer are explained. This is followed by detailed simulations of the variance in the number of quasiparticles produced by absorption of an x ray. This variance is inherent in the detector and establishes an upper limit on the resolving power of the spectrometer. These simulations include effects due to the materials used in the spectrometer and to the multilayer structure of the device. Next, the spectrometer is characterized as functions of operating temperature, incident x-ray energy, and count rate. Many of these tests were performed with the spectrometer attached to a synchrotron radiation port. Finally, example x-ray fluorescence spectra of materials exposed to synchrotron radiation are presented. These materials are of interest to semiconductor processing and structural biology, two fields that will benefit immediately from the improved resolving power of the STJ spectrometer.

Table of Contents

DISCLAIMER

This work was performed under the auspices of the U.S. Department of Energy by the University of California, Lawrence Livermore National Laboratory under Contract W-7405-ENG-48.

This work was partially performed at SSRL which is operated by the U.S. Department of Energy, Office of Basic Sciences.

Acknowledgements

First and foremost I must offer my heartfelt thanks to three individuals. First I must thank my research advisor, Simon Labov. This thesis could not have been completed without his patience and infectious enthusiasm. I also must single out the support of Carl Mears, who took on the role of mentor. He taught me the arcana of ultra-low-temperature experimentation and the ins-an-outs of superconductivity. Finally, I must also thank my graduate advisor, Stephen Cramer. Again for his patience, and also for creating the motivation and opportunity to test our work at SSRL's synchrotron. His influence not only determined the ultimate form of this thesis, but also had a profound effect on the course of our entire research program.

Of my co-workers, I wish to offer special thanks to Matthias Frank and Stephan Friedrich. These two individuals have actively pursued the theme of this thesis, the application of superconducting tunnel junction technology to industrial and biochemical analysis. The device characterizations and analysis demonstrations performed at the synchrotron could not have been completed without their efforts. Adapting our cryogenic detectors for use at the synchrotron was not an easy project; the construction and testing process was often tedious, stressful, and subject to the interfering acts of evil, unseen gremlins.

Given the stressful and tedious nature of performing experiments at the synchrotron, I have to make special mention of the contributions of my co-workers Harry Netel, John Kipp, and in particular, Hans le Grand. These individuals made life easier for all of us by shouldering some of the burden of monitoring these experiments. Special thanks goes to Jeff Moore and Curt Troxel of SSRL for their patience and understanding for the neophyte beamline users. I also give thanks to all of members of the SSRL technical support staff and the user support staff, who have made SSRL probably the best such facility at which to work.

I wish to thank Jan Batteux and Dennis Carr for their technical support. They all-too-often were given a simple sketch, from which they produced beautiful machine drawings and precision machine parts. I also wish to thank Ida Hartmann, Christie Shannon, and others on the administrative staff at LLNL for their support and their ability to navigate the bureaucracy of such a large organization. Finally, I thank Andy Barfknecht and Conductus, Inc. for producing the actual devices around which this thesis is based.

wavelengths in different directions, which are detected with a spatially-resolving detector. A particular x-ray wavelength is often referred to as an *x-ray line* from the historical use of photographic film in this configuration. EDS instruments absorb every x ray and output an electrical signal that is proportional to the x-ray energy. The spectrum is the histogram of the heights of these electrical signals. This process is illustrated in figure 1.1. The STJ spectrometer is an energy-dispersive spectrometer.

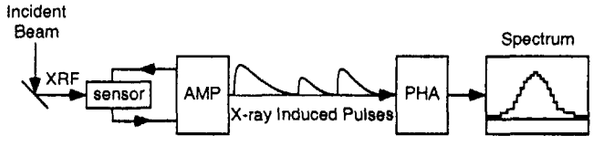

Figure 1.1: Illustration of x-ray fluorescence spectroscopy using an energy-dispersive spectrometer. An incident beam of either electrons or x rays strikes a target, which produces x-ray fluorescence (XRF). A sensor absorbs the fluorescent x rays. An amplifier and bias circuit (AMP) measures a change in the sensor and outputs an electrical pulse for each x-ray photon absorbed by the sensor. The pulses vary in size according to the x-ray energy, and also fluctuate due to noise in the spectrometer. A pulse-height analyzer (PHA) measures the height of each pulse and constructs a histogram of pulse heights. Each monochromatic x-ray energy is represented by a gaussian-shaped peak in the spectrum.

Neither WDS nor EDS instruments can determine the wavelength or energy with infinite precision. A monoenergetic x-ray beam will be represented by a peak in the spectrum. If the histogram bin size is sufficiently small, the peak will be distributed over several bins with an approximately gaussian shape. The precision of the wavelength or energy measurement can be characterized by the full-width at half maximum (FWHM) of the peak, and is expressed as the energy width ΔE_{FWHM} or the wavelength width $\Delta\lambda_{FWHM}$. The figure-of-merit for spectrometers is the *resolving power*, $E/\Delta E_{FWHM}$ or $\lambda/\Delta\lambda_{FWHM}$, where E and λ are the energy and wavelength of the x ray. The term *resolution* may refer to either the width or the resolving power; however, it is understood that the qualified

term high-resolution refers to large values of resolving power and small values of width. In general, WDS instruments have very high resolving power but very low efficiency. Until recently, EDS instruments have not had the high resolution of WDS. But, they have much greater efficiency.

X rays are not monoenergetic in practice. Fluorescence targets are composed of many elements, and the individual elements themselves emit many different x-ray lines which tend to be grouped into *multiplets*. As a result, a typical spectrum will contain multiple peaks from different elements, and each peak may be composed of many multiplet lines. The finite peak width causes lines with similar energy to overlap and merge. These lines can sometimes be separated by fitting a combination of multiple gaussian distributions to the measured line shape. If the lines are too close together, or one line is much more intense than the other, the confidence in the fit becomes unacceptably small. The ability to detect a weak line can be improved by increasing the measurement time, but at some point the time required becomes prohibitive. The only practical solution is to reduce the overlap by improving the detector resolving power. The EDS systems in common use today are near the fundamental resolution limit. The resolving power of these EDS systems is particularly poor in the soft x-ray energy range, 0.1 – 2.0 keV, typically being about 5 – 10. In the past, the only solution is to switch to a WDS system. Now, new technology such as the STJ spectrometer offers a high-resolution EDS solution.

WDS systems are constructed around a crystal or grating which diffract x rays of differing wavelengths at different angles. These typically operate over a range of wavelengths determined by the crystal lattice spacing and the grating line spacing,

Chapter 1

Introduction

X-ray fluorescence spectroscopy (XFS) is a valuable analysis tool. It can detect the presence and concentrations of elements in an analyte sample, and can do so non-destructively. It can probe the electron structure of atoms to explore physical chemistry. For these reasons, it is widely used in industry, geology, environmental monitoring, and biochemistry. This thesis examines the potential application of a new technology that greatly enhances the capabilities of XFS, with emphasis on industrial and biological analysis. This new technology is the superconducting tunnel junction (STJ) x-ray spectrometer.

XFS is an important tool in semiconductor manufacturing. Many semiconductor microstructures must have a precise chemical composition to function properly. Also, modern integrated circuits are becoming increasingly sensitive to contamination as the feature density increases and the feature size decreases. Typically, a wafer, either processed or blank, is examined in an electron microscope. The microscope can image the wafer surface or the processed microstructures. Then, the electron beam can be directed to a particular structure, or a particle of contamination. The electron beam excites the atoms in the structure or particle, which emit characteristic x rays. These x rays are collected and analyzed to determine the components of the microstructure or particle being examined.

Biochemists use x rays to study proteins and enzymes. Many such biological molecules, called *metalloproteins*, contain metal atoms that are crucial to the biological function of the molecule. X rays interact with the electrons of an atom. Many of these electrons are also involved in the chemical bonding of the atom to its neighbors. The presence of chemical bonds alters the states of these electrons. The absorption and fluorescence of x rays by an atom are therefore affected by the chemical bonds, or more generally, the chemical environment of an atom. Other techniques, such as nuclear magnetic resonance (NMR), are also sensitive to the chemical environment of atoms. However, NMR measures averaged properties of the molecule, or, at best, averaged properties of the element being studied. X-ray absorption spectroscopy (XAS), however, can be specific to an individual atom in the molecule. The electronic structure of that atom can be examined in detail as the molecule proceeds through different stages of its biological function. It is very difficult to determine the amount of absorption by the low-concentration atoms of interest in biological molecules, so the absorption is calculated by the x-ray fluorescence that follows.

The goal of XFS is to measure the distribution, or *spectrum*, of x-ray wavelengths or energies emanating from a fluorescent x-ray source. XFS is performed using two classes of instrument: wavelength-dispersive spectrometers (WDS) and energy-dispersive spectrometers (EDS). WDS instruments typically use Bragg diffraction to select a very narrow band of x-ray wavelengths from the beam of fluoresced x-ray photons and count the number of photons passed. The spectrum of x-ray wavelengths is calculated by stepping through different wavelengths. The spectrum is the histogram of count rates at each wavelength. Alternatively, a diffractive optical element may disperse different

Thermal detectors, or *microcalorimeters*, measure the temperature increase of a low-heat-capacity material when an x-ray is absorbed. These detectors are sensitive to phonons or conduction electrons, and the typical excitation energy is on the order of 1 – 10 μK. Thermal detectors have the best energy resolution, but must be operated at the lowest temperatures. The earliest microcalorimeters were dielectric or superconducting[a] absorbers coupled to silicon- or germanium-based thermistors. The conductivity of a thermistor varies substantially with temperature and functions as a sensitive sensor of the absorber temperature. The semiconductor thermistor is typically operated with a constant bias current and the voltage drop is measured. A recent advance is the development of the voltage-biased superconducting transition-edge sensor (TES). The thermistor has been replaced by a superconducting[a] film whose temperature is held at the transition between the superconducting and normal states. The resistance of the film is extremely sensitive at this point. When kept far out of equilibrium with a much colder bath by a constant voltage bias, the TES will automatically regulate its temperature on the steep transition. The change in temperature caused by an absorbed x ray will cause a change in the bias current, which is measured by an inductively coupled SQUID-based current amplifier. The TES microcalorimeter has exceptionally good low-energy x-ray resolving powers approaching 1000. However, current operating schemes require the microcalorimeter to return to its steady-state temperature before absorbing another x ray. A typical exponential time constant for this cooling is 200 μs. [4]

[a] These superconductors are conventional superconductors. Low temperature operation cannot be avoid by using "high-temperature superconductors" because thermal fluctuations must be kept small for high resolving power. The low temperature, rather than the superconductivity, is the key detail.

The STJ detector is a superconducting analogue to a semiconductor detector. Since it is sensitive to electronic excitations with energies much greater than the average thermal excitation, it is considered an athermal detector. The STJ is a thin-film tunnel junction composed of two superconducting[a] electrodes separated by a thin insulating barrier of aluminum oxide. The energy of the absorbed x ray breaks bound, superconducting Cooper pairs of electrons into unbound electron-like excitations, called *quasiparticles*. When the junction is biased, these quasiparticles tunnel to create a measurable current. Since the energy required to break a Cooper pair is approximately 1 meV, 3000 times less than the energy required to create and electron-hole pair, approximately 10^6 quasiparticles are created. This reduces the significance of both the external electronic noise and the internal quasiparticle fluctuations. The resolving power of the STJ spectrometer developed at LLNL is typically 100 – 200. [5] The duration of the current pulse created by LLNL STJ sensors is 2 – 5 μs, or about 100 times faster than the TES microcalorimeter. In the LLNL design, the superconducting electrode is also the x-ray absorber. Since this electrode is a thin film of niobium, the sensor is efficient only below 1 keV. [5]

This summarizes the primary technology candidates for XFS in soft x-ray energy band 0.3 – 2 keV. A representative sample of the energy widths for crystal, semiconductor, TES, and STJ are plotted in figure 1.2. Semiconductor spectrometers, limited by electronic noise, have a FWHM of about 100 eV at all energies. The LLNL STJ spectrometer FWHM is 5 – 25 eV, and is limited by a combination of intrinsic fluctuations, external noise, and in some cases, spatial dependence. The result for a TES

[a] See footnote a on the previous page.

respectively. This range can be extended by monitoring multiple diffraction angles with multiple photon counters or an imaging detector. Originally, quartz and mica crystals were used to diffract hard x-rays. However, lower energies require larger crystal spacings. Lithium fluoride crystals may be used to diffract x rays with energies as low as 4 keV. Below that, organic crystals pentaerythritol (PET) and thallium acid phthalate (TAP) may be used to diffract x rays with energies as low as 0.5 keV. Synthetic multilayers of different materials may be constructed to diffract even lower-energy x rays. However, these multilayers are usually optimized for only a very narrow energy range. The resolving power of WDS systems can be as high as 10,000.

All crystal spectrometers and x-ray grating spectrometers have very low efficiencies. This can be improved by bending the crystal or grating or by varying the line spacing along the length of the grating, so that the x-rays are focused on the detector while at the same time maintaining the diffraction condition. The effective efficiency is reduced if the grating or crystal must be scanned through a broad range of wavelengths.

Semiconductor EDS systems are now more popular than WDS systems because of their broad-band capability, ease-of-use, and relatively low cost. Semiconductor EDS detectors are generally constructed from lithium-drifted silicon (Si(Li)) or high-purity germanium (HPGe, or simply Ge). The detector is doped to form a p-type/intrinsic/n-type diode. When reversed-biased, the intrinsic region is depleted of charge carriers. When the intrinsic region absorbs an x ray, several thousand electron-hole pairs are created. These electrons and holes are separated by the reverse-bias electric field before they recombine and are collected in the electrodes. The total charge collected is proportional to the number of electron-hole pairs created, which in turn is proportional to

the energy of the absorbed x ray. The charge collection process typically takes a few hundred nanoseconds. The signal generated by 1000 electrons is very small, so the detector resolution at low energies is limited by the noise of the electronics. The actual number of electron-hole pairs also fluctuates from absorption to absorption, which is equivalent to an additional noise source. Semiconductor EDS detectors have a further disadvantage for low energy x rays. Low energy x-ray photons are absorbed very close to the surface electrode in what is termed the *dead-layer*. [1, 2] Electron-hole pairs created there frequently recombine before being collected, resulting in reduced efficiency, reduced signal size, and non-linearity.

The energy resolution of an EDS detector is fundamentally determined by its sensitivity to changes in the internal energy of the absorber. The intrinsic error in the energy measurement scales with the square root of the basic energy scale for the excitations to which the detector is sensitive.. For silicon and germanium detectors, this basic energy scale is the average energy to create an electron-hole pair, which is about 3.5 eV. Improved resolution is possible if the detector can be made sensitive to smaller quanta of energy. [3] Sensitivity to smaller quanta requires the operating temperature to also be reduced, otherwise thermal excitations will contribute too much noise to the signal. High-resolution silicon and germanium detectors operate at the temperature of liquid nitrogen, 77 K, to reduce the number of thermally created electron-hole pairs to negligible levels. Very-high-resolution detectors must operate at still lower temperatures, below 1 K, or even 0.1 K. These detectors are called cryogenic detectors[4], and may be grouped into two categories: thermal and athermal detectors.

[4] Although liquid nitrogen is a cryogen, detectors operating at 77 K are not included, as the engineering and physics of materials below 1 K is substantially different.

Chapter 2

Detector Principles

2.1 Introduction

The operating principle of an STJ spectrometer is similar to that of a semiconductor ionization spectrometer. As in a semiconductor spectrometer, the STJ operates by measuring the quantity of electronic excitations created from the energy of an absorbed x-ray photon. In a semiconductor detector, these excitations are electron-hole pairs. In the STJ, the absorbed energy breaks bound electron pairs, or *Cooper pairs*, producing weakly-interacting, nearly-free single particles, or *quasiparticles*. The STJ gains an advantage over semiconductors because the energy to create quasiparticles is 1000 times less than the energy to create electron-hole pairs. The STJ spectrometer can measure the greater number of excitations with greater relative accuracy. Both detectors must be cooled so that the average thermal phonon energy is a tiny fraction of the creation energy for an excitation. Both detectors measure the excess current or charge of the excitations. However, a semiconductor detector is a resistive medium, and can support an electric field. This field will draw the electrons and holes to the electrodes and produce a measurable current. A superconductor will not support a DC electric field. The tunnel junction provides a means for measuring these quasiparticles, but there is no direct method to bring the quasiparticles to the junction. LLNL STJ detectors solve this problem through a combination of layered geometry and material selections, which

causes almost all of the created quasiparticles to become confined in a trap at the tunnel barrier. [9, 10]

This chapter provides a foundation for the theoretical modeling and experimental results in the following chapters. The construction of the LLNL STJ detector, and how this construction results in a measurable signal for spectroscopy, is described,. The behavior of quasiparticles in an STJ will be qualitatively described here, and elaborated upon in later chapters. Finally, the phenomenon of quasiparticle tunneling is described, and the electrical properties and operation of the tunnel junction explained.

2.2 Bardeen-Cooper-Schrieffer (BCS) Theory of Superconductivity

The original BCS theory, which is applicable to most low-temperature superconductors, describes a system where electrons with opposite spin and momentum feel a weak attractive potential and become bound. This attractive potential arises from the positive charge of ion cores that have been attracted to a passing electron. If this attractive potential is greater than the screened repulsive potential between electrons, and thermal fluctuations do not disrupt the correlated motions of the ions and electrons, superconductivity can result. While it is not an absolute requirement, interactions between electrons of opposite spin and momentum are strongly favored due to phase space considerations.

The theory of BCS and its extensions has provided an excellent description for most low-temperature superconductivity. A brief description of the foundations of BCS is presented here to support the theoretical work in this thesis. For further details the reader should consult one of many reference works. [11] Since they will appear later, the BCS formulation using fermion creation and destruction operators will be introduced

x-ray microcalorimeters developed at NIST is shown with a FWHM of 4.5 keV at 6 keV. Finally, the performance for TAP, PET, and LiF crystals is shown, which has a strong dependence on energy.

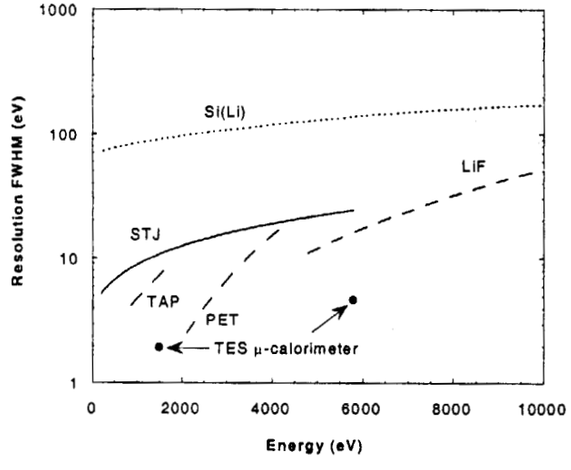

Figure 1.2: Plots of typical peak width as a function of energy for the EDS technologies: lithium-compensated silicon (Si(Li)), [6] LLNL STJ (STJ), [5] NIST TES (TEST), [7, 8] and the WDS crystals: lithium fluoride (LiF), pentaerythritol (PET), and thallium acid phthalate (TAP). [6]

The STJ spectrometer is a maturing technology that is ready to be applied to demanding XFS applications. This thesis examines the qualifications of the STJ spectrometer, characterizes its properties and performance, and demonstrates actual measurements of x-ray fluorescence at a synchrotron radiation light source. The thesis is structured as follows. Chapter 2 describes the construction of the LLNL STJ detector. It will reviews the basic physics of superconductivity, with emphasis on the properties of

quasiparticles, as a foundation for the theoretical work in chapter 3. Chapter 3 re-examines the theory behind estimates for the theoretical limiting resolution of the STJ spectrometer, i.e. the intrinsic fluctuations in the number of quasiparticles produced. Specifically, it examines the role of absorber material selection and the multilayer structure of the LLNL STJ absorber. Chapter 4 describes the equipment and experimental setup for the experiments described in chapters 5 and 6. Chapter 5 describes many characterizations of the STJ detector, including energy resolution, energy linearity, temperature sensitivity, and count rate dependence. It also addresses the use of current-following amplifiers rather than the charge-integrating amplifiers typically used in EDS. Chapter 6 presents the fluorescence spectra of several industrial and biological samples, and examines some of the difficulties in acquiring them.

The eigenvalues of the model hamiltonian are the ground and excited states of the superconducting system. The remaining parameter, b_k, is the thermal and quantum mechanical average of the $c_{-k\downarrow}c_{k\uparrow}$ operators over these states. By requiring this system to be self-consistent, b_k and Δ_k are found to be

$$b_k = u_k v_k^* [1 - 2f(E_k)], \text{ and} \qquad 2.9$$

$$\Delta_k = -\sum_l V_{kl} u_l v_l^* [1 - 2f(E_l)] = -\sum_l V_{kl} \Delta_l [1 - 2f(E_l)]/2E_l . \qquad 2.10$$

The function *f(E)* is the Fermi function or a non-equilibrium quasiparticle distribution. Typically, the interaction potential V_{kl} is taken to be constant a constant attractive potential up to a cut-off energy ω_{max} which is of the order of the Debye energy, and zero above it. Thus, the gap energy Δ_k is taken to be constant and real. Given an estimate for the magnitude of the pairing potential, the transition temperature T_c and the gap Δ can be calculated directly from equation 2.10, as well as the changes in Δ when the quasiparticle distribution is far from equilibrium.

The energy of an unpaired quasiparticle is given by equation 2.6. This dispersion curve for quasiparticles is shown in figure 2.1. This dispersion curve has two immediate consequences. First, the quasiparticle density of states, $N_s(E)$, which is proportional to $(dE/dk)^{-1}$, is singular at the gap energy. Second, the group velocity which is proportional to (dE/dk), goes to zero at the gap.

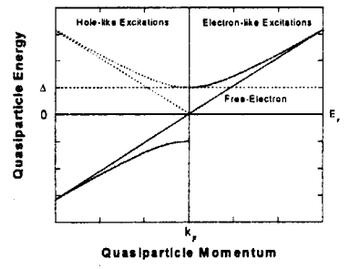

Figure 2.1: Dispersion curve for quasiparticles. The BCS pairing interaction creates an energy gap at the Fermi energy for quasiparticle excitations (solid). Because quasiparticles are a superposition of electron and hole states, and always have positive energy relative to the Fermi energy, it is conventional to reflect the quasi-hole branch about the Fermi energy.

$$\frac{N_s(E)}{N(0)} = \begin{cases} 0 & E < \Delta \\ \dfrac{E}{\left(E^2 - \Delta^2\right)^{1/2}} & E > \Delta \end{cases} \qquad 2.11$$

$$v_g(E) \cong \frac{v_F}{N_s(E)}. \qquad 2.12$$

The electron branch *($|k| > k_F$)* and hole branch *($|k| < k_F$)* can be considered to be equivalent for most purposes. Their dispersion curves are identical to first order. The band structure of the nearly-free electrons will cause some differences at energies that are typically far from the Fermi energy. Also, in certain situations the quasi-electron and quasi-hole populations could be different, a situation called *branch imbalance*. The creation of quasiparticles by an energetic photoelectron occurs at energies where quasi-electrons and quasi-holes have different densities of states, so the creation of one will be favored over the other. Also, quasi-holes and quasi-electrons tunnel differently, so

here. The operator $c_{k\sigma}$ removes an electron with crystal momentum k and spin σ to the current electron system, while $c^{+}_{k\sigma}$ adds an electron.

BCS theory first begins by describing the system with a reduced hamiltonian that has omitted terms that are not important for superconductivity:

$$H = \sum_{k\sigma} \varepsilon_k c^{*}_{k\sigma} c_{k\sigma} + \sum_{kl} V_{kl} c^{*}_{k\uparrow} c^{*}_{-k\downarrow} c_{-l\downarrow} c_{l\uparrow} \text{ , with} \qquad 2.1$$

$$\varepsilon_k = \frac{\hbar k^2}{2m} - E_F . \qquad 2.2$$

This is a pair of summations over Bloch states with crystal momentum k and spin σ. The first is the kinetic energy relative to the Fermi energy. The second is the interaction energy for two electrons with opposite spins to scatter from states $|\pm l\rangle$ to $|\pm k\rangle$, described by the interaction potential V_{kl}. It is recognized that since these are correlated states, $c_{-k\downarrow} c_{k\uparrow}$ and similar operators will not average to zero, but to a macroscopic expectation value $b_k = \langle c_{-k\downarrow} c_{k\uparrow} \rangle_{av}$, with small fluctuations $c_{-k\downarrow} c_{k\uparrow} - b_k$. We can make this substitution, keeping only the lowest order terms to obtain a model hamiltonian,

$$H_m = \sum_{k\sigma} \varepsilon_k c^{*}_{k\sigma} c_{k\sigma} - \sum_{k} \Delta_k c^{*}_{k\uparrow} c^{*}_{-k\downarrow} + \Delta^{*}_k c_{-k\downarrow} c_{k\uparrow} - \Delta^{*}_k b_k , \qquad 2.3$$

and the interaction energy

$$\Delta_k = -\sum_{l} V_{kl} b_l . \qquad 2.4$$

This hamiltonian can be diagonalized transforming the electron operators into a superposition of quasiparticle fermion operators with momentum k and orthogonal spin states 0 or 1:

$$\begin{aligned} c_{k\uparrow} &= u_k \gamma_{k0} + v^{*}_k \gamma^{+}_{k1} \\ c^{*}_{-k\downarrow} &= -v_k \gamma_{k0} + u^{*}_k \gamma^{+}_{k1} \end{aligned} \text{, where} \qquad 2.5$$

$$E = \sqrt{\varepsilon_k^2 + \Delta_k^2} \text{ , and} \qquad 2.7$$

$$|v_k|^2 = 1 - |u_k|^2 = \frac{1}{2}\left(1 - \frac{\varepsilon_k}{E_k}\right). \qquad 2.7$$

At this point, we can identify for the quasiparticle state with momentum k the following energy terms: ε_k is the kinetic energy relative to the Fermi energy, E_k as the total energy also relative to the Fermi energy, and Δ_k is defined to be the gap energy, which is the minimum energy required for an electron to overcome the pairing potential and become a free excitation. The resulting hamiltonian describing the quasiparticle excitations of the superconductor is:

$$H_m = \sum_{k} \left(\varepsilon_k - E_k + \Delta_k b^{*}_k\right) + \sum_{k} E_k \left(\gamma^{*}_{k0} \gamma_{k0} + \gamma^{*}_{k1} \gamma_{k1}\right) \qquad 2.8$$

The first term is the ground state energy, which differs from the normal state by the energy of condensation. If the interaction potential is attractive, then this will always be lower than in than normal state when below a certain temperature, the transition temperature. The second term is the energy of excited states γ_{k0} and γ_{k1}, both of which have the energy E_k.

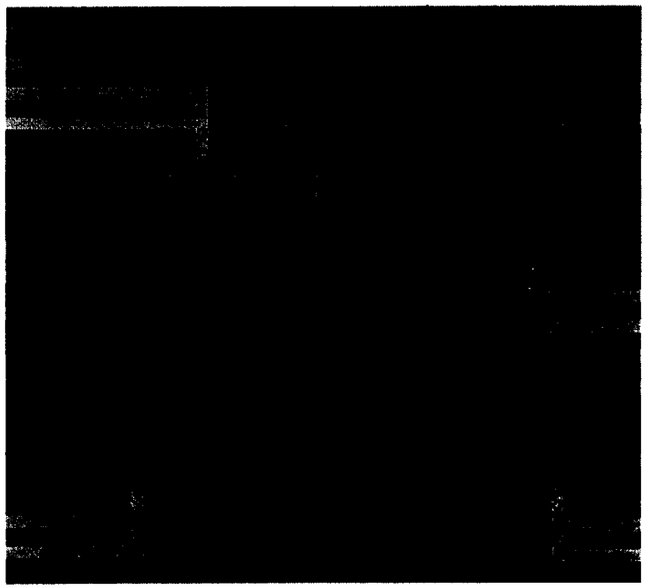

Figure 2.3: Phase-contrast micrograph of a set of LLNL STJ detectors with varying sizes to study volume and capacitance effects. The junctions measure 71 × 71 μm^2, 100 × 100 μm^2, 141 × 141 μm^2, and 200 × 200 μm^2.

The full-wafer process yields about 400 3 mm × 5 mm chips. These chips contain variations on the basic detector design, including "diamond" and "football" junction shapes, optional ground planes, and detector arrays, as well as diagnostic constructions. In all designs, the detector absorbers are the same size and shape as the tunnel junction. The combined absorption efficiency of the two layers is 99.5% at 500 eV, 80% at 1 keV, and 10% at 6 keV. The x rays are primarily absorbed in the niobium. The adjacent aluminum has a lower energy gap than the niobium, and can trap quasiparticles that relax to the lower gap energy. Later designs contact the top niobium through a 5 μm diameter via, and contact the bottom niobium through a 5 μm constriction to reduce quasiparticle escape into the wiring layers.

2.4 Excited Quasiparticle Lifecycle

The lifecycle of the athermal quasiparticles begins with the ejection of an energetic photoelectron and additional Auger electrons in the absorber and ends with the recombination of all excess quasiparticles into bound Cooper pairs. In between those events are the quasiparticle cascade in which approximately 60% of the photon energy is converted into quasiparticles, the diffusion of the quasiparticles to fill the detector volume, and the trapping and tunneling of quasiparticles. This cycle is depicted in figure 2.4.

The creation of the quasiparticle population begins with the absorption of a photon by a niobium atom with the emission of an L- or M-shell electron and Auger electrons. The electrons deposit their energy as they travel through the absorber and create additional free electrons. The range of this photoelectron is very short at soft x-ray energies, only a few nanometers. Because the absorber is constructed from a thin film,

branch imbalance can be created with tunnel junctions with very high tunnel rates. Similarly, a branch imbalance can be detected with a tunnel junction.

A quasiparticle can elastically scatter from a quasiparticle state on one branch to a state with the same energy on the other branch. In general, branch imbalance relaxes on a very fast time-scale, on the order of 100-1000 ps. [12, 13] This is ~1000 times faster than the tunneling process in LLNL STJ devices. Therefore the effects of branch imbalance will not be included in this thesis.

2.3 Detector Construction

The detectors were fabricated at Conductus, Inc. using a modification of their trilayer niobium-aluminum process. [14] Figure 2.2a is a cross-section of the final multilayer structure of the detectors. A four-inch silicon wafer with a thermal SiO_2 layer was coated with a niobium layer that was generally 240 nm thick. This was followed with an aluminum layer of 35, 50, 100, 200, or 400 nm thick. The wafer was then exposed to oxygen in a load-lock. This oxidation step typically exposed the wafer to 10 Torr O_2 for 30 minutes. A second layer of aluminum identical to the first is deposited over the oxide layer. Finally, a niobium layer that was generally 160 nm thick was deposited. All layers were deposited by sputtering and at no time were they exposed to the external atmosphere.

At this point, the wafer was masked and patterned into the desired junction shapes with photoresist as shown in figure 2.2b. The top niobium layer was removed by a reactive-ion etch. The aluminum layers were removed with a wet-etch. The bottom niobium layer was patterned into the base electrode and wiring layer and etched to the SiO_2. The wafer was then coated with up to 1 μm of SiO_2 which was deposited using

plasma-enhanced chemical-vapor deposition. Contacts to the top niobium layer were patterned and etched by ion-milling. In some devices the entire SiO_2 coating of the junction area was removed. A layer of niobium, also about 1 μm thick, was deposited, patterned, and etched into the top wiring layer. This wiring layer either made electrical contact to the counter electrode through either a 5 or 10 μm diameter hole, or completely covered the entire top layer to provide additional x-ray absorption efficiency. Figure 2.3 is a phase-contrast micrograph of several junctions. This fabrication process is mature and device properties are uniform across a single wafer and also between different wafers. For soft x-ray spectroscopy, we attempted to remove the remaining SiO_2. This last step is not precisely controlled and we believe it to be responsible for spectral artifacts on some wafers.

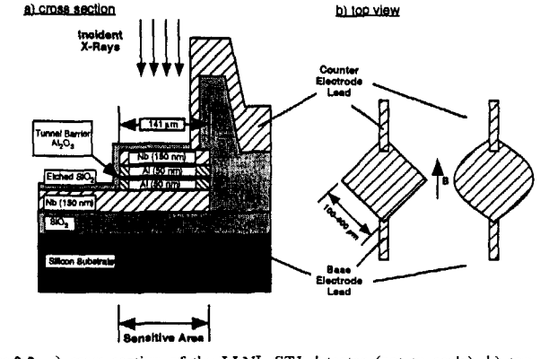

Figure 2.2: a) cross-section of the LLNL STJ detector (not to scale). b) top view of "diamond" and "football" junction shapes.

will reach the aluminum where they may be detected. In addition, a mechanism is identified in this thesis that may recover the energy lost due to possible gap suppression in our devices. These issues are discussed in chapter 3. Overall, the duration of the cascade is 100 ps – 1 ns.

Once the hot-spot decays, quasiparticles are free to diffuse. Those quasiparticles that diffuse near the reduced gap of a trap will almost immediately relax into the trap with the emission of a phonon if the trap is deep enough. Traditionally, this trapping stage has been considered to be completely separate from the cascade stage. However, the dimensions of the LLNL STJ are so small that, unless fully confined by the hot-spot, the quasiparticles will fill the detector volume before the cascade is complete. Some portion of the cascade will occur within the trap material, which has important implications for estimating the quasiparticle yield. This will also be discussed in chapter 3.

Each time a quasiparticle strikes the tunnel barrier, an *attempt*, it has a small chance of tunneling to the other side. Once trapped, the attempt frequency is increased by the ratio of the total volume to the trapped volume. In LLNL devices, this volume ratio ranges from a minimum of 360:200 to a maximum of 275:35. The trap also isolates quasiparticles from losses out the leads or from normal-state oxides on the surface. The typical time scale for tunneling is 0.5 μs.

Finally, the quasiparticles eventually recombine into Cooper pairs. This occurs when two quasiparticles release their energy in the form of a phonon, or relax individually into a deeper trap of normal metal or reduced superconductivity. This process occurs on a short time scale. However, the phonon produced by two recombining quasiparticles contains enough energy to break another Cooper pair, which usually

happens almost immediately. Thus, the effective lifetime of a quasiparticle is enhanced by a phonon trapping factor. Also, since each quasiparticle must combine with another to be lost, the loss rate for this mechanism is proportional to the quasiparticle density and inversely proportional to the trap volume. This mechanism is dominant when very high-energy x rays are absorbed. The loss rate into traps is independent of quasiparticle density, and is dominant when low-energy x-rays are absorbed. The effective lifetime for devices with 5 nm Al traps has been measured to be 2 μs.

2.5 SIS Tunneling Processes

As shown in section 2.2, quasiparticles are not pure electron states, but superpositions of electron and hole states. Because of this, quasiparticle tunneling produces some non-intuitive results that have no analog in normal metals or semiconductors. Also, some confusing but technically correct statements have been made in the literature regarding the hole-like nature of quasiparticles. A short but explicit derivation of SIS (superconductor-insulator-superconductor) tunneling will be given here to clear up any confusion.

The Hamiltonian for electron tunneling is simply represented by electron quantization operators of arbitrary but identical spin:

$$H = \sum_{k_1,k_2} T_{k_1k_2} c^*_{k_2} c_{k_1} + \text{c.c.} \qquad 2.13$$

In this Hamiltonian, $T_{k_1k_2}$ is the matrix element for an electron tunneling from the k_1 state in superconductor 1 to the k_2 state in superconductor 2. The complex conjugate represents the reverse tunneling process. The matrix element $T_{k_1k_2}$ is taken to be constant and symmetric over the small range of momenta relevant to SIS tunneling. The tunnel

there is a possibility of photo-electron escape at higher energies. Monte Carlo simulations have shown that this will not be observed below 5 keV for 200 nm niobium absorber. [15]

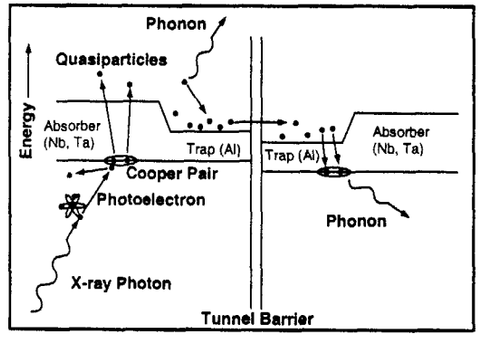

Figure 2.4: Lifecycle of excited quasiparticles. An x-ray photon is absorbed by a niobium atom. The emitted electrons break a large number of Cooper pair into single quasiparticle excitations. The quasiparticles diffuse into the aluminum, which has a lower gap. Quasiparticles can become trapped in the aluminum by emitting a phonon. The trap confines the quasiparticles near the tunnel barrier, through which they tunnel into an identical trap on the other side. Quasiparticles eventually recombine into Cooper pairs by emitting a phonon which escapes.

Electron-electron scattering continues to produce free electrons until the average electron energy relative to the Fermi energy is $(\Omega_D E_F)^{1/2} \sim 0.5$ eV [16] where Ω_D is the phonon Debye energy and E_F is the Fermi energy. At this point there is a small population of a few hundred free electrons. Now, the electron-phonon interaction comes to dominate the Coulomb interaction, and the electrons relax in energy by emitting phonons.

Each electron releases its remaining energy into 25-50 acoustic phonons with energies ~ Ω_D. These phonons are almost immediately absorbed by the dense Cooper

Pair sea. Each absorbed phonon producing two quasiparticles. It is likely one quasiparticle or both quasiparticles will have greater than 3Δ in energy, and each can emit a phonon which will again break more Cooper pairs. Recall that neither the photoelectrons nor the phonons could travel more than a few nanometers before creating more excitations. At this stage the entire process and all of the x-ray energy is confined within a very small volume of typically 0.1 μm^3, [17] colorfully termed the *fireball* or *hot-spot*. This hot-spot is characterized by slow growth and the possible suppression of superconductivity, resulting in the premature loss of quasiparticles. These effects are collectively termed the "hot-spot effect".

The hot-spot effect has several aspects. First, energetic phonons do not propagate very far, so the only means to reduce the energy density of the hot-spot is by quasiparticle diffusion. Second, quasiparticle diffusion is slower than electron diffusion in the normal state due to the dispersion near the gap, see again figure 2.1 and equation 2.6. Finally, the gap itself may be suppressed by the high effective temperature and/or the high quasiparticle density. Quasiparticles that are created near the reduced gap or have relaxed to the reduced gap may become trapped and never be detected by the tunnel junction.

There have been several approaches to modeling the hot-spot effect. [17, 18] It is, however, extremely difficult to verify these models. The hot-spot effect will not be modeled in this thesis. The simulations of the quasiparticle cascade in this thesis may be considered to be a limit in which the effects of the hot-spot are negligible (i.e. low photon energies). Since the size of the hot-spot is expected to comparable to the thickness of the STJ niobium layers, it is reasonable to expect that the majority of created quasiparticles

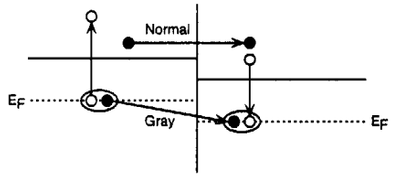

Figure 2.5: Simplified diagram of quasiparticle tunneling, which does not acknowledge the mixed electron-hole character of the quasiparticle. Electrons (filled circles) tunnel via the "normal" process from left to right, while holes (empty circles) "tunnel" via the "Gray" process from right to left. The inverse processes are obtained by reversing the arrows.

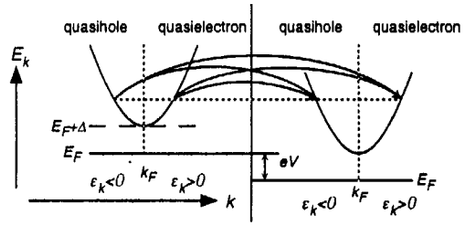

Figure 2.6: Expand view of "normal" tunneling illustrating the possibility of tunneling between branches. The quasiparticle energy E_k differs from the free electron energy relative to the Fermi energy, ε_k, with the existence of a superconducting gap.

The net tunneling current for the normal process and its inverse for a single spin, for identical superconductors and in the absence of branch imbalance is,

$$I_{\uparrow}^{(n)} = \frac{G_{nn}}{2e}\int_{\Delta}^{\infty} N_s(E+eV)N_s(E)\left[f_1(E)-f_2(E+eV)\right]\left(\sum_{k_1,k_2} u_{k_1}^2 u_{k_2}^2 \delta_{E,E_{k_1}}\delta_{E,E_{k_2}}\right)dE, \qquad 2.21$$

where $f_{1,2}(E)$ are the occupation distributions for quasiparticles in the two superconductors and $N_s(E)$ is the quasiparticle density of states normalized to $N(0)$, as defined in equation 2.11. Because u_k^2-$^1/_2$ is antisymmetric about k_F, the summation in

equation 2.21 is readily shown to be unity. The summation over $v_k^2 v_k^{\prime 2}$ for the Gray process is also unity. The net current including both processes and both spins, is 4 times equation 2.21. If $f_{1,2}(E)$ is the Fermi function for a given temperature, then this current is the thermal quasiparticle current.

The tunneling time for an SIS tunnel junction can be defined in the same manner as for the NIN. Since the net current includes tunneling from both electrodes, the tunneling rate must be calculated from total quasiparticle population n_{total}. [20] The total number of quasiparticles in *both* traps, including both spins and equal branch occupation is

$$Adn_{total} = 2Adn = 8AdN(0)\int_{\Delta}^{\infty} N_s(E)f(E)dE. \qquad 2.22$$

For sufficiently high bias, the thermal current can be approximated as

$$I_{th} = 2\frac{G_{nn}}{e}N_s(\Delta+eV)\int_{\Delta}^{\infty} N_s(E)f(E)dE, \qquad 2.23$$

and the quasiparticle tunneling rate is

$$\Gamma = \frac{I_{th}}{eAdn_{total}} = \frac{N_s(\Delta+eV)}{4e^2N(0)R_{nn}Ad}. \qquad 2.24$$

Thus, it is shown that the quasiparticle tunneling rate is half that of normal electrons. Various statements about this factor of two have appeared in the literature. Some general examples are:

1. Electrons tunnel. Holes don't.

current can be calculated using Fermi's Golden Rule. In a normal metal-insulator-normal metal junction, this simplifies to Ohm's law with a normal state conductance $G_{nn} = 1/R_{nn}$:

$$I_{nn} = VG_{nn}, \text{ where} \tag{2.14}$$

$$G_{nn} = (Ad)^2 |T|^2 N_1(0) N_2(0) \frac{4e^2\pi}{\hbar}. \tag{2.15}$$

In the above expression, A is the junction area, d is the thickness of the electrodes, T is the tunneling matrix element, and $N_{1,2}(0)$ is the single-spin density-of-states at the Fermi energy for electrode 1,2. It is convenient to define a tunneling rate Γ, according to equation 2.16. Given the density of electrons able to tunnel in the normal metal, equation 2.17, and the definition of current in terms of the tunnel rate, equation 2.18, the normal metal tunnel rate is obtained, equation 2.19.

$$\frac{dn}{dt} = -\Gamma n \tag{2.16}$$

$$n_{nn} = 2N(0)eV \tag{2.17}$$

$$I = e\Gamma A d n \tag{2.18}$$

$$\Gamma_{nn} = \left[2e^2 N(0) R_{nn} A d\right]^{-1} \tag{2.19}$$

To calculate how quasiparticle states tunnel, the electron tunneling Hamiltonian is transformed by substituting the Bogoliubov quasiparticle operators, equation 2.5 for the electron operators of a given spin.

$$\begin{aligned} H &= \sum_{k_1,k_2} T_{k_1k_1} \left(u_{k_1}\gamma_{\uparrow k_1} + v_{k_1}\gamma^*_{\downarrow -k_1}\right)\left(u_{k_1}\gamma^*_{\uparrow k_1} + v_{k_1}\gamma_{\downarrow -k_1}\right) + \text{c.c.} \\ &= \sum_{k_1,k_2} T_{k_1k_1} u_{k_2} u_{k_1} \gamma_{\uparrow k_2}\gamma^*_{\uparrow k} + T_{k_1k_{11}} v_{k_1} v_{k_1} \gamma^*_{\downarrow -k_2}\gamma_{\downarrow -k_1} + \text{c.c.} + \text{energetically disallowed terms} \end{aligned} \tag{2.20}$$

After expanding the product, the first term represents electron-like quasiparticles tunneling from superconductor 1 to superconductor 2, and is called the "normal" process. The second term represents hole-like quasiparticles tunneling from superconductor 2 to superconductor 1, and is called the "Gray" process. [19] The Gray process is *not* the inverse of the normal process. These two processes are illustrated in figure 2.5. The Gray process transfers charge in the same direction as the normal process, but the excitation travels in the opposite direction. This is allowed because the number of Cooper pairs in each electrode also changes. Despite appearances, the normal and Gray processes are of the same order, and occur at identical rates, in symmetric junctions, with no branch imbalance.

The simplified diagram ignores the mixed character of quasiparticles. The two processes in figure 2.5 actually represent eight different processes corresponding to the sum over all possible initial and final momenta that conserve energy. The four processes that comprise normal tunneling are shown in figure 2.6. The initial and final states are located along the horizontal dashed line of constant energy. The initial state, in superconductor 1, may be either a quasi-hole or quasi-electron state, with weighting u^2_{k1}. The final state, in superconductor 2, may also be either a quasi-hole or quasi-electron state, which is unoccupied with probability u^2_{k2}. The inverse process is similar, with the arrows reversed. The Gray processes may be described with a similar diagram involving Cooper pairs at the Fermi level, and each state is weighted by v^2_{k2} instead of u^2_{k2}.

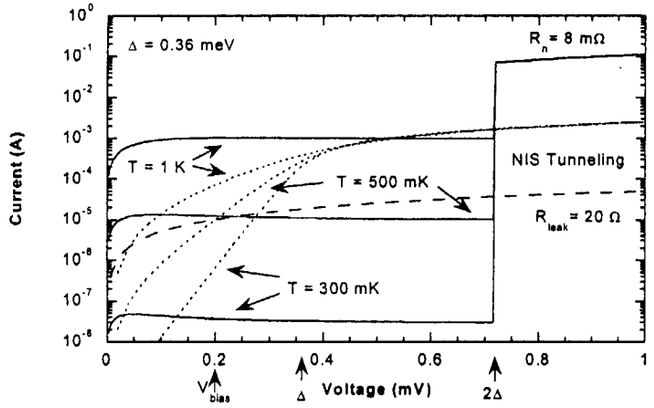

Figure 2.7: Thermal quasiparticle current of an ideal SIS tunnel junction at 300 mK, 500 mK, and 1 K (solid lines). The parameters shown are typical for a device with 200 nm aluminum traps. The leakage current (dashed line) must be added to the quasiparticle current and is dominant at low temperatures. In practice there is some amount of NIS tunnel current (dotted line). The maximum temperature at which devices with 200 nm aluminum traps remain insensitive to thermal changes is 300 mK. The curves are symmetric about the origin.

through a superconductor, so a flux line of arbitrary orientation will generally pass perpendicularly through the superconducting film, then travel along the insulating barrier and exit at the junction perimeter or perpendicularly through the other electrode. An NIS junction is formed in this case. We have observed point-like variations in the STJ response to a scanning electron beam which we believe to be penetrations of magnetic flux. [21]

The NIS contribution to the current-voltage characteristic varies with the magnetic history of the junction. Cooling a junction through its transition in a magnetic

field or while it is carrying (possibly thermoelectric) currents will trap magnetic flux in the junction. Magnetic flux can also become trapped if the field is increased to near the maximum field tolerated by the superconducting state, if a strong current is driven through the junction, or if the field is repeatedly cycled. The effect of the NIS current is to reduce our dynamic resistance and hence our amplifier gain. Nearly perpendicular fields may penetrate both junction electrodes in-line. This will form an NIN junction, which will also contribute to our leakage current. NIS leakage currents are strongly temperature dependent, while NIN currents are not. Both depend on the magnetic history of the junction. If we suspect there to be a large amount of trapped flux, we heat the STJ above its transition temperature and allow it to cool without any applied field or currents, and hope the niobium electrodes exclude the magnetic flux upon becoming superconductive.

The remaining feature of figure 2.7 is the large jump in current that occurs when the bias voltage corresponds to the sum of the gap energies ($\Delta_1+\Delta_2$) of the two electrodes. This occurs when the BCS singularities in the density of states align. Above this voltage the junction behaves nearly identically to a normal resistor. A logarithmic singularity in the current with positive and negative resistance sides also occurs at the difference energy ($\Delta_1-\Delta_2$). This is not observed in our symmetric junctions.

The tunneling of Cooper pairs must also be considered to accurately model the electrical properties of an SIS junction. The current through an SIS junction can be described by the "resistively-shunted junction" (RSJ) model, which by analogy is also called the "rotating pendulum" or "washboard" model. [22, 23] These models are described by a differential equation of the form

2. Only electron-like quasiparticles tunnel from superconductor 1, and only hole-like quasiparticles tunnel from superconductor 2, if all quasiparticle energies are less than eV.
3. There are twice as many quasiparticles for a given current, or, the current is half that of an NIN junction.

These statements fail to explain the factor of two for the following reasons:

1. This a true statement. However, we are not considering electron and hole states, but quasiparticle states that are superpositions of electrons and holes.
2. This is an incorrect statement, as shown in Figure 2.6, that results from over-reliance on the semiconductor representation. But by ignoring half of the quasiparticle population, the correct result is obtained.
3. This is a true statement, but is not a fundamental explanation.

The fundamental reason is a modification of statement (1): *the electron tunneling Hamiltonian, equation 2.13, only operates on the electron component of the quasiparticle.* The magnitude squared of the electron component of a quasiparticle with momentum k is u_k^2. For an individual quasiparticle near the gap, the electron and hole components are mixed equally and the transition probability is reduced to 50%. The average transmission of a balanced quasiparticle population is also 50%. The tunneling of a quasiparticle is exactly analogous to the transmission of a photon through two linear polarizers. As a result, all quasiparticles in a symmetric junction may tunnel at any energy, whether they be electron-like or hole-like.

2.6 Current-Voltage Characteristic

The electrical properties of the STJ may be described in terms of its current-voltage characteristic, or *I-V curve.* Figure 2.7 plots the thermal current of an ideal SIS junction at three temperatures as given by equation 2.23. An additional leakage current must be included in parallel to represent unavoidable normal-state conductance through the barrier. At low temperatures this leakage current dominates, and the dynamic resistance is determined by the leakage current. The ratio of the dynamic resistance to the normal resistance is the "quality factor" of the barrier. Typical values of the quality factor are 1000-10000.

The thermal current exhibits a negative resistance region, but this is almost always masked by the leakage current at low temperature for very high quality junctions. It may nevertheless may be difficult to apply a steady current bias in these regions. While high dynamic resistance maximizes the tunnel signal, it also increases the sensitivity to electronic and thermal noise. This noise not only appears across the junction, but also affects the tunnel signal.

We typically see an exponential increase in current near 1 Δ. This is evidence of normal-insulator-superconductor (NIS) tunneling, in which thermal electrons in a region of normal metal at the barrier are able to tunnel into the superconductor. These normal regions are most likely due to the penetration of magnetic flux lines perpendicular to the barrier. These flux lines are tubes with a normal core, surrounded by a circulating supercurrent. Thin superconducting films do not expel magnetic flux nearly as effectively as bulk superconductors. A line of magnetic flux will try to minimize its path

resonances, and the current is again multi-valued. Figure 2.9 contains the current-voltage characteristic of an actual junction, with several Fiske modes near the bias point.

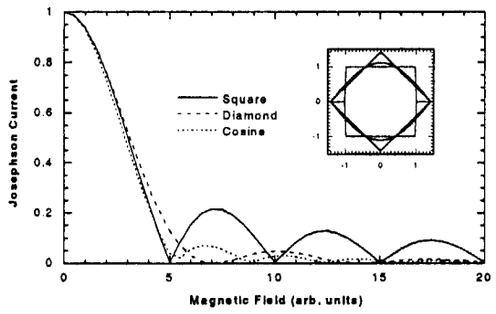

Figure 2.8: The zero-voltage superconducting tunnel current is modulated by a magnetic field that is applied in the plane of the junction. The modulation pattern is related to the Fourier transform of the junction perimeter along the direction of the field. The modulation pattern of three junction shapes (shown inset) with identical areas is plotted. The square pattern allows the Josephson current to be nulled at a lower field, but the field must be applied with precision. The diamond and cosine patterns have much smaller sidelobes, so that the current is very low even if it is not completely eliminated.

The Fiske resonance create several problems. First, they have negative dynamic resistance regions were the detector cannot be biased. Second, they themselves have low dynamic resistance and, though stable, are unsuitable bias points. Third, they provide numerous opportunities for the bias voltage to jump to, all at the same bias current. While the chances of such a jump decrease as the size of the jump increases, it seems there is always a Fiske mode nearby. The spacing between Fiske modes can be increased by reducing the junction dimensions. This is in conflict with our desire to have large absorbers and junctions. Each Fiske mode responds individually to the magnetic field in a complex manner and cannot be simultaneously eliminated with a small field, although they can be suppressed by large fields. Chapter 5 discusses the possibility that bias

instability due to nearby Fiske modes may be suppressed by an unusually large magnetic field.

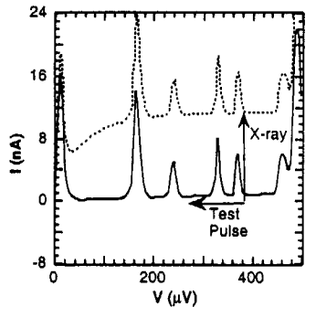

Figure 2.9: Current-voltage characteristic of a real junction taken with a voltage-biased circuit, in the cold, dark state (solid) and in the x-ray induced non-equilibrium state (dotted). Peaks in the current are called Fiske resonances, which is due to the tunneling of Cooper pairs with the emission of a photon with energy $h\nu = eV$ into the electromagnetic cavity formed by the junction. The gap is 0.7 meV. The junction is a 70 x 70 μm^2 diamond. Also shown are the load-lines for x-ray induced current changes and charge injected into the FET gate by a tail-pulse generator.

Figure 2.9 also illustrates the response of an STJ to an x ray and a current pulse. When the detector absorbs an x-ray, the excess quasiparticles cause the current to increase as if the temperature was very high, along the high-frequency load-line. When a current pulse is applied, the bias shifts along the cold I-V curve. The test pulse is used to provide an estimate of the electronic noise of the junction, bias circuit, and amplifier. However, the dynamic resistance of the "hot" I-V curve will always be less than the "cold" I-V curve. Also, it is clear from figure 2.9 that x-ray pulses and test pulses interact differently with the Fiske modes. The Fiske mode interaction and the nature of the "hot" I-V curve are currently being researched. [24, 25]

$$I = \frac{C\hbar}{2e}\ddot{\phi} + \frac{\hbar}{2eR_{sg}}\dot{\phi} + I_c \sin\phi, \qquad 2.25$$

which combines with the very important Josephson relation

$$V = \frac{\hbar\dot{\phi}}{2e} \qquad 2.26$$

to describe the behavior of the junction. In this expression ϕ is the phase difference across the junction, between the two superconducting quantum states. It can also be considered the angular displacement of a pendulum or the linear displacement of a particle moving along the wave-like surface of a washboard. C is the capacitance of the junction and also the mass of the pendulum or particle. R_{sg} is the sub-gap resistance, which is the linear approximation to the current below 2Δ. The conductivity $1/R_{sg}$ of the quasiparticle current damps the motion of the pendulum/particle. I is the applied bias current and is analogous to an applied torque on the pendulum or a tilt to the washboard. The remaining term, $I_c\sin\phi$ is the tunnel current of Cooper pairs. This term is the gravitational potential of the pendulum or washboard surface. The voltage V across the junction is seen to be the angular or linear velocity in the pendulum or washboard models.

This model describes a wide variety of SIS behaviors which are easily understood in the mechanical analogies. When the bias current exceeds a certain value I_c, the voltage will suddenly jump to a non-zero value. This voltage will have a small high-frequency oscillation, called the AC Josephson effect. If the product $R_{sg}C$ is sufficiently small, the junction is *over-damped* and the voltage will snap back to zero when the current is reduced below I_c. If the junction is *under-damped* then a non-zero voltage will be

maintained until a minimum current, the drop-back current, is reached. [22] The current-voltage characteristic of an under-damped junction is therefore hysteretic. This is the case for LLNL quasiparticle detectors.

The junctions tested in this thesis were operated with a constant current bias. Because the current-voltage characteristic is hysteretic and multiply-valued, there is always a chance that thermal or electrical noise will cause the bias to jump back to the zero-voltage Josephson current. [22] Therefore, it is desirable to suppress the Josephson current. The Josephson critical current I_c can be reduced or nulled completely by applying a weak magnetic field within the plane of the junction.. This reduction follows a diffraction pattern related to the shape of the junction as a function of the magnetic field strength. The I_c modulation patterns for square, diamond, and cosine perimeters are shown in figure 2.8. Square shaped junctions have the first minima at the lowest field, but required the applied field to be very stable and precise. Diamond junctions, which are simply square junctions mounted at a 45° angle, have much smaller sidelobes so that the critical current is very low at all fields above the first minimum. Junctions with a cosine-shaped perimeter have still weaker sidelobes. Once the critical current is suppressed, the junction can be stably biased near the drop-back current, which generally is the region of highest dynamic resistance.

The previously mentioned AC Josephson effect allows Cooper pairs to tunnel with the emission or absorption of a photon. This is normally very weak and averages to zero net current. However, the junction electrodes and barrier form an electromagnetic cavity which enhances the tunneling of pairs when the photon frequency corresponds to a cavity resonance. This results in Lorentzian-like peaks in the I-V curve called Fiske

aluminum traps is scanned with an electron beam. [21] Also, we have noticed that top niobium layer, which is the last to be deposited and is generally of poorer quality than the bottom layer, is more likely to exhibit position dependence. An extreme example is presented in chapter 5, in which the resolution of the top absorber varied linearly with the x-ray energy, while the resolution of the bottom absorber varied with the square root.

Tunneling Noise

The LLNL STJ design uses symmetrical quasiparticle traps on each side of the tunnel barrier. This allows quasiparticles to tunnel in both directions, by either the "normal" or "Gray" processes described earlier, until they recombine. This results in an increase in the total tunneled charge when measured with an integrating amplifier. This increase is equal to the average number of times a quasiparticle tunnels, $<n>_{av}$, and is equal to the ratio of the effective quasiparticle lifetime before recombination to the average time between tunneling events, τ_r/τ_t. This gain factor helps to reduce the contribution of electronic noise, but contributes its own noise since the actual number of times a quasiparticle will tunnel can fluctuate. This noise, F', is often combined with the Fano factor, called the effective Fano factor $F+F'$.

An ideal current amplifier could measure the initial current at time $t = 0$, which is subject only to the standard shot noise of a tunnel junction. In reality, there will be some integration. In a charge amplifier or gaussian-shaping amplifier, the integration is intentional. As a simple model, consider the accumulated shot noise over an integration window of time t in terms of the tunneling contribution to the energy resolution F':

$$F'(t) = \frac{\sigma_Q^2(t)}{[Q(t)]^2}, F'(\infty) = \left[1 + 1/< n >_{av}\right], \text{ with} \qquad 2.31$$

$$Q(t) = eN < n >_{av} \left(1 - e^{-t/\tau_r}\right), \text{ and} \qquad 2.32$$

$$\sigma_Q^2(t) = eN\left[< n >_{av} + < n >_{av}^2 - e^{-t/\tau_r}\left(2 < n >_{av}^2 \frac{t}{\tau_r} + < n >_{av}\right) - < n >_{av}^2 e^{-2t/\tau_r}\right]. \qquad 2.33$$

In these expressions, $Q(t)$ is the charge accumulated within the integration time t averaged over nominally identical x-ray absorptions, and $\sigma^2(t)$ is the variance about that average. Also, e is the electron charge, and N is the average number of quasiparticles in the trap after the cascade and trapping. A derivation is provided in appendix C.

In fully integrating systems, this noise term clearly dominates the cascade noise, F ~ 0.2, for all $<n>_{av}$ and can rival or exceed other contributions. The noise contribution as a function of integrating window duration, $F'(t)$, is plotted in figure 2.10. It is possible to find an optimum integration window that will minimize the tunneling noise. To a very good approximation, this minimum is obtained if the integration window has the duration

$$t_{optimal} = \tau_t \sqrt{0.15 + 3\frac{\tau_r}{\tau_t}}. \qquad 2.33$$

For a highly conductive junction with $<n>_{av} = 10$, the tunnel noise is reduced to be comparable to the cascade (Fano) noise after only accumulating 42% of the total charge! This may explain a recent result which claims to achieve better intrinsic resolution than the estimated limit, which is based on the fully integrated tunnel noise. [29]

An analysis of how current-following, charge-integrating, and pulse-shaping amplifiers affect the tunneling noise contribution has been done. [30] It predicts that the shaping amplifier is better able to filter out the tunnel noise contribution than any single-pole integrating amplifier, regardless of the integration time. This is because the single-

2.7 Detector noise sources

Ideally the measured current or charge should be directly proportional to the energy deposited by the absorbed x-ray. Unfortunately various sources of noise add to the signal and broaden x-ray spectral peaks. The dominant sources of noise are electronic noise, fluctuations in the number of quasiparticles produced in the quasiparticle cascade, shot noise due to tunneling, and spatial inhomogeneities.

$$\Delta E_{FWHM} = 2.35\left(\sigma^2_{electronic} + \sigma^2_{cascade} + \sigma^2_{tunnel} + \sigma^2_{spatial}\right)^{1/2} \qquad 2.27$$

Electronic Noise

Electronic noise is primarily due to amplifier and resistor noise in the STJ readout circuit, but also includes the effects of bias instabilities. Electronic noise is estimated by injecting current pulses into the amplifier while an x-ray spectrum is being measured. It is often subtracted in quadrature from the measured resolution to compute the "intrinsic" resolution of the spectrometer. Depending on the configuration of the amplifier and filters, the electronic noise contributes between 4 and 10 eV to the x-ray spectral peak in the devices measured in this thesis:

$$\Delta E_{electronic} = 4 \text{ to } 10 \text{ eV}. \qquad 2.28$$

Cascade Noise

The cascade noise is due to fluctuations in the number quasiparticles produced, and is characterized by the average quasiparticle creation energy, ε, and a measure of the correlation of the cascade, the Fano factor F: [26]

$$\Delta E_{cascade} = 2.35\sqrt{F\varepsilon E}\ . \qquad 2.29$$

Previous simulations of the cascade [18, 27, 28] suggest that typical values of F and ε are 0.22 and $1.75\Delta_{Nb}$, respectively, for a single absorbing layer of niobium. This value of ε implies that about 60% of the x-ray energy is used to create quasiparticles, while 40% of the energy escapes as low-energy phonons. The STJ is totally insensitive to phonons with energies less than twice the energy gap. This allows the STJ detector to operate at the count rates appropriate for fluorescence analysis, but at the cost of reduced resolving power. The question of how the cascade noise changes with the type of absorber material, or in a multilayer construction, is the focus of chapter 3 of this thesis.

Inhomogeneous Spatial Response

Spatial variations result when the signal produced varies with the location of the x-ray absorption. Major sources of inhomogeneity are losses though the leads and into normal metal niobium oxides at the surface and edges of the niobium. Also, the energy gap of the niobium may vary within the niobium, creating local quasiparticle traps. Diffusion in niobium is relatively slow compared to aluminum, so its inhomogeneities are enhanced. In general, the fraction of energy lost does not depend on energy, so the spectral peak width due to inhomogeneities is proportional to the energy:

$$\Delta E_{spatial} \propto E\,. \qquad 2.30$$

The LLNL STJ design stacks the thin absorber and tunnel junction together. Since quasiparticles have to travel only a few hundred nanometers before reaching the quasiparticle trap, the position dependence fairly minor. However, we have observed reduced signal generation near the perimeter of the junction when a device without

Chapter 3

Calculated Detector Response

3.1 Introduction

Any x-ray energy measurement is subject to some degree of uncertainty. Several contributions to this uncertainty were described in the previous chapter. These are, briefly: electronic noise, [31] spatial inhomogeneity, [32] tunneling noise, [10, 33] and cascade noise. [27, 28] The significance of the first three sources may be adjusted by various design decisions. The final source, the *cascade* noise, is intrinsic to any superconducting detector of quasiparticles. Estimations of the best ultimately achievable energy resolution are invariably attributed to this term. This contribution is very difficult to measure. Instead, probabilistic simulations, also called Monte Carlo simulations, substitute for actual measurements. These simulations generate two important statistics: the average number of quasiparticles produced by an x ray of given energy, and the fluctuation about that mean. These simulations are used to compute the ultimate resolving power of STJ technology. Relatively little work has been done to refine the initial calculations. One surprising fact from previous work is that both generic and material-specific simulations generate similar results. One may be tempted to believe that these statistics are universal for superconducting absorbers. An extended model shows that this is not the case.

This chapter extends the calculation in two areas. First, it examines the role of material-specific properties. It shows that the universal result is valid for certain conditions, and that no calculation is necessary if these conditions are met. However, it also shows that large deviations from the universal result are possible, which may either increase *or* decrease the ultimate resolving power of the STJ detector. In some cases, the method of film deposition may be as important as the material composition.

The second extension in this chapter examines how the cascade occurs in a multilayer of thin films. The simplest view is as follows: an x ray is absorbed in the absorbing material, e.g. niobium. The ejected photoelectron and Auger electrons create hot electrons and phonons. Eventually, some number of quasiparticles are created. This creation is assumed to have occurred entirely in the niobium, due to confinement effects and the short time-scale of the cascade. The quasiparticles diffuse to the trap and relax into the trap, emitting phonons. These phonons have a chance of breaking Cooper pairs in the trap if they have sufficient energy. Thus, the total number of quasiparticles present in a typical trap at the end of the cascade is between one and three times the number created in the niobium, and the fluctuations in this number are a combination of the niobium cascade and the trap multiplication noise. However, the niobium films in LLNL devices are so thin that hot electrons, phonons, and quasiparticles should experience little or no confinement.

Instead, one should think of the cascade as occurring in all films simultaneously. Hot electrons may relax directly to the bottom of the trap, so there is no discrete trapping step. Phonons will carry energy to different layers, even those on the opposite side of the tunnel barrier. This chapter presents Monte Carlo simulations of the electron and phonon

pole amplifiers give greater weight to the most recent signals, which are more noisy, while the earlier part of the pulse decays away. While it is true that the peak current from a wide-bandwidth, current-following amplifier depends on only the earliest signals, it is overwhelmed by the classical shot noise.

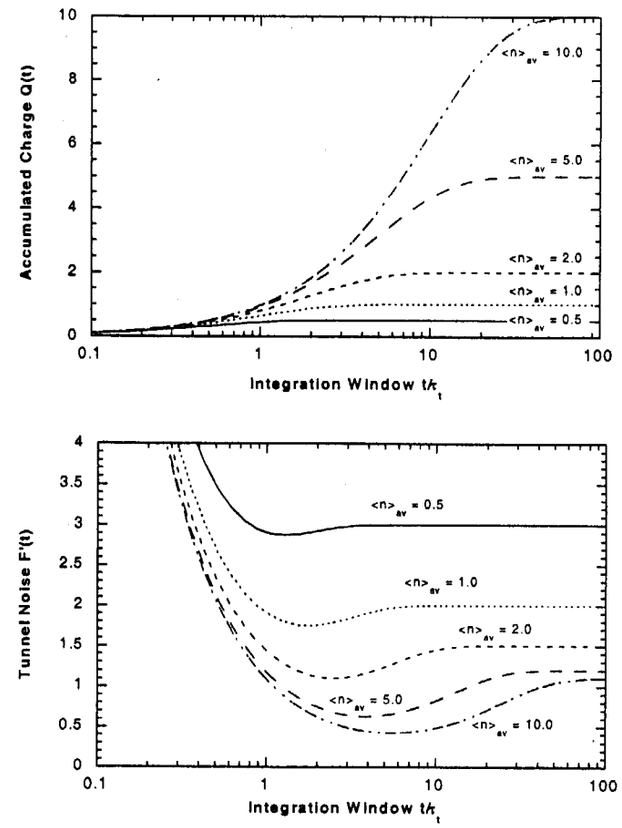

Figure 2.10: Charge and noise accumulated after partial integration. Fluctuations in the number of times the quasiparticles tunnel adds additional noise, which is greater in the tail of the pulse. This noise can be reduced by integrating only the early part of the pulse.

$$F = \frac{\sigma_n^2}{n}. \qquad 3.2$$

The value of ε will be near that of Δ if the cascade process is efficient. Because energy is always lost in the form of sub-gap phonons, the actual value of ε will be somewhat greater than Δ. If large numbers of quasiparticles are lost in normal regions or regions with suppressed gap, the value can be substantially greater than Δ. [18, 34, 35]

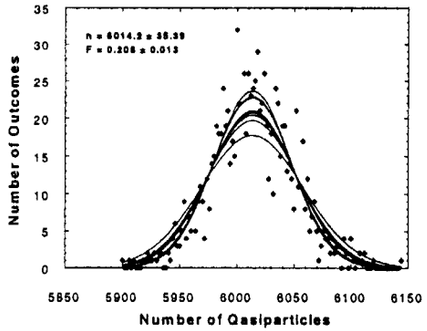

Figure 3.1: Distribution of quasiparticle generation for 1000 cascades with the same initial energy. The mean number of quasiparticles and the Fano factor are 6014.2 and 0.208, respectively. The curves show Gaussian fits to 10 subsets of 100 points, which are used to estimate the variance of the Fano factor.

The variability of the overall energy loss is quantified by the Fano Factor. The cascade process is highly correlated as a result of being constrained by energy conservation during most of the cascade. It is only in the final stages of the cascade, after most of the quasiparticles have been created, that energy loss due to sub-gap phonons introduce variations in the number of quasiparticles created in nominally identical cascades. As a result, F is a small number less than 1. For a system with no correlations,

the variation would be Poissonian and $F=1$. Figure 3.1 illustrates the calculation of n and F from a Monte Carlo simulation of 1000 cascades. The moments of the approximately Gaussian distribution of quasiparticle production generate the required statistics. Given these estimates, the so-called theoretical minimum width of a monochromatic x-ray line measured with an of an STJ spectrometer can be written as

$$\Delta E_{FWHM} = 2.355\sqrt{F\varepsilon E}. \qquad 3.3$$

This expression is widely used to define the upper-limit of the energy-resolving performance of an STJ detector, [28, 36] e.g. ΔE = 5 eV FWHM at 6 keV. These values are based on computerized Monte Carlo simulations, since they are very difficult to measure in practice. [18] While STJ spectrometers continue to improve, they have not yet achieved the theoretical limit. [36-38] Much of this discrepancy is due to spatial dependence in the absorber, electronic amplifier noise, and noise due to multiple tunneling, as described in the previous chapter. However, one can reasonably expect engineering improvements in these three areas. This leaves the cascade noise itself, which cannot be measured directly, only calculated. Since each calculation must simplify the problem to make it tractable, it is possible that the cascade contributes more noise than calculated. After briefly summarizing previous work, this chapter will present the first of two enhancements to the cascade noise analysis: dependence on the phonon spectrum of the absorber material.

3.3 Prior Calculations

There are primarily three approaches to modeling the quasiparticle cascade. The first is purely analytic solutions. The second is numerical integration of the differential

relaxation in a multilayer structure, progressing in increasing complexity and physical relevance. These simulations reveal that under certain circumstances, the cascade noise maybe greater than, lesser than, or equal to the universal result for a single layer.

3.2 Cascade and Cascade Statistics

The superconducting absorber transfers the energy of an absorbed photon to a population of excess quasiparticles through the cascade process: energetic electrons and photons excite/create additional electrons/phonons until all the energy has been distributed among quasiparticle and phonon populations with energies near the superconducting gap energy. Energetic electrons may break a Cooper pair directly, resulting in three electrons whose energy sum to the energy of the initial electron. Alternatively, an energetic electron may relax to a lower energy while emitting a phonon whose energy is equal to the difference in the electron's initial and final energies. These phonons may be absorbed by a Cooper pair, resulting in two electrons whose energy sum to that of the now-destroyed phonon. The key detail is that the final energy of any individual electron may take on a range of values, but that energy is conserved in any electron-electron or electron-phonon scattering event.

In a normal metal, this process continues until the energy is distributed among the conduction electrons. These electrons then have a thermal energy distribution with an elevated temperature approximately equal to the energy of the x ray divided by the heat capacity of the normal metal. A normal metal microcalorimeter, designed to be thermally isolated from the outside world, would convert 100% of the x-ray energy into "warm" electrons. Thus, there is little or no significant noise contribution from the cascade. A thermal detector derives much of its superior resolving power from this fact. The

disadvantage to such a detector is the long cooling time that necessarily results from thermal isolation.

A superconducting detector that is sensitive to quasiparticles is much faster, but suffers from noise intrinsic to the cascade process. Each quasiparticle has a minimum energy, Δ, which is on the order of 1 meV. This introduces the possibility of a quantization error as the x-ray energy is used to create new quasiparticles. Since quasiparticles must be created in pairs, there is an energy threshold for quasiparticle creation. An initial phonon must have at least 2Δ energy, and an initial quasiparticle must have at least 3Δ. Although energy is always conserved in electron-electron and electron-phonon interactions, loss of energy from the quasiparticle system is inevitable because the initial and final energies will not be exact multiples of these thresholds. There is a non-zero probability that a phonon with energy less than 2Δ, called a *sub-gap* phonon, will be created in every relaxation event of a hot electron. Barring re-absorption by a quasiparticle, sub-gap phonons will escape the absorber and their energy will be lost. Each cascade loses a different amount of energy. This introduces a noise source intrinsic to measurement.

The cascade is quantified by two statistics: the effective quasiparticle creation energy ε and the Poissonian pre-factor, or Fano factor, F. These statistics are defined in terms of the x-ray energy E, the mean number of quasiparticles n, and variance in quasiparticle number σ_n^2 as follows:

$$\varepsilon = \frac{E}{n}, \text{ and} \qquad 3.1$$

recombine, their energy is carried by a phonon with insufficient energy to break a Cooper pair once it leaves the hot-spot. If a significant number of quasiparticles recombine from the reduced gap of the hot-spot, the total number of quasiparticles is reduced and the spectrometer resolution is degraded.

Modeling with differential equations can provide the number of quasiparticles, and hence, ε. It can also include possible losses due to the hot-spot effect. This type of modeling is critically important for large, thick absorbers with relatively small STJ sensors, e.g. superconducting crystals. However, the stacked, thin-film geometry of the STJ detectors tested at LLNL have integrated absorbing layers which are comparable in size to the supposed hot-spot effect, at least in thickness. Furthermore, the low-gap trapping layer will absorb sub-gap phonons created by a hot-spot, reclaiming their energy. Hot-spot effects are therefore less important in modeling our thin-film devices. This assumption is supported by the multilayer Monte Carlo calculations presented at the end of this chapter.

Finally, the third method of modeling is the Monte Carlo simulation. An initial population of phonons containing the energy of the x ray is created. Each phonon is assumed to break a Cooper pair into two quasiparticles. The energies of these quasiparticles are randomly selected from a theoretical distribution, but constrained to sum to the energy of the phonon. Each quasiparticle created is then allowed to relax to a lower energy, creating a phonon with an energy also selected at random, from another theoretical distribution. This process continues until no more Cooper pairs can be broken. The total number of quasiparticles is recorded, and the process is repeated.

The first such calculation was performed by Kurakado for a tin absorber. [27] This calculation produced the values $\varepsilon = 1.7\Delta$ and $F = 0.2$ which are universally quoted for superconducting absorbers. He also generated a plot similar to figure 3.2. This figure shows the variation of ε and F with initial quasiparticle energy. This graph represents the quasiparticle creation statistics resulting from "injection" of quasiparticles into a superconductor. These functions vary as energy thresholds for pair-breaking are crossed. However, multiple scattering and pair-breaking events remove the effect of the 2Δ quasiparticle creation threshold at energies above 10Δ, resulting in an average value. Another interesting feature is that the point of minimum noise (minimum F) does not correspond to the point of maximum signal (minimum ε). This will be explained later in this chapter.

Burnell, *et al.* calculated the quasiparticle multiplication m_{trap} that would result from a quasiparticle relaxing into a deep trap. [41] Their quasiparticle multiplication function is again the function of figure 3.2, with the transformation $m_{trap}(E) = E/\varepsilon(E)$. They included a simple model for allowing (in fact, requiring) quasiparticles to absorb the athermal phonons produced by relaxation. Furthermore, they were able to compare their calculations with a quasiparticle injection experiment. The measured quasiparticle multiplication fell between the model with phonon re-absorption and the model with no phonon re-absorption. These measurements support the existence of structure in ε as shown in figure 3.2.

equations that govern electron and phonon dynamics. The third is Monte Carlo simulation of each quasiparticle and phonon generated during the cascade. Each approach has its merits and complements the other methods.

The first method is theoretical calculations. A purely analytical model has recently been developed by Ochinnikov and Kresin [39] and refined by Kozorezov *et al.* [40] This model calculates the growth of the quasiparticle number during each of the aforementioned cascade stages. A value for ε can be obtained by this method. While some approximations are necessary, the closed-form solution is much easier to use than the numerical methods. One can look forward to further refinements and possibly closed-form solutions for the variance in quasiparticle number as well.

The second method is modeling by differential equations, and is currently the most active area of research. These models include the interaction between quasiparticles, Cooper pairs, and phonons; the diffusion lengths of quasiparticles and phonons which are highly dependent on the energy; and the possibility that the superconducting energy gap may be suppressed by the intense energy of the x-ray, by magnetic fields, by impurities, or inhomogeneity or anisotropy that is a property of the absorber material. These are critically important details because energy can be permanently lost if quasiparticles recombine in a region with a reduced energy gap or if the tunnel junction sensor is too far away. These issues are difficult to include in a Monte Carlo simulation because the particles are not independent. Thus, the two methods complement each other. These details, which are excluded from the calculations presented in this chapter, are summarized below.

- Quasiparticles recombine in pairs. Therefore, calculating the recombination rate quires the excess quasiparticle density to be monitored in energy, space and time. Similarly, the absorption of phonons by quasiparticles requires the phonon density to be known in energy, space and time as well.
- The mean free path of the initial photoelectron and Auger electrons is extremely short. At this point, energy is transported by phonons. However, the mean free path of above-gap phonons is also rather short since they are readily absorbed by Cooper pairs, producing quasiparticles. So, at intermediate energies, energy is carried by quasiparticles. However, quasiparticles have a nonlinear dispersion curve (see figure 2.1) and the group velocity approaches zero as the quasiparticle energy nears the gap. As the x-ray energy is transferred from a few high-energy electrons and phonons to many low-energy quasiparticles, the flow of energy slows. Eventually the energy is again transferred by 2Δ phonons created by the quasiparticles recombining, which subsequently break Cooper pairs after traveling a short distance. If the quasiparticle-phonon system reaches this point, other slow processes, such as quasiparticle trapping, can permanently remove energy from the system.
- High temperatures, or equivalently high quasiparticle densities, can suppress the superconducting gap. This region is referred to as the *hot-spot* or *fireball*. Gap suppression along the path of the photoelectron and Auger electrons is expected in most materials. [9, 18] Quasiparticles that relax to, or are created at, the reduced gap are trapped. They may escape this trap if they absorb an athermal phonon created within the hot-spot. On the other hand, if two trapped quasiparticle

Eliashberg function

Eliashberg re-formulated the BCS theory in terms of the *electron-phonon coupling* function, denoted as $\alpha^2(\omega)F(\omega)$. This function may be calculated [43] or measured. [44] To calculate α^2F, one averages the product of the phonon density of states and the electron-phonon matrix element over a momentum surface of constant energy, taking special care to include all electron-phonon interactions, e.g. Umklaap processes. The expression, α^2F, reflects an artificial factoring of the average into a slowly-varying coupling α^2, and the phonon density of states F.

To measure α^2F, one carefully measures the second derivative of the current-voltage characteristic of a tunnel junction with electrodes constructed from the superconductor in question. [44] Because α^2F is so fundamental to strong-coupling superconductivity, peaks in α^2F are transformed into resonance structures in the quasiparticle density of states in a manner analogous to the Kramers-Krönig relationship in electromagnetics. These structures then appear in the derivatives of the quasiparticle tunneling current with respect to applied voltage.

The most important moment of α^2F is the electron-phonon coupling constant, λ. This constant is defined as

$$\lambda = 2\int_0^{\Omega_D} \frac{\alpha^2(\omega)F(\omega)}{\omega}d\omega, \qquad 3.4$$

and is also related to the electron effective mass enhancement due to the electron-phonon interaction,

$$\frac{m^*}{m_e} = Z(0) = 1+\lambda. \qquad 3.5$$

In this expression m^* is the observed electron mass, m_e is the electron mass, which includes mass enhancements due to Coulomb interactions and band structure, and $Z(0)$ is called the *renormalization* at the Fermi surface. This mass enhancement is an independently measurable property, which allows Eliashberg theory to be applied even in the absence of a known α^2F. Once λ is determined, the renormalized coupling $\lambda/(1+\lambda)$ plays the same role in Eliashberg theory as $N(0)V$ does in BCS. A critical detail in the definition of λ is the fact that low-energy interactions contribute to λ more than high-energy interactions.

Scattering and pair-breaking rates

Kaplan, *et al.* used Eliashberg's formalism to calculate the energy-dependent quasiparticle scattering, creation, and recombination rates due to phonon interaction. [13] These expressions are widely used in differential equation models of quasiparticle relaxation. We shall use them here to determine the relative probability of different outcomes (final energies) from scattering and pair-breaking events, as well as allow competing diffusion and relaxation processes in the multilayer model.

Kaplan derived the scattering and pair-breaking rates with the form of:

$$\tau_s^{-1}(\omega) = \frac{1}{\tau_0}\int_0^{\min[\omega-\Delta,\Omega_{max}]} N_s(\omega-\Omega)\alpha^2F(\Omega)\left[1-\frac{\Delta^2}{\omega(\omega-\Omega)}\right]d\Omega \qquad 3.6$$

$$\tau_{PB}^{-1}(\Omega) = \frac{1}{\tau_u^{ph^*}}\int_{\Delta}^{\Omega-\Delta} N_s(\omega)N_s(\Omega-\omega)\left[1+\frac{\Delta^2}{\omega(\Omega-\omega)}\right]d\omega \qquad 3.7$$

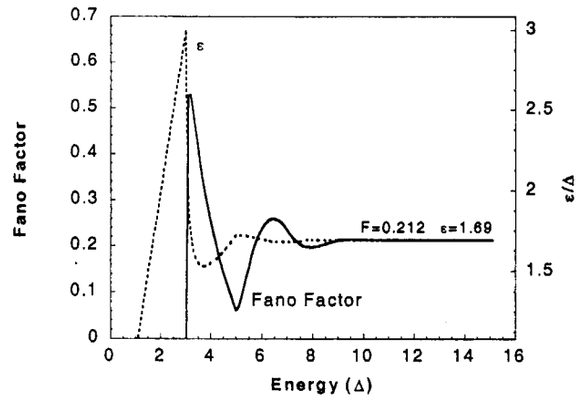

Figure 3.2: Variation of ε (dashed) and F (solid) as a function of initial quasiparticle energy for a Debye-BCS absorber. Rapid changes occur as the quasiparticle energy crosses thresholds at 3Δ and 5Δ. However, the random distribution of final states for quasiparticle creation and relaxation smooth out the discontinuities at higher energies, eventually approaching a limiting value. There exist similar functions for initial phonon energy.

Rando, *et al.* provided an important repetition of Kurakado's calculation. [28] First, they calculated ε and F for a "Debye-BCS" absorber. This model assumes a quadratic form for the electron-phonon coupling, proportional to the phonon-density of states, and a quasiparticle density of states given by BCS theory. Second, they repeated the calculation for niobium and tantalum, using the experimentally determined electron-phonon coupling functions in lieu of the Debye approximation. In all three cases, $\varepsilon = 1.7\Delta$ and $F = 0.2$ were obtained.

The thesis of Brink combined hot-spot modeling with Monte Carlo, and also made the painstaking measurements to determine the actual number of quasiparticles created. [18] He studied Nb-I-Nb and Al-I-Al junctions (I = insulator). While his

niobium results agreed fairly well with previous calculations, aluminum had an $\varepsilon > 4\Delta$. He attributed this to aluminum's susceptibility to the hot-spot effect. Also, the electron-phonon coupling of aluminum is weak compared to the coupling of most other superconductors, and 2Δ phonons readily escape thin films of aluminum.

This concludes the review of prior work. The remainder of this chapter will be divided into two sections. The first will show that materials with quadratic electron-phonon coupling at low energies will generate the same statistics as the Debye-BCS absorber, while materials with structure in the electron-phonon coupling function at low energies will deviate from the Debye-BCS result. The second will show how heterogeneous absorbers composed of superconductors with differing energy gaps will deviate from the Debye-BCS result. Some background material motivating and describing the Monte Carlo calculations will be presented first, with most of the implementation details and raw results provided in appendix A for reference.

3.4 Electron-Phonon Coupling

BCS explained superconductivity with a simple attractive potential, which was of constant strength up to a cut-off momentum, and zero otherwise. This theory successfully predicted the superconducting and thermodynamic properties of many superconductors, such as aluminum, which are now called *weak-coupling* superconductors. However, the properties of other superconductors, such as lead, deviated from the BCS predictions. These superconductors were successfully modeled by Eliashberg's *strong-coupling* theory. [42]

Material Variability

The Eliashberg formalism provides a mechanism for including material dependencies in the quasiparticle cascade via the electron-phonon coupling function α^2F. Both Kurakado and Rando *et al.* addressed this when they used the measured α^2F for tin, niobium, and tantalum. [27, 28] By coincidence, these three materials are quadratic over a sufficient range which results in nearly identical cascade statistics. This is not true for all materials. While most, if not all, materials have a quadratic α^2F functions at low energy, many large-gap superconductors have structure within the first few multiples of the gap energy. These exhibit different gap statistics.

However, there is another source of variability that has not been addressed: disorder. In general, disorder shifts the α^2F spectrum to lower energy, enhances low-energy coupling, and increases coupling to transverse phonons. The amount of disorder can vary greatly among different production techniques. For example, the devices tested at LLNL are composed of polycrystalline niobium, with a residual resistance ratio of about 6. Other groups are making devices from epitaxial niobium and tantalum. [45-47] Devices are also constructed on solid crystals of tantalum, with resistance ratios > 1000. Furthermore, the α^2F functions are usually obtained from sputtered thin films, and the film quality is not always specified. These are further reasons why one should not simply quote the original cascade simulation as a blanket result for all STJ spectrometers.

The interaction with transverse phonons merits more attention. In an ideal metal, electrons do not couple to transverse (shear motion) phonons. They only couple to longitudinal (compression-tension motion) phonons. Longitudinal waves result in local changes in charge density, while transverse waves do not. In the *adiabatic*

approximation, the fast, light electrons quickly follow the motion of the heavy, slow ions to counter this change in charge density.

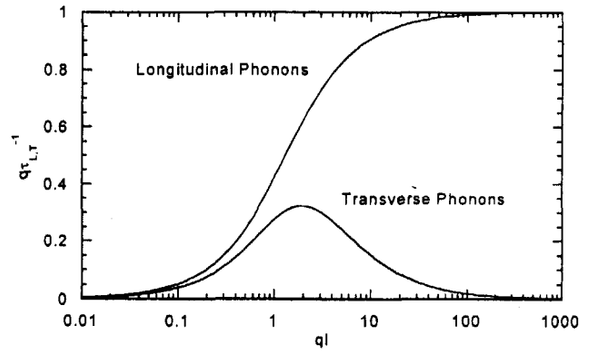

Figure 3.4: Normalized coupling to longitudinal and transverse phonons with momentum q by electrons with impurity-, grain-, or boundary-limited mean free path l. Moderately decreasing the mean free path decreases longitudinal coupling while increasing transverse coupling.

As impurities are introduced, the electron mean free path decreases and the electrons are less able to follow the highest-frequency motions of the ions. Thus, the coupling to longitudinal phonons decreases. However, the electrons are now able to follow the motion of the impurities, which may be excited by transverse waves. This is illustrated in figure 3.4, which plots the normalized longitudinal and transverse coupling against the product of phonon momentum q and electron mean free path l. [48, 49] As l continues to decrease, the transverse coupling reaches a maximum and then decreases along with the longitudinal coupling. Similar results are obtained if the mean free path is limited by grain boundaries or film thickness.

In these expressions, τ_0^* and τ_β^{pb*} are characteristic times dependent on the material, N_s is the quasiparticle density of states, and the integral is dimensionless. The energy Ω_{max} is the maximum acoustic phonon energy and is approximately Ω_{Debye}. Factors containing Bose and Fermi functions have been omitted. In equation 3.6, $\tau_s^{-1}(\omega)$ is the inverse lifetime of a quasiparticle with initial energy ω, which subsequently scatters with emission of a phonon with energy Ω, integrated over all allowed Ω. Similarly, $\tau_{PB}^{-1}(\Omega)$ in equation 3.7 is the inverse lifetime of a phonon with energy Ω, which is absorbed by a Cooper pair and creates two quasiparticles with energies ω and $(\Omega-\omega)$. The *integrals* provide the overall rates, integrated over the possible final states, while the *integrands*, properly normalized, provide the probability distributions of the possible final states.

Frequently, α^2F is replaced by a quadratic fit to the low-energy dependence of α^2F. This assumes a constant coupling α^2 and Debye model for the density of states. Figure 3.3 compares the measured and approximated functions, as well as the calculated phonon emission rates using the two functions. Despite the large differences between the two results, the Debye-BCS model and the realistic niobium model both produce very similar cascade statistics, as did the tantalum model. It will be shown later that this is directly due to the quadratic form of all three models at low energy; the structure at high energy is unimportant.

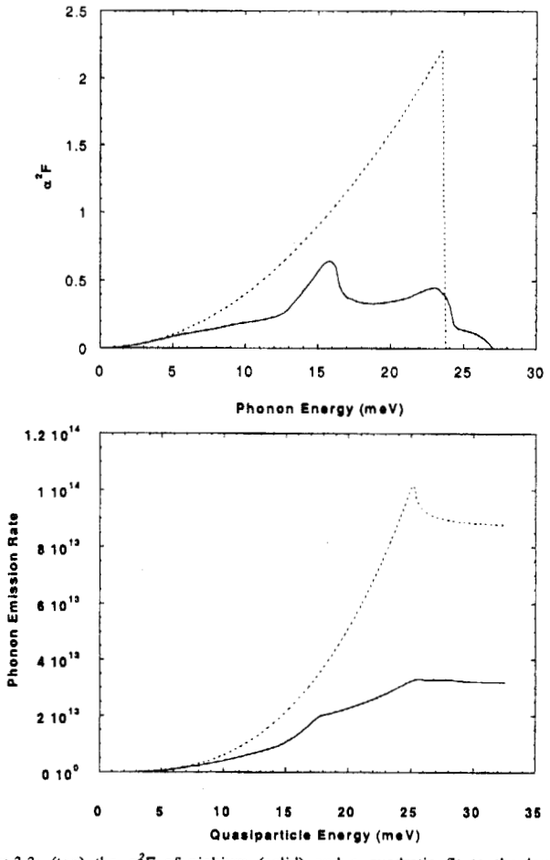

Figure 3.3: (top) the α^2F of niobium (solid) and a quadratic fit to the low-energy dependence (dashed). (bottom) the calculated phonon emission rate of a quasiparticle using Nb α^2F and quadratic functions.

substituted into equation 3.6 and modifies the probability distribution of quasiparticle relaxation.

The model α^2F function has the form

$$\alpha^2F(\Omega) = aA_0\{L(\Omega,\Omega_0,\delta\Omega) - L(\Omega - \min[\Omega,\Omega-\Omega_0],\Omega_0,\delta\Omega)\}^2 + bB_0\Omega^2$$
$$L(\Omega,\Omega_0,\delta\Omega) = \frac{(\delta\Omega)^2}{4(\Omega-\Omega_0)^2+(\delta\Omega)^2} \qquad 3.8$$

The function $L(\Omega,\Omega_0,\delta\Omega)$ is the Lorentzian function centered at Ω_0 and with width $\delta\Omega$. The parameters A_0 and B_0 normalize the area of each function, and a and b are the relative magnitudes of the perturbation and quadratic α^2F functions, respectively. The ratio a:b defines the size of the perturbation. This model α^2F function was designed to have the following properties:

- Both the function and integral are simple analytic functions in closed-form. The integral is analytic for arbitrary endpoints.
- The perturbation is a quadratic function near zero. This ensures the integrand is zero at zero even if the Bose-Einstein term $[1 + n(\Omega)]$ is included in the integrand of equation 3.6. Also, it preserved the quadratic dependence at low energies when the perturbation was centered at high energies.
- The size of the perturbation is defined as the relative area of the perturbation to the area under the quadratic curve, up to the Debye energy.
- Near zero or the Debye energy, the perturbation is allowed to become narrower while preserving its area. Away from these endpoints, the perturbation's half-width quarter-maximum (HWQM) is $\delta\Omega$.

Plots of the model α^2F with the perturbation and its dependence upon its parameters are shown schematically in figure 3.5.

The Monte Carlo calculations were repeated for differing sizes and locations for the perturbation peak. Typical values were 0.1 meV HWQM, centered from 1.0 to 10.0 meV in 0.1 meV steps. There was one additional calculation: the energy gap. The transition temperature and energy gap increase with increasing electron-phonon coupling. These were estimated by a semi-empirical formula (equations A.8 - A.10) that is accurate to within 10% for both strong- and weak-coupling low-temperature superconductors. [50]

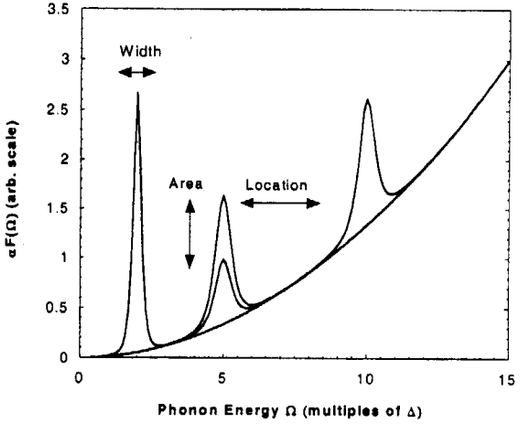

Figure 3.5: Schematic illustration of the model α^2F function and its three parameters. On the left, the perturbation is half as wide (0.5 HWQM) and nearly twice as tall as the others in the graph, preserving the area. In the center, two perturbations that differ in area by a factor of two are contrasted. On the right, the perturbation has been shifted, preserving area and nearly preserving width. All perturbations have finite extent: the left is non-zero from 0 to 4, the center extends from 0 to 10, and the right is non-zero from 5 to 15.

Coupling to transverse phonons has significant results. First, transverse modes have much longer wavelengths than longitudinal modes and the transverse peak in the phonon density of states is at a much lower energy than the Debye energy. This peak may be in the energy range to which the cascade is sensitive. Furthermore, because λ weights low-energy coupling more than high-energy coupling, impure and thin films usually have higher gaps and T_c than bulk, pure crystals of the same material. Increasing the gap further extends the range in which the cascade is sensitive.

Of course, in real metals, there is always some coupling to transverse phonons. Anisotropy of the Fermi surfaces and Umklaap scattering are two characteristics that allow transverse coupling. As such, there is usually a peak in the α^2F function that corresponds to coupling to the transverse phonons. Nevertheless, device fabrication techniques may have a substantial, additional impact on α^2F, the superconducting gap, and the cascade statistics. The model used in this chapter will systematically show what effect, if any, coupling to low-energy phonons have on the cascade.

3.5 Monte Carlo Simulations of Material Dependence

Briefly, the cascade statistics were calculated in the following manner. It is assumed that the earliest part of the cascade has produced a small population of hot electrons. These hot electrons will transfer almost all of their energy into acoustic phonons. An initial energy, typically $10^4\Delta \sim 15$ eV, is assumed. It is unnecessary to increase the initial energy to actual x-ray energies. The calculation produces a narrow gaussian-like distribution of quasiparticle yields, so increasing the energy does not change the statistics. It is only necessary to provide enough energy so that the initial phonon distribution contains enough phonons to closely represent the α^2F function. A population of phonons

is randomly selected from the α^2F function until all of the initial energy has been distributed. This population is represented in the computer as a list. Phonons with energies < 2Δ are immediately discarded. The phonon at the top of the list is removed, and two quasiparticles are created in accordance with the integrand in equation 3.7. Quasiparticles with energies < 3Δ are immediately discarded; the rest are added to the list. Again, the top particle of the list is removed. If it is a quasiparticle, it is allowed to relax in accordance with the integrand in equation 3.6. A phonon equal to the relaxation energy is added to the list. The quasiparticle is returned to the list if its new energy >= 3Δ, otherwise it is discarded. Particles continue to be added and removed from the list until the list is empty. At this point, the total number of quasiparticles created is recorded, and the calculation is repeated with a new population of phonons. The calculation is over after 1000 repetitions and the cascade statistics are calculated.

A baseline result is created using the Debye-BCS models for a solid. The electron-phonon coupling is represented by a quadratic energy dependence, and the quasiparticles have a BCS density of states. The gap and Debye energies are the values for niobium: $\Delta = 1.5$ meV and $\Omega_D = 23.7$ meV. This results in values of $\varepsilon/\Delta = 1.69$ and $F = 0.19$ for the cascade statistics.

Electron-phonon (α^2F function) modeling

The following Monte Carlo simulations use a model α^2F function following the observations that certain materials, such as tantalum and niobium, are well represented by the Debye-BCS model, and that low-frequency modes, such as transverse modes, are more likely to affect the cascade statistics. The model α^2F function is quadratic function of the phonon energy up to Ω_D with a Lorentzian-like perturbation. This function is

energetic quasiparticles into many gap-edge quasiparticles with no loss of energy and no fluctuation in the number created. Similarly, locating such a peak just below 2Δ would demonstrate the least efficiency, since almost every phonon would be lost without breaking a Cooper pair. Perturbations with area ratios $a{:}b > 1{:}32$ have essentially identical cascades statistics at all locations of the perturbation.

On the other hand, even small changes to α^2F can have a large effect on the cascade. The perturbation $a{:}b = 1{:}4000$ is insignificant relative to the entire distribution. Truncating the distribution so that $\Omega_D = 15\Delta$, as in niobium, increases this ratio to $1{:}18$, which would still seem insignificant. However, as shown in the bottom frame of figure 3.6, this peak in α^2F can still encourage phonons with a particular energy to be emitted over 50% of the time when located between 2Δ and 6Δ. The statistics ε and F approach limiting values as the perturbation moves to higher energy. This is not due to the decreasing effective strength of the perturbation. As shown by Kurakado, [27] a mono-energetic injection of quasiparticles or phonons above 10Δ will produce the same limiting values for the cascade statistics. The limiting values for the statistics is due to the averaging out of the quantization effect caused by the presence of the energy gap. The perturbation encourages the creation of certain high-energy phonons, but these phonons ultimately deposit the same fraction of their energy into quasiparticles as other high-energy phonons not influenced by the perturbation.

Cascade outcome probabilities

The remaining question is the behavior of ε and F as functions of the energy of quasiparticles, phonons, or α^2F peaks. Both statistics achieve minimum values when the phonon density is enhanced at 2Δ, corresponding to the most-efficient cascade. At higher

energies, however, lowest-noise does not correspond to maximum yield. This is explained by examining the probability of a single energetic phonon or quasiparticle *eventually* producing 0, 2, 4, ... additional quasiparticles. This can be calculated approximately without relying on stochastic techniques.

First, energies are quantized to be multiples of $\Delta/10$ to make the problem tractable. For a given quasiparticle with energy ω, there are $10(\omega-\Delta)$ different relaxation phonons that may be emitted. The probability of each of these outcomes is easily calculated from equation 3.6. Similarly, a phonon with energy Ω will create one of $10(\Omega/2-\Delta)/\Delta$ possible quasiparticle pairs with distinct energies. The probability of each of these outcomes is computed from equation 3.7. The probability of a quasiparticle with energy ω eventually producing between 0 and 2*integer$[(\omega-\Delta)/2]$ additional, fully-relaxed quasiparticles is readily obtained. Further details are provided in the appendix.

This calculation was performed for the baseline Debye-BCS model, for the minimum F at 3Δ, and for the maximum ε at 4Δ. A large peak was used to maximize its effects. The quasiparticle production probabilities are shown in figure 3.7. These figures illustrate exactly what effect the perturbation has on the cascade when located at these critical energies. When located at 3Δ (middle frame), cascade noise is minimized. This causes quasiparticles with energies between 4Δ and 6Δ to almost always produce two additional quasiparticles, for a total of three. The lack of multiple outcomes reduces the statistical fluctuations in the number of quasiparticle produced, and F attains a minimum.

Compare when the peak is located at 4Δ (figure 3.7 bottom). In this case, there is a significant chance of not producing *any* additional quasiparticles up to 5Δ. Similarly, the probability of only producing two quasiparticles, again for a total of only three, in the

Thus, while the perturbations are of equal width and equally spaced in actual energy, they vary somewhat when scaled to Δ. Furthermore, if Ω_D/Δ is less than 15, the ratio for niobium, the initial energy is $10^4\Omega_D/15$ instead of $10^4\Delta$ to ensure that the initial phonon distribution is sufficiently sampled.

A peak in α^2F is similar to phonon injection, and the results were expected to be similar to the plot shown in figure 3.2, except shifted by Δ and broadened by the peak width. The actual results are shown in the top and middle frames of figure 3.6. The ratio a:b is somewhat misleading as it depends on the quantity $(\Omega_{Dw}/\Delta)^3$; the gap Δ is relatively small compared to niobium and varies with the precise form of α^2F. It is helpful to define a measure of the perturbation's influence that is independent of this parameter.

A quasiparticle with energy ω may emit a phonon $0 < \Omega < \omega-\Delta$. The perturbation will have its greatest influence on quasiparticles with energy $\omega \approx \Omega_0+\delta\Omega+\Delta$. One may estimate the relative size of the perturbation over this restricted domain as $1:[(\Omega_0+\delta\Omega)/\Omega_D]^3(b/a)$. For the 1:4000 point near 4Δ, $\Delta = 0.26$ and the effective size is 1:0.45. Thus, the perturbation accounts for 69% of the probability distribution below 4.4Δ but 0.025% overall. The bottom plot in figure 3.6 provides this alternate definition of the perturbation size, which is independent of $(\Omega_D/\Delta)^3$.

Consider the large perturbation peak $a:b = 1:8$. A sufficiently large peak almost ensures that every relaxation phonon will be the same energy. A high-energy quasiparticle will continue to emit nearly identical phonons until it has insufficient energy to do so. In this way, the absorber is behaving like a *perfect quantizer*. Clearly, it is very desirable to locate such a peak just above 2Δ. This will convert a small number of

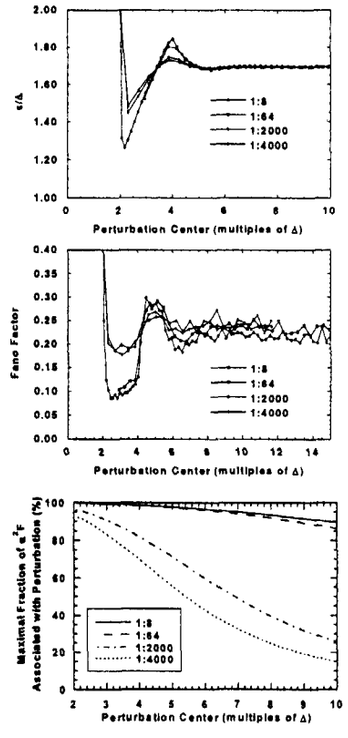

Figure 3.6: Cascade statistics ε (top) and F (middle) for a perturbed-quadratic α^2F function defined in equation 3.8. The ratios $a:b$ of perturbation area to area under the quadratic was 1:8, 1:64, 1:2000, and 1:4000. Points with the same area have been connected to improve the clarity of the plot. The bottom plot indicates the effective size of the perturbation for the special case of a relaxing quasiparticle located $1\ \Delta$ above the perturbation.

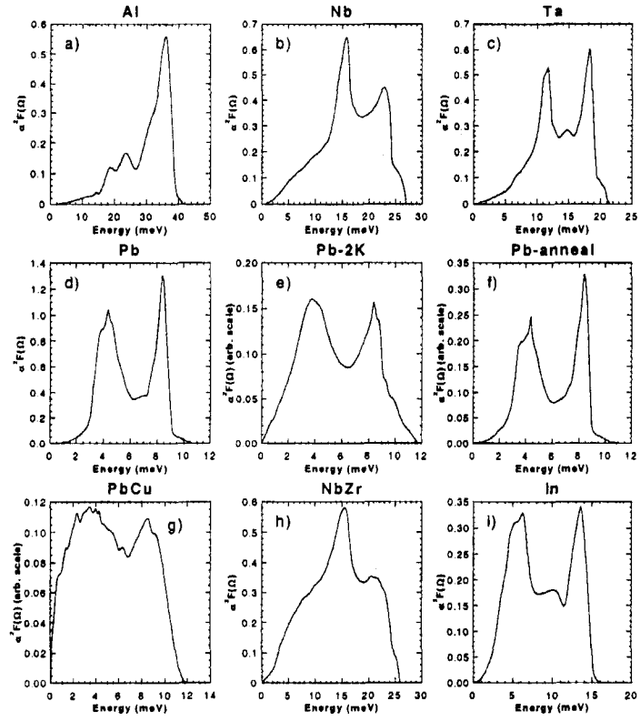

Figure 3.8: Electron-phonon coupling functions used to generated the cascade statistics in table 3.1. a) aluminum; b) niobium; c) tantalum; d) lead; e) lead deposited at 2 K and measured without warming; f) as e), but measured at room temperature (annealed); g) $Pb_{0.9}Cu_{0.1}$ alloy; h) NbZr alloy; I) indium. Data for cold-deposited Pb and $Pb_{0.9}Cu_{0.1}$ are on a normalized scale. The low energy tail of aluminum was not actually measured and is assumed to be quadratic up to 10 meV. See table 3.1 for the origins of these functions.

Material	Δ (meV)	ε (meV)	ε/Δ	F ($10^3\sigma_F$)
Nb[a]	1.55	2.64	1.71	0.214 (2)
NbZr[b]	1.83	3.18	1.74	0.223 (4)
Pb[a]	1.40	2.23	1.59	0.140 (2)
Pb deposited at 2K[c]	1.39	2.45	1.76	0.251 (5)
Pb as above, annealed[c]	1.35	2.20	1.63	0.155 (3)
$Pb_{0.9}Cu_{0.1}$[c]	1.33	2.54	1.91	0.284 (4)
In[a]	0.56	0.94	1.68	0.210 (3)
bcc Ta[a]	0.72	1.27	1.76	0.230 (5)
Al[a]	0.17	0.29	1.70	0.216 (4)

Table 3.1: Cascade statistics for various materials. The final value in parentheses is the uncertainty in the last digit of the Fano Factor. The entry "Pb as above, annealed" was deposited at 2 K, then warmed to room temperature. The Pb statistics cover a wide range due to sub-gap structure and a fortuitously located peak in the electron-phonon coupling.

NbZr alloy also has shifted phonon modes to lower energy, but the extra modes are all between 2Δ and 8Δ. The positive and negative effects over this region have apparently averaged to very little net change. Finally, consider indium. It has an α^2F similar to that of lead, but a smaller gap. As a result, the phonon peak is at too high an energy to affect the cascade statistics.

3.6 Multilayer Cascade

This section continues to expand the model of the cascade process by accounting for the multilayered structure of the STJ detector. The LLNL STJ detector design intentionally uses superconductors with different energy gaps to confine quasiparticles near the tunnel junction. Since the absorber material is very thin and adjacent to the trap material in a stacked geometry, the cascade may occur within both materials simultaneously.

[a] Kotkevich[51]
[b] Wolf and Noer[52]
[c] Knorr and Barth[53]

range of 7Δ to 9Δ is twice that of the previous case. Thus, the average yield is reduced. Furthermore, there are at least two outcomes at every energy above 3Δ, resulting in an increase in cascade noise.

Material dependencies

The preceding sections have demonstrated that low-energy structure in the electron-phonon coupling can lead to either desirable or undesirable cascade statistics. Quasiparticle yield may be either increased or decreased, and cascade noise may be enhanced or reduced. Furthermore, the term "low-energy" may now be understood to be energies less than 8Δ. Using the simple Debye model may be justified for materials like niobium and tantalum, which have no low-energy structure, but other materials, such as lead, must be explicitly examined.

The α^2F functions of several superconductors are shown in figure 3.8. Also included are alloys and amorphous materials. This is to emphasize that material purity and disorder *can* result in cascade statistics that are quite different than one might expect. The corresponding cascade statistics of these materials are given in table 3.1. Most of the pure materials are close to the standard Debye-BCS result. The exceptions are the alloys and Pb. Lead is a strong-coupling superconductor with a large gap and low-energy structure in the electron-phonon coupling function. As noted previously, these characteristics are not independent. The α^2F of lead has a peak at about 4 meV, which is near 3.3Δ. This is an ideal position for low-noise cascades, as well as some slight enhancement of quasiparticle yield. However, the amorphous Pb and $Pb_{0.9}Cu_{0.1}$ alloy have substantial sub-gap states which results in inefficient quasiparticle generation. The

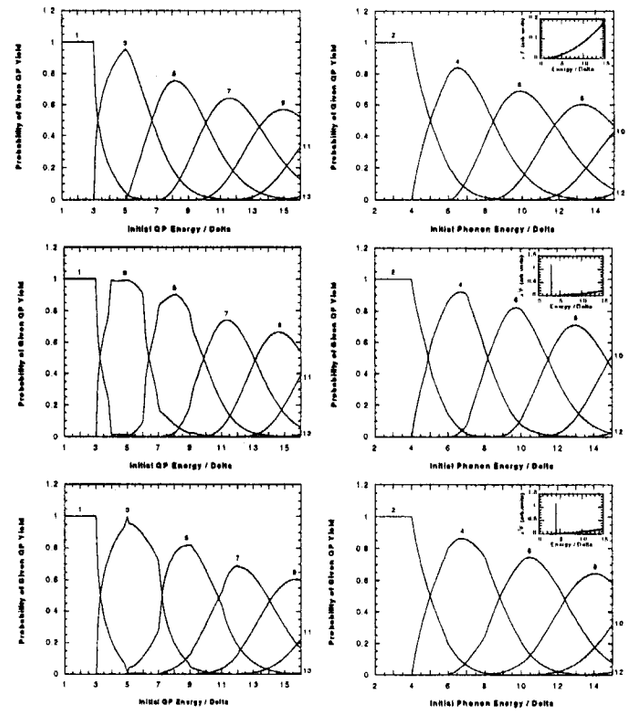

Figure 3.7: Probabilities of an initial energetic quasiparticle (left) or phonon (right) producing a specific number of additional quasiparticles after all daughter particles have relaxed or been lost. The final number of quasiparticles is indicated next to each curve. Each row is a different α^2F model (insets): (top) baseline Debye-BCS model; (middle) peak at 3Δ, corresponding to minimum F; (bottom) peak at 4Δ, corresponding to maximum ε. Notice that in the low F case, there is only one significantly probable outcome for many energies. In the high ε case, low-yield outcomes persist over a wide range of energies.

is very thin. The first calculations of the multilayer model are simple bi-layer junctions. These bi-layers are considered to be deposited on infinitely thin membranes through which phonons cannot travel. Since the phonons cannot escape, they must eventually break a Cooper pair in one layer or the other. The layers are identical, and both have properties of the bulk material. Therefore, the cascade statistics should be identical to those calculated in the previous section. The first and third entries of table 3.2 show that this is the case.

Configuration	Δ (meV)	ε (meV)	ε/Δ	F	% lost	P_{PB}/P_{ESC}
100 nm Nb (membrane)	1.55	2.63	1.69	0.219	41%	16.4
100 nm Nb (substrate)	1.55	2.63	1.69	0.200	41%	12.3
100 nm Al (membrane)	0.17	0.288	1.69	0.201	41%	0.116
100 nm Al (substrate)	0.17	0.508	3.00	2.34	67%	0.068
50 nm Al (substrate)	0.17	0.772	4.54	3.30	78%	0.034

Table 3.2: Monte Carlo results for bi-layer tunnel junctions. The percentage lost is the amount of energy that could not be used to create quasiparticles, either because the phonons had insufficient energy or they escaped to the substrate. The ratio P_{PB}/P_{ESC} is the ratio of the probability of a 2Δ phonon breaking a pair in the bottom layer to the probability of escaping to the top layer (if on a membrane) or to either the substrate or top layer (if on a substrate).

The calculations were repeated, this time possibly allowing phonons to cross into a silicon dioxide substrate. These results are also tabulated in table 3.2. Energy loss due to escaping phonons is reflected as an increase in ε. One finds little change in the result for niobium. Aluminum, however, shows a large effect that depends on thickness. That is because phonons may cross the thickness of a film, perhaps several times if reflected at the interfaces, without breaking a Cooper pair. The probability of breaking a Cooper increases with increasing electron-phonon coupling and increasing gap. The probability of escape increases with increasing film thickness and interface transmission. Aluminum has weak electron-phonon coupling and a very small gap, so many energetic phonons escape. Niobium has strong coupling and a large gap, so only sub-gap phonons escape.

The relative probabilities of pair-breaking and escape for several configurations are tabulated in appendix A.

The bi-layer calculations demonstrate that a lossless multilayer will generate the same cascade statistics as the original lossless single-layer calculation, as expected. They also demonstrate that phonon loss can be especially severe in aluminum bi-layers, also as expected. The quasiparticle yield calculated for aluminum is similar to the result calculated by Brink. [18] His estimate for ε is slightly higher, but he was also including a hot-spot model that increased sub-gap phonon production.

The first STJ model to be tested is simply a four metal layer device, Nb-Al-AlO_x-Al-Nb on an SiO_2 substrate. The two superconductors in intimate contact modify the other's properties. This is known as the *proximity* effect and will be dealt with in detail later in the chapter. It is assumed for this model that each layer possesses the bulk properties of that material, scaled according to the measured gap energy. Other aspects of the proximity effect have been ignored. This model was tested for our most frequently used SIS junctions, which have 50 nm or 200 nm-thick aluminum traps. The results are shown in table 3.3.

Trapping Model	Δ_{trap} (meV)	ε (meV)	$\varepsilon/\Delta_{trap}$	ε/Δ_{Nb}	Fano Factor	Gain
50 nm Trap	0.70	1.76	2.51	1.13	0.269	1.5
200 nm Trap	0.35	0.640	1.83	0.413	0.310	4.1

Table 3.3: Results of a Monte Carlo calculation for a simple symmetric four metal layer (Nb/Al/AlO_x/Al/Nb) detector configuration. The gap of the aluminum has been modified by the proximity effect, but other aspects of the proximity effect have been ignored. The trapping gain is the ratio of the number of quasiparticles produced to the number expected, assuming $\varepsilon = 1.7\Delta_{Nb}$.

These results illustrate three principles. First, the low gap of the trap has encouraged relaxation and pair-breaking to occur within the trap, despite the relatively weak coupling in the trap material. Second, many fewer pair-breaking events occur in

Energetic quasiparticles may relax in the absorber, or travel to the trap and relax directly to the lower gap of the trap. This could result in a more efficient cascade, but also a more noisy cascade if one material is not strongly favored over the other. Furthermore, sub-gap phonons from the absorber are often *super*-gap phonons in the trap, and can continue to create quasiparticles. Finally, two adjacent superconductors modify the properties of each other, so that neither is properly described by the BCS theory. Therefore, the simple Debye-BCS calculation in the previous section should not be considered adequate for inhomogeneous absorbers.

Most prior calculations of the quasiparticle cascade in inhomogeneous superconductors are in the form of finite-difference simulations of quasiparticle and phonon density diffusion. This section approaches the problem from the opposite extreme, which considers quasiparticles and phonons as ballistic particles located somewhere in a layer of material. The following characteristics of an actual detector have been intentionally omitted to simplify the problem:

- Quasiparticles and phonons move as ballistic particles in 1 dimension, with a given average velocity component perpendicular to the layers.
- Quasiparticle loss and phonon downconversion, which may be enhanced at surface and edges, is not considered, nor are losses into the leads.
- Inhomogeneity and anisotropy of the equilibrium superconducting gap within a material is not considered. These properties may affect quasiparticle relaxation rates and transport through the superconductor.
- Phonon absorption by quasiparticles is not considered, which may affect trapping and relaxation rates, and the average quasiparticle velocity.

- The hot-spot or fireball effect, which is believed to occur during the first 100 ps of the cascade, is not modeled.
- Finite reflectivity for quasiparticles between dissimilar metals is not considered.
- Phonon properties are considered to be an average of longitudinal and transverse phonons.

The calculation is designed with the following features:

- The calculation is a Monte Carlo simulation of the production and relaxation of quasiparticles from an initial population of acoustic phonons.
- For both quasiparticles and phonons of a given energy, the average time between interactions is compared with the time to cross the thickness of a layer to give a probability an interaction to occur in each layer.
- Quasiparticles are assumed to travel though all accessible layers several times before relaxing in one of them. Phonons usually have a very short interaction time, and are modeled as hopping from one layer to the next.
- Finite reflectivity for phonons at each interface increases the phonon escape time. The tunnel barrier is considered to be too thin to affect phonon transmission.
- The calculation models an arbitrary arrangement of dissimilar superconductors and barriers. The presence or absence of a substrate is included by specifying the phonon transmission from the bottom layer into the substrate.

This calculation differs from the traditional model by considering the cascade and trapping processes together. Each quasiparticle can now relax into either the absorber or the trap from high energy. Since the relaxation rate is proportional to ω^3, quasiparticles are very likely to relax directly into the trap rather than the absorber, except when the trap

The loss of these intermediate phonons has been considered to be a substantial loss mechanism. Instead, one can expect that most of this energy will be recovered, particularly when the energy is deposited in top niobium layer and must traverse these proximitized layers to escape into the substrate. This implies three things: that the hot-spot effect may not be important if such phonon-trapping layers are present, that accurate modeling of the hot-spot is not necessary and simple models will suffice[*], and finally that neglecting the hot-spot effect in these calculations was justified.

The BCS density of states is a poor representation of the proximitized system, so the above calculations were repeated using the quasiparticle Green's functions calculated from a proximity model. [55] The density of states and coherence terms are expressed in terms of the spatial average of the proximitized Green's functions. Both the gap and the averaged Green's functions are taken to be constant over the proximitized area. Also, the proper α^2F functions presented in the previous section are used. A much more realistic model is achieved by using these material- and construction-dependent functions.

The results shown in table 3.5 are similar to the simple proximity model. This is because the accurately modeled proximitized niobium layer is still able to trap almost all phonons that escape from the aluminum. There is about 10-20% difference between the two calculations. Use of the simple proximity model is recommended as it requires much less computational effort.

Realistic Model	Δ_{trap} (meV)	ε (meV)	$\varepsilon/\Delta_{trap}$	ε/Δ_{Nb}	Fano Factor	Gain
50 nm Trap	0.69	1.52	2.20	0.981	0.252	1.8
100 nm Trap	0.50	1.06	2.11	0.684	0.325	2.7
200 nm Trap	0.34	0.648	1.91	0.418	0.205	4.5

[*] It has been suggested that aluminum is more susceptible to the hot-spot effect, and there is no efficient mechanism to capture sub-Al-gap phonons[18].

Table 3.5: Results using a realistic proximity model to describe the proximitized Nb and Al layers.

Finally, the variation of the cascade statistics with the trap gap and thickness is shown in figure 3.9. One can see that the discrepancy in ε between the simple and realistic proximity models is actually quite small on an absolute scale. Another thing to note are the peak in ε/Δ near 50 nm and the peak in F near 100 nm. These are easily understood in light of the earlier analyses in this chapter. The increase in ε/Δ is due to the fact that most of the relaxations are occurring in the unproximitized niobium while Δ_{trap} is decreasing. As the trap comes to dominate the relaxation process, ε/Δ begins to decrease. The increase in F at 100 nm is easily understood by recognizing that the gap is at the threshold of allowing quasiparticle multiplication by fully relaxed quasiparticles in the niobium. The uncertainty of multiplication at the threshold results in increased cascade noise. It peaks at 100 nm because thicker traps have a lower gap, and multiplication is very likely, while thinner traps have higher gaps, and only energetic quasiparticles are capable of multiplication.

The multilayer Monte Carlo calculation also lends itself to investigating another issue: the small but measurable variation in quasiparticle yield depending between absorptions occurring in different layers. X rays with energies <= 500 eV are almost always absorbed in the top niobium layer, which is 160 nm thick. X rays with energies >= 2000 are absorbed in both niobium layers in proportion to their thicknesses. The STJ signal is slightly different depending on which layer the absorption occurs. Furthermore, niobium is relatively transparent to x-rays between 100 and 200 eV. These x-rays may be absorbed in *any* of the niobium or aluminum layers. Thus, a monochromatic x ray source

the aluminum because the thickness of the traps is much less than the phonon mean free path for pair-breaking in aluminum. As a result, energy that could have been used to break Cooper pairs has been lost into the substrate. Finally, the number of quasiparticles produced differs significantly from the traditional model. For the 200 nm-thick trap device, the traditional model expects multiplication during trapping to be possible. The energy gap of the trap is between 1/5 and 1/3 of the gap in the absorber, so each quasiparticle may break at most one Cooper pair in the process of trapping. The maximum possible multiplication factor is therefore three. This new calculation predicts greater multiplication by converting energy into trapped quasiparticles more efficiently. The traditional model allows no multiplication in the device with 50 nm-thick traps at all, but an increase of 50% is predicted when allowing the cascade process to occur in both materials simultaneously.

The next calculation will now include the modification of superconductor properties by adjacent superconductors, known as the *proximity effect*. Superconductor properties are able to vary spatially over a distance called the *coherence length*, which is related to the electron mean free path. This is quite short in our polycrystalline niobium, about 30 nm, and somewhat longer in our aluminum, about 300 nm. Modeling of the proximity effect in Nb-Al bi-layers suggests that the gap in the niobium is suppressed near the interface but with the properties of the bulk material away from the interface, while the gap in the aluminum is elevated and nearly constant throughout the film. The proximitized niobium region cannot be ignored for two reasons: 1) the width is comparable to the thickness of our trapping layer in many of our devices, so that the trap volume is increased, and 2) the phonon coupling to low energy quasiparticles is much

stronger in the niobium than in the aluminum traps. [54] Therefore, the first refinement to the previous calculation will add a 30 nm-thick Nb film with a reduced gap. Again, the other aspects of the proximity effect will not be included. The most important aspect is that the density of states at the interface, between the proximitized and bulk gap energies, is much smaller than the BCS density of states. In particular, there is no singularity at the energy gap. Thus, the effects of this BCS-like proximity layer are expected to be exaggerated somewhat. Specifically, quasiparticles will relax closer to the gap in this model than in the actual material, and the relaxation phonons will be slightly larger.

Proximity Model	Δ_{trap} (meV)	ε (meV)	$\varepsilon/\Delta_{trap}$	ε/Δ_{Nb}	Fano Factor	Gain
50 nm Trap	0.68	1.37	2.01	0.884	0.289	1.9
100 nm Trap	0.50	0.858	1.71	0.554	0.307	3.1
200 nm Trap	0.37	0.620	1.69	0.400	0.216	4.2

Table 3.4: Results for the six-layer model, in which the niobium and aluminum layers are separated by one coherence length of reduced-gap niobium. This layer increases the yield of detectors by absorbing phonons that escape the relatively thin aluminum traps.

The cascade results using this model are summarized in table 3.4. Comparison of raw results in appendix A reveals that the thin layer of reduced-gap niobium is more effective at trapping phonons and quasiparticles than even the 200 nm aluminum layer. The total quasiparticle yield is substantially increased for devices that would otherwise lose intermediate gap phonons from the aluminum traps. In other words, the proximitized layer acts as a barrier to phonon loss and increases the efficiency of energy conversion into quasiparticles. An important conclusion is that a proximitized layer such as this would absorb intermediate energy phonons produced in an initial niobium hot-spot.

modified version of this simulation. [56] First, energetic quasiparticles with a scattering time approximately equal to time to ballistically cross the layer thickness are assumed to relax in that layer. Second, a small fraction of the quasiparticles that may enter the top niobium layer are lost along with all their energy. This emulates some undefined quasiparticle loss mechanism; an example is the formation of normal metal oxides of niobium. The fit had two adjustable parameters: the ratio of scattering time to transit time that resulted in confinement, and the fraction of quasiparticles that are lost from the top layer. It was possible to fit peaks corresponding to the top niobium and both aluminum films exactly, and to predict the location of the peak corresponding to the bottom niobium film.

Conclusion

These calculations have shown that the standard cascade statistics, $\varepsilon = 1.7\Delta$ and $F = 0.2$ may be correct for most materials, but not all. Materials for which this assumption is appropriate will have electron-phonon coupling that is smoothly increasing with respect to phonon energy, be quadratic below 2Δ, and be free of peaks or other structure below 10Δ. This is true for most pure materials. A systematic study of the role such structures play in the cascade reveals that coupling peaks between below 6Δ will have a substantial effect on the cascade statistics. Quasiparticle cascades in very strong-coupling superconductors like lead and mercury may be completely different from those within the more ordinary superconductors. The Monte Carlo simulations of materials like amorphous lead show that the cascade statistics can be heavily dependent on the film quality beyond previously established issues such as trapping, loss, and mean free path.

From an x-ray spectrometer point of view, these effects can be either beneficial or detrimental, depending on the exact form of the coupling at low energy.

Just as the cascade statistics depend on the absorber material and the material quality, so do they also depend on the absorber geometry. Under assumptions that are reasonable for thin films, the calculations for multilayer absorbers in this chapter demonstrate that neither $1.7\Delta_{abs}$ nor $1.7\Delta_{trap}$ are reasonable estimates for the cascade ε statistic, except in limiting cases. Furthermore, the calculations predict that sub-niobium-gap phonons created within a niobium hot-spot will be efficiently captured, negating much of the effect of the hot-spot. An accurate multilayer simulation is required if one desires a valid estimate of noise intrinsic to a multilayer STJ detector.

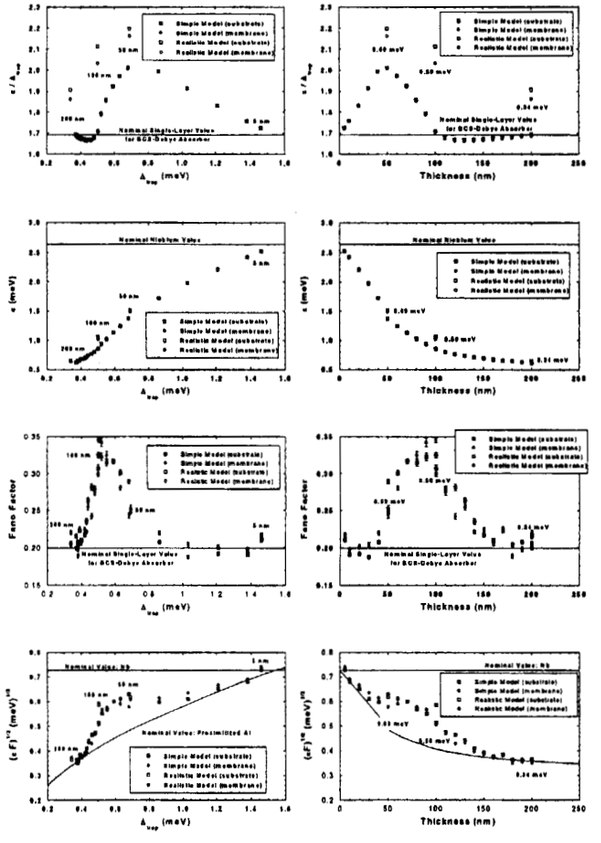

Figure 3.9: Plots of $\varepsilon/\Delta_{trap}$ (first row), ε (second row), F (third row), and $(\varepsilon F)^{1/2}$ (fourth row) vs. the proximitized gap (left column) and trap thickness (right column). Note that $(\varepsilon F)^{1/2}$ is a factor in the theoretically achievable FWHM (see equation 3.3).

	base Nb	prox. Nb	Al	Al	prox. Nb	counter Nb
QP Yield per keV	647890	652174	655831	704750	712100	708258
Normalized Yield	0.915	0.921	0.926	0.995	1.005	1.000

Table 3.6: Quasiparticle yields where the initial phonon population is located in one of the six layers of the simple proximity multilayer model (50 nm-thick traps on substrate). Note that the proximitized niobium layers are too thin to generate an appreciable number of events.

may produce one, two, or four spectral peaks, which complicate the spectrum. The differences in the signal sizes is small, so the peaks may overlap to form a broad and/or asymmetric peak. A spectrum demonstrating this is shown in figure 5.15, where this effect is discussed.

The Monte Carlo calculations using the simple proximity model were repeated, but with the initial phonon population appearing in layers other than the top niobium layer. The traps were 50 nm thick and a substrate was present in this calculation. The quasiparticle yields for each initial layer are listed in table 3.6. The calculation predicts an 8.5% decrease in signal between the top and bottom niobium layers, primarily due to phonon loss through the substrate but also due to the Nb/Al volume ratio being different for each side.

The predicted signal amplitudes are within the appropriate range for the observed splitting of spectral peaks. However, we observe that, for the LLNL devices, the bottom Nb layer generates the larger signal, as well as the best energy resolution. As with most thin film devices, the uppermost layers that were deposited last are of lesser quality than the earlier layers below them. The inversion of the peak splitting indicates that the difference in quasiparticle yield is due to the greater quasiparticle losses in top layer. The splitting of a line into four distinct peaks in the niobium window has been fit by a

The experimental workspace contains the ADR, the STJ detector, and the detector support apparatus. A schematic of the essential elements is shown in figure 4.2. The ADR magnet is recessed into the LHe tank, though not immersed as is common in many designs. The active component of the ADR is connected to an OFHC (oxygen-free, high-conductivity) copper rod which conducts heat in and out of the refrigerator. The slightest touch to a 2 K component will render the ADR useless, particularly if the touch is a low-resistance electrical contact. The millikelvin components, or "cold-stage", are suspended by 50 lb. kevlar string as shown in figure 4.3. The OFHC copper rod is clamped to a platform which holds calibrated thermometers, electric heaters, and occasionally the components being tested.

STJ detectors generally require a weak but well-defined magnetic field for normal operation. The detectors are mounted within a 4 cm diameter superconducting electromagnet which in turn is enclosed completely by a Cryoperm 10 magnetic shield to block the earth and ADR fields. [58] As with the ADR cold stage, this detector mount is supported by kevlar strings as shown in figure 4.4. The kevlar strings are threaded in a criss-cross pattern through the arms of the detector support, called the crab, and two plates that are separated by compressed springs. The kevlar is kept under tension because kevlar expands when cooled below room-temperature. The criss-cross pattern should ensure that all arms of the crab move identically when the kevlar expands, so that the detector orientation with respect to the applied magnetic field does not change. The crab is attached to the cold-stage via a copper braid.

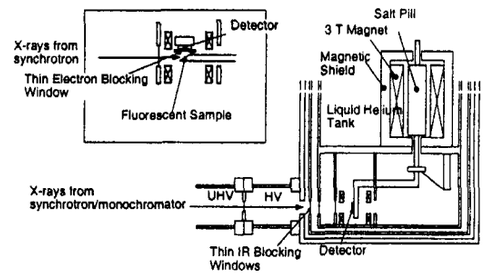

Figure 4.2: Schematic diagram of the cryostat, also illustrating the detector mounting for direct illumination and for secondary fluorescence measurements.

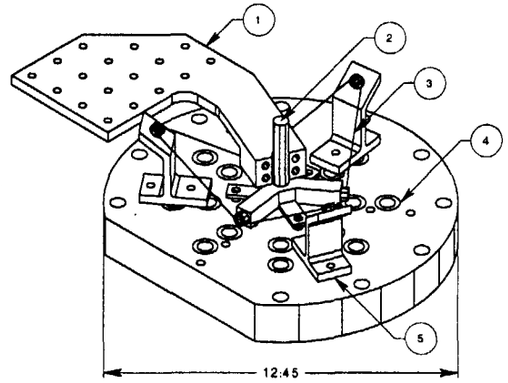

Figure 4.3: ADR magnet cover and millikelvin feedthrough and "cold stage". The central copper rod extends from the FAA salt pill which is suspended in the core of the magnet. This suspension is accomplished by wrapping a kevlar string around six pulleys as indicated and fastening under tension. An identical support completes the suspension at the other end of the magnet. The cold stage, which contains thermometry and heating elements, is clamped to the copper rod (half of the clamp is omitted from the drawing).

Chapter 4

Experimental Setup

4.1 Introduction

In this chapter the experimental setup and the operating procedures will be described. The first part treats the cryostat and in particular the adiabatic demagnetization refrigerator which is used to obtain the low temperatures that are required to operate the STJs. The next section is devoted to the infrared filters that have been used in the synchrotron measurements. Also calculations of the effect of the magnetic shield on the magnetic field will be presented. Finally, the analog and digital data acquisition and electronics readout will be briefly described.

4.2 Equipment Descriptions

Cryostat

A cryostat differs from a simple dewar in that it is designed to cool to and regulate temperature at low temperatures with great precision. Our cryostat was manufactured by Infrared Laboratories. [57] Liquid helium is used at low pressure to reduce the temperature within the cryostat below 2 K. The cryostat is equipped with an adiabatic demagnetization refrigerator (ADR) which can cool detectors to 50 mK. The heat capacity of solids at these temperatures is very small, so all forms of heat conduction, including radiation and physical contact, must be carefully managed.

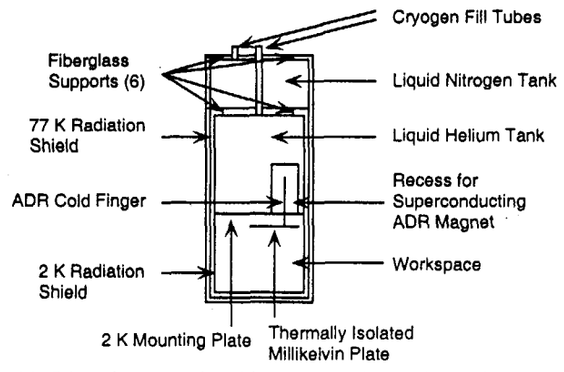

Figure 4.1: Schematic cross-section of the cryostat used to test the STJ detectors.

Our cryostat measures 28" in height by 12" in diameter. Most of this space is occupied by a 6 L liquid nitrogen (LN_2) tank and a 12 L liquid helium (LHe) tank. The remaining space is available for conducting experiments and is in direct contact with the LHe tank. All LHe temperature components are enclosed in an aluminum shell that is attached to the LN_2 tank. This shell is not vacuum-sealed, but is sealed against 300 K radiation. The experimental area is likewise completely enclosed and light-sealed against 77 K radiation. The exterior of the LHe shell is covered with a layer of mylar superinsulation to further decouple the LHe stage from the LN_2 stages. The interior is coated with carbon-filled epoxy to absorb any external radiation that leaks into the workspace. Also, activated charcoal is attached to the 2 K surface to adsorb residual nitrogen and helium gas. When the pressure of the LHe in the tank is reduced by a large mechanical pump, the temperature of the LHe stage can reach 1.9 K. All electrical wires are heat sunk at each temperature stage.

Adiabatic Demagnetization Refrigerator

The ADR is a very simple device that can reach temperatures as low as a few millikelvin. This simplicity makes the ADR inexpensive and easy to maintain and operate in comparison to the ^{3}He dilution refrigerator. The ADR operates through the isothermal magnetization and adiabatic demagnetization of a paramagnetic salt. In the LLNL ADR, the salt is ferric ammonium alum (FAA). The net effect of this cycle is to transfer heat from the millikelvin stage to the LHe bath. The cycle is shown in figure 4.6: [59] At relatively high temperatures the magnetic dipoles of the paramagnetic salt are randomized and the specific entropy $S_0 = R \ln(2J+1)$, where J is 5/2 for FAA and R is the ideal gas constant. The salt is thermally connected to the LHe bath by a mechanical heat-switch and a strong magnetic field of magnitude B_a is applied. The entropy decreases to $S(B_a,T_i)$ and the heat of magnetization $S(B_a,T_i)\,T_i$ is released, where T_i is the temperature of the LHe bath. This heat is conducted away through the thermal connection to the bath. The heat switch is opened, which isolates the salt from the LHe bath. The magnetic field is then reduced to zero in a smooth manner. When the applied field reaches zero, the salt reaches a final temperature T_f, and gradually warms along the curve $S(0,T(t))$. In general, the total cooling energy of one ADR cycle parameterized over time is

$$Q = \int_0^\infty \dot{S}(B(t),T(t))T(t)dt\,. \qquad 4.1$$

Three important things should be noticed. First, there is a minimum temperature, T_{min}, at which the applied field equals the internal magnetic field. Further reduction of the applied field does not result in additional cooling. For FAA, this temperature is about 30 mK. [59] Second, if the magnetic field is not reduced completely to zero then the

ADR can hold the temperature constant by slowly reducing the field, or change the temperature to higher or lower values at any time. Third, if the temperature is regulated at a constant temperature above T_{min} then the ADR is able to absorb a far greater amount of energy and the *hold-time* is greatly increased.

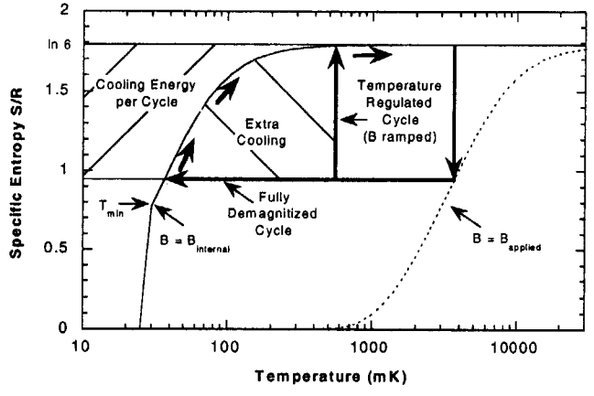

Figure 4.6: Thermodynamic cycle of an ADR. The solid and dotted curves are the entropy curves as a function of temperature with and without an applied magnetic field, respectively. Magnetization releases $\delta S T_i$ in heat. After demagnetization, the parametric salt absorbs heat equivalent to the shaded area to the left of the $B=0$ curve. If B is not reduced to zero, but slowly decreased to hold T constant, then additional heat can be absorbed (note logarithmic temperature axis). The minimum obtainable temperature is near the ordering temperature T_{min}, where the entropy drops sharply with temperature.

In the LLNL cryostat, the ADR is capable of reaching 50 mK and absorbing 18 mJ of heat. The applied field is generated by a 3 T superconducting magnet. The FAA salt is suspended within the bore of the magnet, as shown in figure 4.2 and figure 4.3. The magnet is contained within 0.5" thick vanadium permendur shielding so

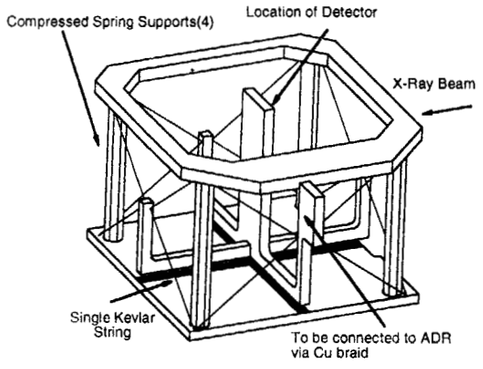

Figure 4.4: Drawing of the support mechanism of the sub-Kelvin stage. The aluminum frame is nominally at 2 Kelvin. The low-temperature stage (or "crab") is gold-plated OFHC copper. A single Kevlar thread (50 lbs. weight) is threaded between opposing corners through small holes in the arms of the crab. The magnetic shield descends around the central post of the crab. Because Kevlar expands below room temperature, the vertical posts are under compression with steel springs. The crab is aligned by hand and each crossing of the strings is dabbed with a small amount of cyanoacrylate adhesive. It is hoped that the expansion of the Kevlar will only raise the crab slightly without twisting or tilting in this configuration.

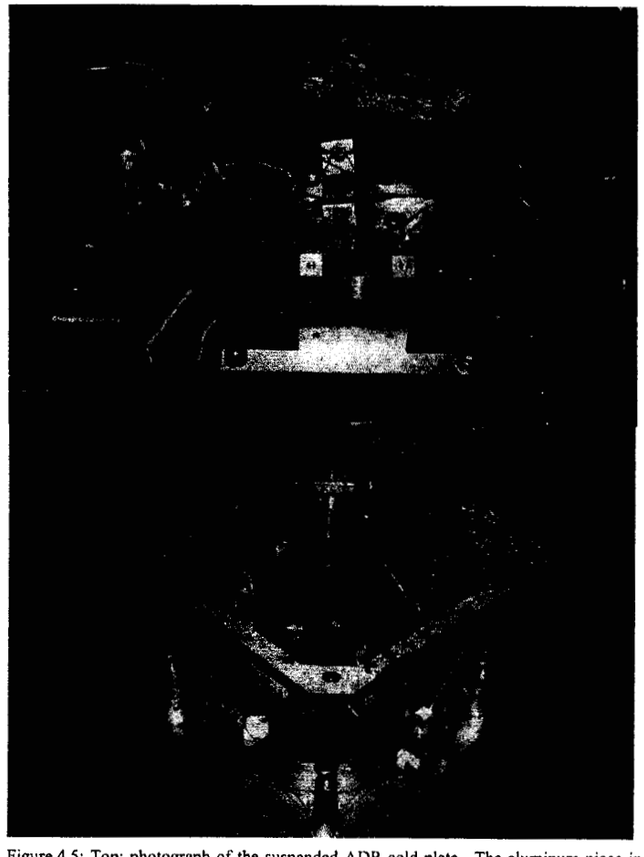

Figure 4.5: Top: photograph of the suspended ADR cold plate. The aluminum piece in the foreground supports part of the fluorescence sample loadlock, the opening for which is currently covered with aluminum tape. The cold stage is shown clamped in the jaws of the heat switch in the lower left corner. Bottom: photograph of the "crab." Detectors are mounted on the center post. The copper braid is attached to the cold plate.

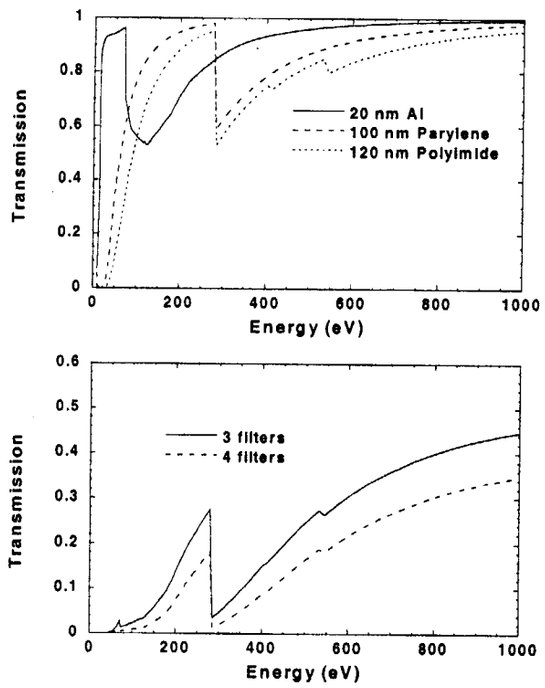

Figure 4.7: Top: the transmission of aluminum, parylene, and polyimide films that comprise the infrared filters. Bottom: the net transmission of three (solid) and four (dashed) filters constructed from 200 Å aluminum deposited on 1000 Å parylene.

Experiments at the Stanford Synchrotron Research Laboratory (SSRL) required an additional film that isolated our cryostat vacuum from the UHV vacuum of the synchrotron beam. We use a 1200 Å polyimide ($-C_{22}H_{10}N_2O_5-$, $\rho = 1.43$ g/cm^3) film from Luxel, [65] mounted within a vacuum gate valve from VAT. [66]

The calculated transmissions of the mylar, parylene, and polyimide filters are plotted in figure 4.7. [67] The effect of the nickel meshes is dependent upon the particular geometry of the experiment and is not included here. There is the possibility of attenuation due to adsorbed oxygen and nitrogen which is addressed in chapter 6.

Filter Radiation Damage

Aluminum filters are expected to degrade within hours of deposition due to oxidation [68] with subsequent degradation occurring over a period of years. But, the combination of intense synchrotron radiation exposure and adsorbed gases in our cryogenic system may greatly accelerate the formation of transparent aluminum oxides and nitrides. We observed physical changes in the parylene filters almost immediately after they were exposed to synchrotron radiation. The filters normally have a slightly rough appearance, but the became very smooth at the location where the beam x-ray beam passed through the filters. Under normal operating conditions we do not observe a change in the ADR performance from before and after the first exposure to radiation. However, an experiment that exposed the filters to intense zero-order (reflected) light from the monochromator for over 30 minutes resulted in a spot that was visibly more transparent to the eye, and a reduction in the ADR hold time was noted.

Electronics

The STJ was operated with the circuit shown in figure 4.8. This circuit provided a constant bias current at low frequency. The DC bias current and voltage were monitored with INA110 instrumentation amplifiers. The junction was coupled at high frequencies through a 5 μF blocking capacitor to a low-noise trans-impedance pre-amplifier. [69] The trans-impedance pre-amplifier converted the pulse of excess quasiparticle current

that the field does not escape and affect the STJ operation. When the ADR magnet is energized to 3 T, the shield keeps the field at the detector below 1 G. [60]

Infrared Filters

Early tests of the STJ spectrometer were made with sealed ^{55}Fe electron-capture sources, which emit manganese K x rays. However, to test the spectrometer at lower energies, and particularly at sub-keV energies, it was necessary to use an external source of radiation. Thus, holes had to be made in the shells attached to the LN_2 and LHe storage tanks. Each hole is covered with a filter that transmits most of the low-energy x rays but reflects infrared radiation. The heat capacity of solids at millikelvin temperatures is incredibly small and an IR light leak would render the ADR inoperable.

For these experiments we selected thin-film plastic filters with aluminum coatings. In early experiments with photon energies above 1 keV we used 2.5 μm mylar films with an estimated 130 Å aluminum coating. [61] This estimate was made from the measured resistance per square of 2 Ω. One filter is mounted on the LN_2 shell and one on the LHe shell. Because the thin aluminum film does not conduct heat very well, it is possible that the temperature at the center of the filter is elevated. [62] A third filter is mounted on the wall of the detector's magnetic shield to block the direct path of IR light that is transmitted through or radiated by the other filters.

The mylar filters are too thick to conduct experiments at x-ray energies below 1 keV. Therefore, we used 1000 Å parylene-N ($-C_8H_8-$, $\rho = 1.11$ g/cm^3) filters with 200 Å aluminum coating from Lebow, Inc. [63] These filters are supported by an 80% open Ni mesh and are expected to withstand a pressure difference of 10 Torr. We

discovered that the third filter on the magnetic shield was absolutely necessary when using these thinner filters, otherwise an ADR cycle lasted only an hour.

A fourth filter is placed between the detector and the target in fluorescence measurements (see figure 4.2, inset). The fluorescence efficiencies of x-ray lines below 1 keV are only of the order of 0.1 - 1.0%. Most of the absorbed beam energy is released as photoelectrons and Auger electrons. The STJ detector is sensitive to any form of energetic particle and would be overwhelmed by the emitted electrons if they were not blocked. This fourth filter blocks those electrons at the expense of additional attenuation of radiation. We used CASINO, [64] a Monte Carlo simulation package for determining secondary electron and x-ray production in a scanning electron microscope, and found that the parylene should stop ~500 eV electrons completely.

We also confirmed the presence of the electrons by replacing the fourth filter with an electrified grid. At zero voltage the fluorescence spectrum was a broad, almost random distribution of pulse heights. The spectrum became sharper as a negative voltage was applied to the grid. Unfortunately, there was not enough space between the fluorescence target and the detector to operate the grid at full voltage without electrical arcing that destroys the fragile tunnel barrier. As such, a parylene filter was used for all actual fluorescence measurements.

define a component tangential to the junction. The geometry defining these components is shown schematically in figure 4.9.

The results of the calculation are plotted in figure 4.10. The field strength is normalized to the field of an infinite solenoid with identical turn density, diameter, and current as the solenoid being modeled. The maximum axial field of the test solenoid, which has been enhanced by the magnetic shield, is approximately equal to this value. The calculation revealed that the perpendicular component could be as great as 2% of the nominal field with only a vertical offset. In all cases a horizontal offset increased the amount of perpendicular field. At typical applied fields of 80 G, this corresponds to about 1.4 G. Without the magnetic shield, the distortion is much worse, up to 10% along the vertical axis.

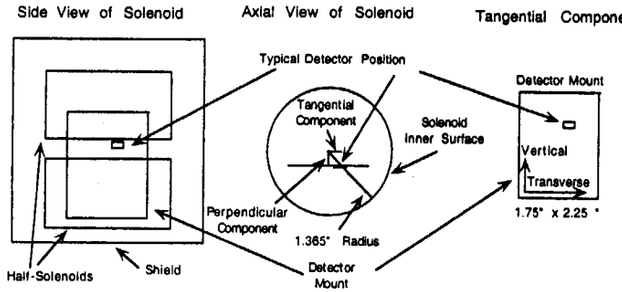

Figure 4.9: Geometry used to describe magnetic field calculation. The transverse component is the radial component that is parallel to the detector junction.

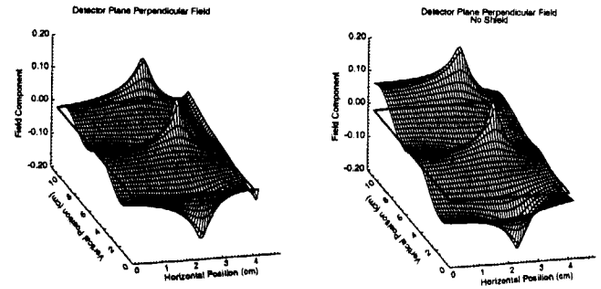

Figure 4.10: Perpendicular component of the applied magnetic field as a function of the position of the detector in the plane of the detector mount. The vertical scale is normalized to the axial field of an infinite solenoid with the same turn density and diameter. The "wavy" nature is the result of having two finite solenoids stacked atop each other. The peaks occur where the detector plane intersects the solenoids' current sheets. The horizontal position is zero when the detector is centered on axis.

4.3 Acquisition Modes

Data can be acquired in three modes: as complete waveforms, as a spectrum of pulse heights, or one can simply measure the number of pulses with heights that fall within a window (single channel analyzer). Each of these techniques is suitable for a different purpose.

Waveform Acquisition

To assess the characteristics of the STJ detector, the complete waveform of the pulses is digitized. We have two waveform digitizers at our disposal: a 10-bit Tektronix RTD-710 with a GPIB interface, a 12-bit GaGe 6012 PCI A/D card. The waveforms are digitized with a timebase of 20-50 ns and saved to the hard-drive of a PC for later processing. To prevent aliasing of high-frequency noise, the detector signal is filtered by a two-stage Ithaco filter-amplifier in low-pass mode at 1 Mhz and a gain of 10. This filtered signal is connected to the digitizer input, properly terminated with 50 Ω. Each pulse is analyzed

into a voltage signal while holding the junction voltage approximately constant during the pulse. The pre-amplifier was based around a IF9030 (InterFET NJ903L process) negative JFET. This FET had 0.5 $nV/Hz^{1/2}$ effective voltage noise at the gate. The open-loop gain of the amplifier in a voltage amplifier configuration was 2.2×10^5. The pre-amplifier was normally configured with negative feedback with a 50 – 200 kΩ feedback resistor. A 5 pF feedback capacitor was required to ensure the stability of the pre-amplifier. The FET, feedback, and bias elements were all operated at room temperature. Electrical power was provided by an array of Gell Cell rechargable batteries.

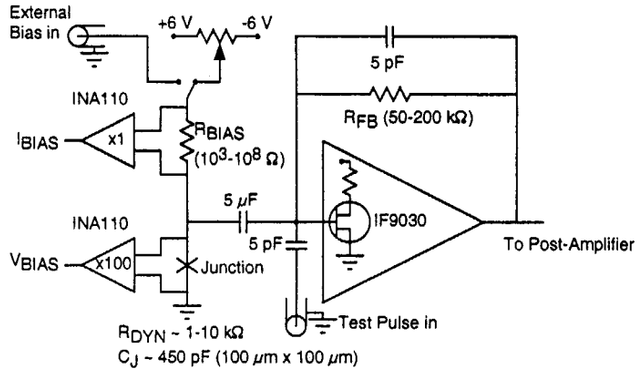

Figure 4.8: Schematic of the STJ bias and amplification circuit. At low frequency the junction is biased by a constant current. At high frequency the junction is biased at constant voltage and the excess tunneling current is amplified to a voltage at the amplifier output.

Parallel Magnetic Field

The sensitivity of the STJ to magnetic fields was described in chapter 2. A magnetic field is applied in the plane of the detector by a solenoid to suppress the zero-voltage supercurrent, while a magnetic shield eliminates other magnetic sources. However, the

applied field is not uniform. The solenoid is divided in half so that x rays may reach the detector. Also, the height of the solenoid is approximately equal to its diameter; it cannot be considered to be a long solenoid. The magnetic shield may straighten the field near the ends, but will distort the field in-between the two solenoid halves. Finally, the detector itself is mounted off axis.

One consequence of a non-uniform field is fairly minor. The modulation function of the supercurrent will no longer follow the diffraction patterns described in chapter 2. Another consequence, however, deserves careful consideration. The perpendicular component of the magnetic field can have a significant impact on the performance of the STJ spectrometer. It leads to the creation of magnetic flux tubes which can trap quasiparticles and increase the junction leakage current. It also creates an additional variable that can vary between measurements.

The field is applied by a solenoid which is 2.75" in diameter and is 3.4" in height. The axial component was measured with a Hall probe at room temperature with the base of the magnetic shield omitted and found to be 0.4 G / mA.

The solenoid-shield combination can be reduced in the axially-symmetric case to a 2-D Laplace equation of a magnetic scalar potential. This equation was solved numerically; the details are given in appendix B. The axially-symmetric calculation describes the vertical and radial components of the field. The detector is not located at the center of the solenoid, nor along a radius. Instead, it is usually in a plane offset 0.9 cm from the center. Thus, the radial component of the field will be divided into parallel and perpendicular components relative to the detector junction plane. The parallel (also horizontal and transverse) and vertical components can be recombined to

to determine the pulse rise and decay times, non-exponential pulse characteristics, and the pulse amplitude. In addition to the x-ray waveforms, approximately 100 waveforms are acquired with no x-rays present and with the trigger set to "AUTO" to determine the nature of the noise in the system. The x-ray and noise waveforms are combined and processed to produce a digital optimal filter. [70] The x-ray waveforms are convolved with this filter and the maximum voltage is computed from a parabolic fit to the filtered waveform.

Diagnostics such as decay time vs. pulse height can be computed with 1,000 waveforms; at least 10,000 waveforms are required to produce a good quality spectrum. Although the latest generation of LabView software for the RTD has increased the its acquisition and transfer rate to about 100 waveforms per second, this procedure was too slow to acquire the spectra shown in this thesis, and is not practical for industrial applications. The use of the GaGe card with machine compiled drivers has increased the acquisition to a much more acceptable 1,000-3,000 waveforms per second.

Pulse Height Analysis

To acquire fluorescence spectra at a faster rate we used a Nucleus pulse height analyzer (PHA) card in a PC, with 8192 channels. Many spectra were measured in a similar configuration as the waveform acquisition mode, except the second filter stage of the Ithaco filter was set to a high-pass filter at 3.15 kHz. This removed low-frequency noise that was removed by the optimal digital filter in the waveform acquisition mode. However, the high-pass filtering produced an under/overshoot ring that appeared in the spectrum, so the lower discriminator of the Nucleus card had to be set above this point.

Filtering with the Ithaco filter provides more variation in filtering so that the signal-to-noise may be optimized. However, the high-pass filter cannot be used for count rates greater than a few kilohertz. Our high count-rate configuration replaces the Ithaco filters with Ortec or Tenelec spectroscopy amplifiers, which produces pulses better suited for counting at high rates. This allows the detector to operate at up to 60,000 counts per second. The spectroscopy amplifiers also feature base-line restore, which greatly reduced the variation in the Nucleus card's measurement of the pulse height, and also pile-up rejection gating.

Single Channel Acquisition

While the greatest utility of the STJ detector lies in the ability to create detailed fluorescence spectra with distinct lines, the electronics can also be configured to generate a count-rate signal without additional processing steps. This technique still takes advantage of the energy resolving capabilities of the detector by allowing you to define a window that excludes strong fluorescence lines near the excitation energy.

Instead of digitizing the pulse or pulse height, each pulse is filtered and input to a single channel analyzer (SCA) or discriminator circuit. The output is a fast +5V pulse that may be input to a CAMAC scaler. The monochromator software can read the number of pulses detected per unit of time and record this with the excitation energy. The SCA can be roughly set by connecting a logarithmic ratemeter to its output, and adjusting the lower discriminator above the noise or (if appropriate) intense lines such as oxygen Kα. A more accurate technique is to estimate the voltage amplitude of the region of interest from the PHA spectrum. The most accurate technique, but least convenient, is to use the Nucleus card itself, which has an SCA output. After acquiring a spectrum, the

upper and lower discriminators of the PHA are set to window only the region of interest. The SCA output of the PHA is input to the scalar as before.

This configuration is also useful when aligning the cryostat. The logarithmic ratemeter indicates what position is exposed to the greatest intensity. For fluorescence experiments, the window can be set to an elemental line found only in the target, allowing the exclusion of fluorescence and scattered light at incorrect beam positions.

Chapter 5

Measured Detector Response

Superconducting tunnel junctions are a promising technology for high-resolution and high-sensitivity radiation detection. X-ray spectrometers using STJs have been in development for as long as 15 years, [71-73] but the technology is now approaching maturity. With this maturity comes the possibility of applying the technology to demanding mainstream applications in industry and academia. This chapter presents several characterizations of detector performance as well as some analyses of behaviors unique to the stacked tunnel junction design and current-following electronics used at LLNL to establish the utility of STJ spectrometers as a high-performance analysis instrument. This chapter will begin with an analysis of the small but observable variations in the signal output by the STJ. This will be followed by a series of measurements characterizing the detector performance over a wide range of incident x-ray energies, the temperature sensitivity of the detector, and demonstrate its operation at high count rates.

5.1 Pulse Shape Variations

Asymmetric Response

The STJ detectors developed at LLNL are essentially stacks of thin-films patterned into a diamond shape. This design has several advantages. It allows the engineering of the energy gap of the middle films via the proximity effect. Also, it is constructed so that the

two junction electrodes double as absorbers. Quasiparticles that are created in the absorbers do not have far to travel before reaching the tunnel barrier. There is now, however, a disadvantage: there are two absorbers in a single detector. As a result, each x-ray line of sufficient energy to be absorbed in both absorbers will appear twice in a spectrum, a phenomena which is referred to as *peak splitting*.

Peak splitting is most easily observed by researchers who operate STJs with the more conventional charge-accumulating pre-amplifier. Possible variations in recombination and tunneling rates have been proposed as causes for the observed peak splitting. [74-76] By using current-sensitive pre-amplifiers and no shaping, we obtain pulse heights that are relatively insensitive to such variations. This can actually be a disadvantage, since the nearly-coincident spectral peaks produce broadened, single peaks when combined. A mechanism for dealing with this situation will be presented later in this chapter.

Ideally, quasiparticle production is instantaneous on the time scale of a single pulse, and the amplifier can track the resulting current perfectly. The pulse height is then determined solely by the initial quasiparticle density, and any variations in the relaxation parameters appears as changes in the decay shape. Unfortunately, the finite bandwidth of the amplifier requires that some of those changes in shape appear in the measured pulse height. The effects of asymmetric properties for devices operated with charge-sensitive amplifiers have been studied in the aforementioned references. The implications for detectors operated with current-sensitive amplifiers will now be discussed.

First, the ideal output current is calculated for a linearized system composed of two quasiparticle reservoirs (traps or electrodes) with dissimilar quasiparticle tunneling

and loss rates. The initial condition with n_0Ad quasiparticles in a single reservoir of volume Ad is considered. In the equations given below, n is the athermal quasiparticle density, γ_T is the tunneling rate, γ_L is the loss rate, subscript numbers identify the reservoir, and superscript numbers indicate which reservoir is initially filled. The eigenvalues λ_f and λ_s are the fast and slow decay rates, respectively. Solutions corresponding to one initial condition can be obtained from solutions to the other initial condition by exchanging indices on n and γ parameters, and applying identities provided by the characteristic equation of the system and its eigenvalues. These identities allow the solutions to be written in several equivalent forms. A fairly symmetric set of solutions is given below.

$$\dot{\vec{n}}(t)=\begin{bmatrix}-(\gamma_{L_1}+\gamma_{T_1}) & \gamma_{T_2}\\ \gamma_{T_1} & -(\gamma_{L_2}+\gamma_{T_2})\end{bmatrix}\vec{n}(t),\vec{n}(t)=\begin{bmatrix}n_1(t)\\ n_2(t)\end{bmatrix} \tag{5.1}$$

$$\lambda_{f,s}=-\frac{1}{2}\left[\sum_{\text{all }\gamma}\gamma\pm\sqrt{\left(\sum_{\text{all }\gamma}\gamma\right)^2-4\left[(\gamma_{L_1}+\gamma_{T_1})(\gamma_{L_2}+\gamma_{T_2})-\gamma_{T_1}\gamma_{T_2}\right]}\right] \tag{5.2}$$

$$\lambda_f<\lambda_s<0,|\lambda_s|<|\lambda_f|$$

$$\vec{n}^{(1)}(t)=\frac{n_0}{\lambda_s-\lambda_f}\begin{bmatrix}\gamma_{L_2}+\gamma_{T_2}+\lambda_s & -(\gamma_{L_2}+\gamma_{T_2}+\lambda_f)\\ \gamma_{T_1} & -\gamma_{T_1}\end{bmatrix}\begin{bmatrix}e^{\lambda_s t}\\ e^{\lambda_f t}\end{bmatrix}$$
$$\vec{n}^{(2)}(t)=\frac{n_0}{\lambda_s-\lambda_f}\begin{bmatrix}\gamma_{T_2} & -\gamma_{T_2}\\ \gamma_{L_1}+\gamma_{T_1}+\lambda_s & -(\gamma_{L_1}+\gamma_{T_1}+\lambda_f)\end{bmatrix}\begin{bmatrix}e^{\lambda_s t}\\ e^{\lambda_f t}\end{bmatrix} \tag{5.3}$$

The quasiparticle current from each layer is taken to be proportional to the instantaneous quasiparticle density in the layer. The total measured charge follows directly from the total current.

$$I^{(1)}(t) = eAd\begin{bmatrix}\gamma_{T_1} & \gamma_{T_2}\end{bmatrix}\cdot\vec{n}^{(1)}(t) = \frac{eAdn_0\gamma_{T_1}}{\lambda_s - \lambda_f}\left[e^{\lambda_s t}\left(\gamma_{L_1} + 2\gamma_{T_1} + \lambda_s\right) - e^{\lambda_f t}\left(\gamma_{L_1} + 2\gamma_{T_1} + \lambda_f\right)\right]$$

$$Q^{(1)} = \int_0^\infty I^{(1)}(t)dt = \frac{en_0Ad\gamma_{T_1}\left(\gamma_{L_1} + 2\gamma_{T_2}\right)}{\lambda_s\lambda_f} \qquad 5.4$$

The spectral peak separation for charge-mode measurements is

$$Q^{(1)}/Q^{(2)} = \frac{\gamma_{T_1}\left(\gamma_{L_2} + 2\gamma_{T_2}\right)}{\gamma_{T_2}\left(\gamma_{L_1} + 2\gamma_{T_1}\right)}, \qquad 5.5$$

which is identical to previous derivations obtained by various means. [33, 74, 76]

In current-sensitive measurements, the pulse amplitude is determined by the maximum in the tunnel current, possibly after application of some pulse shaping electronics. While the maximum quasiparticle density occurs at $t = 0$, an examination of the solutions 5.3 reveals that the maximum current may come later. In addition, the finite bandwidth of the current amplifier and the pulse shaping electronics will cause the measured maximum amplitude to depend on the precise time dependence of the current in the vicinity of the maximum. This is the origin of the small but noticeable peak separation in current-sensitive measurements.

The current pulse may take three forms, which can be distinguished by calculating the time t_{max} at which a maximum in the current occurs, or equivalently, by calculating the initial derivative of the current at $t = 0$. The parameter x, defined below in equation 5.6, defines the pulse shape in three classes for which $x < 0$, $0 < x < 1$, and $x > 1$:

$$x^{(1)} = \left[\frac{\lambda_f\left(\gamma_{L_2} + 2\gamma_{T_1} + \lambda_f\right)}{\lambda_s\left(\gamma_{L_2} + 2\gamma_{T_1} + \lambda_s\right)}\right], \text{ and} \qquad 5.6$$

$$t_{max}^{(1)} = \frac{1}{\lambda_s - \lambda_f}\ln x^{(1)} \text{ if } x^{(1)} > 1, \text{ 0 otherwise.} \qquad 5.7$$

If $x > 1$, the tunnel current actually increases even though the total quasiparticle number is decreasing. An example is plotted in figure 5.1. When the tunnel rates are different ("slow" and "fast") but are sufficiently faster than the loss rates, the total current can increase as quasiparticles tunnel from the "slow" electrode and populate an initially empty "fast" electrode. The current decreases when the ratio of the two quasiparticle densities approach its equilibrium value. While peak separation is directly attributable to initial current at $t = 0$ and hence the tunneling rates alone, the unusual pulse shape is of interest and may affect such things as optimal filtering templates.

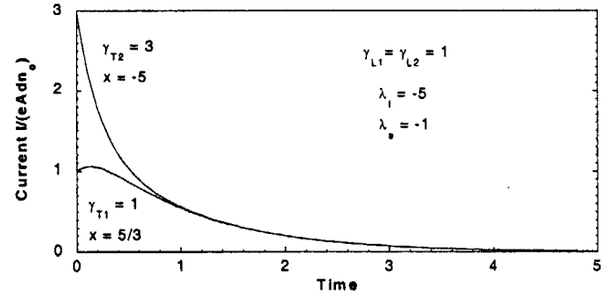

Figure 5.1: Examples of two pulse shapes where the initial quasiparticles are in the electrode with slow ($\gamma_{T1} = 1$) tunneling and fast ($\gamma_{T2} = 3$) tunneling rates. The spectral peak splitting in this case is due to the differences in the initial tunneling rate. The variation in pulse shape will affect analysis techniques that depend on pulse shape templates

In the intermediate class, $0 < x < 1$, the quasiparticle loss rate is sufficient to force a monotonically decreasing tunnel current. In this case, the initial decay rate is slow, then

increases after the population ratio equilibrates. The third class, $x < 0$, describes a pulse that has a fast initial decay, followed by a slower decay for the remainder of the pulse. These domains are more clearly illustrated in the following special cases: STJs with identical loss but different tunnel rates, and STJs with identical tunnel but different loss rates.

Case 1: $\gamma_{L1} = \gamma_{L2} = \gamma_L$

The expressions for the eigenvalues and the shape parameter x are greatly simplified in the case of identical loss rates but dissimilar tunneling rates. This situation is easily created and controlled by simply having different trapping volumes from which the quasiparticles must tunnel from. The proximity effect can also create this situation in a much less controllable, and possibly unintentional, fashion. First, the effective volume of the trap is dependent upon the volume of proximitized superconductor and how quickly the energy gap changes at the S-S′ interface. Second, the superconducting density of states is heavily modified by the proximity effect and can vary over the length scale where quasiparticles have a significant probability of tunneling into or out of the superconductor electrode. [44, 77] The following relations hold for dissimilar tunneling rates:

$$\lambda_f = -\left(\gamma_L + \gamma_{T_1} + \gamma_{T_2}\right)$$
$$\lambda_s = -\gamma_L$$
$$x^{(1)} = \frac{\left(\gamma_{T_2} - \gamma_{T_1}\right)\left(\gamma_L + \gamma_{T_1} + \gamma_{T_2}\right)}{2\gamma_{T_1}\gamma_L} \qquad 5.8$$
$$x^{(2)} = -\frac{\gamma_{T_2}}{\gamma_{T_1}} x^{(1)}$$

Two features are notable besides the simplicity. First, the pulse decay mirrors the quasiparticle decay after the population ratio between the two electrodes has equilibrated. At that point, the fast λ_f component of the pulse has decayed away, leaving only the slow λ_s component which matches the decay of the quasiparticle population. Second, pulses corresponding to one of the initial conditions will have an initial rise or initial slow decay (positive x), while pulses originating in the opposing electrode will have an initial fast decay (negative x).

Case 2: $\gamma_{T1} = \gamma_{T2} = \gamma_T$

This case corresponds to an otherwise symmetric junction that has unequal quasiparticle lifetimes in the two electrodes, which results in two-exponential decays. Any situation that results in unusually high quasiparticle loss could produce these pulse shapes. These conditions may be intentional, e.g. tunnel-once designs where quasiparticles are removed from one of the electrodes as quickly as possible. Or, the unintentional quasiparticle loss could be the result of edge recombination, metallic niobium oxides, magnetic impurities and magnetic flux penetration, or any number of other factors. The greatest difficulty in observing shape changes due to dissimilar loss rates is that the fast loss dominates the system, and changes in the initial decay must be observed on even shorter time scales.

The shape parameter for this case is given below. This case does not simplify as does the previous case. However, the shape parameter x is less than one for all values of loss and tunnel rates. An initial rise cannot occur if the tunnel rates are equal, which is consistent with expectations.

$$x^{(1)} = \frac{\gamma_{L_1}^2 - \gamma_{L_1}\gamma_{L_2} - 2\gamma_{L_2}\gamma_T + \gamma_{L_1}\sqrt{\left(\gamma_{L_1} - \gamma_{L_2}\right)^2 + 4\gamma_T^2}}{\gamma_{L_1}^2 - \gamma_{L_1}\gamma_{L_2} - 2\gamma_{L_2}\gamma_T - \gamma_{L_1}\sqrt{\left(\gamma_{L_1} - \gamma_{L_2}\right)^2 + 4\gamma_T^2}} < 1 \quad \forall \gamma \qquad 5.9$$

In summary, an asymmetry in the detector response can result even if the absorbers perform identically, resulting in two, possibly overlapping, spectral peaks for each x-ray line. This effect may be small for junctions with high symmetry, but it degrades the overall performance of the detector since the overlapping peaks form a single peak that is unnecessarily broad. The asymmetry can also result in multiple pulse shapes from each device. This reduces the effectiveness of analysis techniques such as optimal filtering, but also allows layer discrimination based on rise and decay time measurements as described in section 5.1. These effects are hard to observe directly in the LLNL symmetric junctions, but should be very obvious in devices with intentional asymmetry, such has tunnel-once designs.

Self-Recombination

The primary decay mechanism of quasiparticle excitations in a superconductor is recombination; two quasiparticles combine to form a bound Cooper pair. The decay rate is therefore not simply proportional to the quasiparticle density. This results in non-exponential impulse response and non-linear charge production in the STJ x-ray detector. This section describes empirical parameters that characterize the pulse shape. It is found that while the empirical parameters only provide limited information about the microscopic behavior of the junction, they are essential for producing high-quality spectra.

There is always a thermal population of quasiparticles that are recombining and regenerating. We will estimate the recombination rate of athermal quasiparticles from this thermal recombination rate. The general expression for the decay of this athermal quasiparticle population is given by

$$\frac{dn}{dt} = -2Rn_{th}(T)n - Rn^2 = -2\tau_r^{-1}(T)n - Rn^2 . \qquad 5.10$$

In this expression n is the athermal quasiparticle density, $n_{th}(T)$ is the thermal quasiparticle density, R is called the self-recombination coefficient and is determined by material constants, and $\tau_r(T)$ is the temperature dependent quasiparticle lifetime. The quadratic terms and the factor of 2 arise from the fact that a quasiparticle must recombine with another quasiparticle to be lost.

In this model of the detector output signal, we assume that all radiation-induced quasiparticles have been trapped in the aluminum trapping layers and have relaxed in energy until they are close to the proximitized gap. We assume that this occurs on a time scale much shorter than the tunneling time. This situation is similar to the analysis of Kaplan *et al.* [13] for thermal quasiparticles, although at athermal densities.

In the low-density limit near equilibrium modeled by Kaplan, the total quasiparticle density is approximately constant and much less than the thermal quasiparticle density. The recombination rate calculated by Kaplan in this case is given by

$$\tau_r^{-1}(T) = \frac{4\pi\Delta b(2\Delta)^2}{\hbar Z_1(0)}\left(\frac{\pi kT}{2\Delta}\right)^{1/2} e^{(-\Delta/kT)} . \qquad 5.11$$

In using this value for the loss rate, we have limited ourselves to the spatially homogenous case and are ignoring other loss processes such as normal or depressed gap regions near the edges and surface. The symbols b and $Z_1(0)$ are material parameters discussed in chapter 3. Identifying the thermal quasiparticle density as

$$n_{th} = 4N(0)\Delta\left(\frac{\pi kT}{2\Delta}\right)^{1/2} e^{(-\Delta/kT)}, \qquad 5.12$$

an estimate for the recombination coefficient for gap-edge quasiparticles is obtained:

$$R = \frac{4\pi b\Delta^2}{\hbar Z_1(0)N(0)} = -\frac{2\tau_0^{*-1}}{\Delta N(0)} = -2\Lambda\Delta^2. \qquad 5.13$$

In this expression, τ_0^{*-1} is the gap-scaled characteristic electron-phonon scattering rate used throughout this thesis and $N(0)$ is the single-spin electron density of states of the normal metal at the Fermi surface. The self-recombination coefficient R has been factored as $2\Lambda\Delta^2$ to emphasize the dependence on the value of the (possibly proximitized) energy gap. A value of 1.39×10^{-9} cm^3 s^{-1} meV^{-2} is calculated for 2Λ in aluminum. The gap is increased by the proximity effect to 0.36 meV, so the self-recombination coefficient $2\Lambda\Delta^2$ is estimated to be 1.60×10^{-10} cm^3 s^{-1}.

In most superconductors, the recombination phonon is immediately absorbed by a Cooper pair, replacing the two quasiparticles that recombined. This process is known as "phonon trapping." Thus, the *effective* quasiparticle lifetime is generally longer than the lifetime of a single quasiparticle state. Aluminum has unusually weak electron-phonon coupling to quasiparticles near the gap, and cannot trap phonons. Niobium has much stronger coupling, so the effective quasiparticle lifetime is 50 to 60 times longer in the unproximitized films. The proximitized niobium will absorb about 60% of the 2Δ phonons that escape from the aluminum, extending the quasiparticle lifetime in the trap by a factor of 2.5. Refer to the implementation of the multilayer cascade simulation in appendix A for the calculation of this factor.

We now lift the restriction that the detector is spatially homogeneous. In addition to recombination, there should be geometric losses that are proportional to the quasiparticle density. These losses would be associated with normal metal regions on the junction perimeter or within the normal metal cores of penetrating magnetic flux tubes. The generalized loss equation, allowing for phonon trapping and unspecified loss processes, and its non-trivial solutions for three cases are shown below.

$$\frac{dn}{dt} = -2\tau_{loss}^{-1} n - 2\Lambda\Delta^2 n^2 \qquad 5.14$$

$$n(t) = \begin{cases} n_0 e^{-2t/\tau_{loss}} & \Lambda = 0, \text{ geometric loss only} \\ \left[2\Lambda\Delta^2 t - n_0^{-1}\right]^{-1} & \tau_{loss}^{-1} = 0, \text{ self - recombination only} \\ \left[\left(n_0^{-1} + 2\Lambda\Delta^2\tau_{loss}\right)e^{2t/\tau_{loss}} - 2\Lambda\Delta^2\tau_{loss}\right]^{-1} & \text{self - recombination and geometric loss} \end{cases} \qquad 5.15$$

These solutions were applied as fitting templates to experimental pulse shapes. The pulses were produced by a device that had the best reported resolution for Mn Kα at the time, but also had several spectral artifacts. [78] An example spectrum is shown in figure 5.2. The sensor was a diamond shaped Nb-Al-AlO$_x$-Al-Nb junction with 200 nm aluminum traps. The detector also had an additional 900 nm layer of niobium deposited on the device to improve absorption efficiency. This layer was deposited after several processing steps and exposure to atmosphere, ending with ion-mill cleaning of the top niobium surface. The spectral artifacts were believed to originate in this additional niobium. The pre-amplifier feedback was in a fast, low-gain setting with a time constant of approximately 200 ns. Each detected pulse from the amplifier was digitized and fit without additional shaping or filtering. A low-pass gaussian-shaped filter was digitally

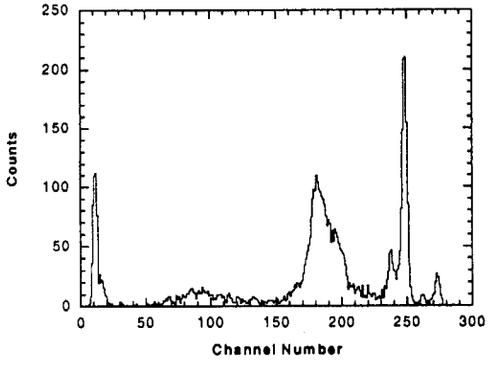

Figure 5.2: Spectrum from a device which produced a then-record 36 eV FWHM at 6 keV but suffered from severe artifacts. [78]

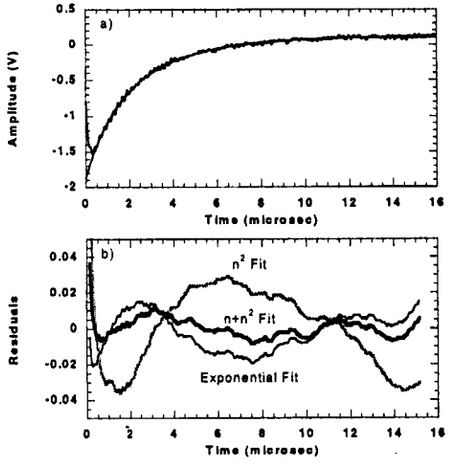

Figure 5.3: a) A smoothed x-ray pulse is shown with a fit using mixed-recombination model. b) Residuals of best fits from the three different models. The decay is primarily exponential, indicating that geometric losses are dominant.

applied to determine the time and amplitude of the pulse's peak and for plotting purposes. Pulse-shape fitting began at 90% of the filtered peak amplitude during the decay because earlier points were affected by the amplifier response. A DC offset and a time offset were additional free parameters in the fit. Pulse amplitude was estimated by subtracting the filtered peak amplitude from the average baseline amplitude before the peak rise.

Figure 5.3 shows a filtered pulse and shape fits for each of the three pulse-shape templates in equation set 5.15. The model based on self-recombination alone does not fit the pulse shape, indicating that geometric losses proportional to the quasiparticle density are present. A plot in amplitude-decay space for the exponential decay τ_{loss}^{-1} as determined by pulse shape fitting is shown in figure 5.4. The spectral peaks of figure 5.2 are identified as clusters. The same plots of geometric loss τ_{loss}^{-1} and self-recombination $\Lambda\Delta^2$ rates for the mixed-recombination model appear in figure 5.5. In this case, the dataset dramatically separates into two very distinct subsets.

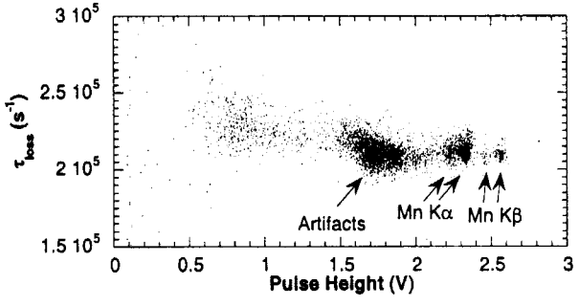

Figure 5.4: Estimates of the decay time of 5000 pulses from a least-squares fit to an exponential decay, plotted against the height of the filtered pulse.

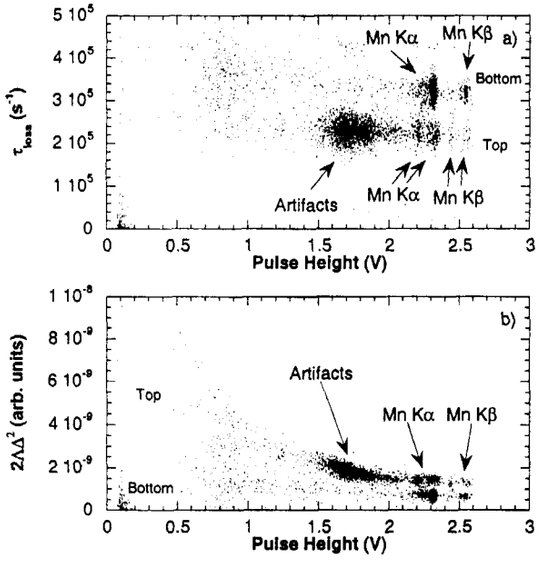

Figure 5.5: Scatter plots of the a) linear and b) non-linear recombination parameters from the mixed recombination model. The bands correspond to absorptions in the top and bottom niobium layers.

The values for self-recombination are in units of cm^3s^{-1}, but the scale is uncertain. Quantitative comparison of the fit parameter with theory requires complete characterization of the junction at the operating point and the amplifier gains. Unfortunately, these were no longer available at the time of analysis. The scale shown is an estimate, but uncertain within a factor of five.

These subsets are identified as absorption in counter (top) and base (bottom) niobium layers, as labeled in figure 5.5. This assignment is based on three observations: absorptions in the bottom film usually produce smaller pulses since more energy will

escape into the substrate; that the irregular group of pulses of medium amplitude were only observed in this device with additional niobium added to the top; and that this group contains the greatest number of counts. We believe that the unusual response of the top layer is due to the lesser quality of the film.

The bands of points from each layer represent an interesting trend. The shape parameters for the bottom layer are constant and consistent for almost all of the pulses in that layer. For the top layer, τ_{loss}^{-1} has a slightly negative slope, while $\Lambda\Delta^2$ is inversely proportional to the amplitude. The latter is characteristic of a decay that is the sum of two exponentials. This occurred only with the top-layer pulses but not with the similarly shaped bottom-layer pulses, so this can be considered a real effect and not an artifact of the fitting process.

Some additional features in the scatter plot can be identified. The pulses trailing to the left of the Mn Kα and Kβ x-ray lines are probably due to absorption events where quasiparticles have diffused from the niobium absorbers into the niobium leads, but nevertheless have shapes consistent with "full-yield" pulses originating in the same layer. The very small, very slow pulses in the lower left corner of figure 5.5 are substrate events, or absorptions of x-rays in the silicon substrate. Substrate events produce a prompt phonon signal which produces a small number of quasiparticles in the STJ detector, and long-lived excitonic states which continue to release energy over the duration of the pulse. The low-amplitude pulses with random decay parameters are accidental triggers due to noise.

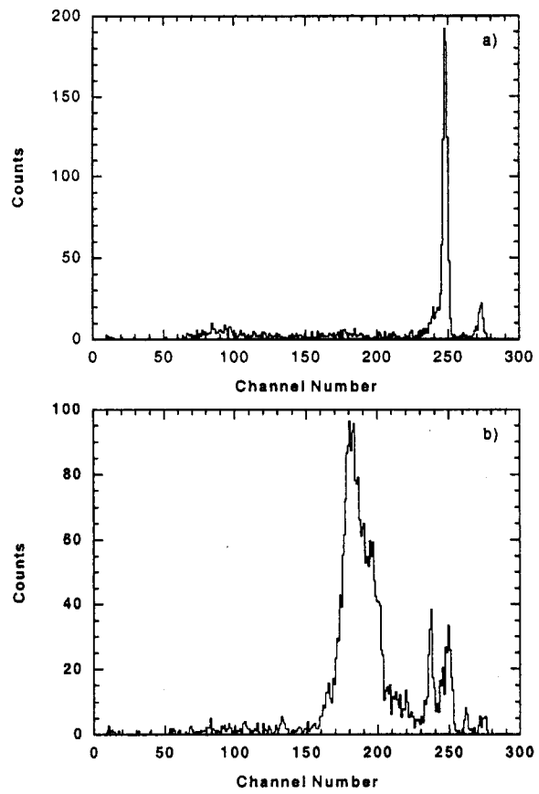

Figure 5.6: Separation of spectra from each layer. The spectra (a) and (b) contain only points from the top and bottom layers, respectively, as determined by decay time.

The obvious application of this analysis is to separate the subsets associated with each layer, which have slightly differing and overlapping responses, into separate spectra. These spectra can be examine separately, or calibrated and recombined. In the case of this device, the very clean and well-shaped spectra from the bottom layer can be separated from the confusing top layer. Figure 5.6 shows the original spectrum and the sub-spectra resulting from a cut of constant τ_{loss}^{-1} between the two datasets. The bottom-layer spectrum is almost completely free of top-layer peaks, with clearly resolved Mn Kα and Kβ lines. The Mn Kα FWHM is 70 eV. This device is actually capable of 36 eV when the measurement system was optimized for resolution rather than pulse shape analysis. [78]

5.2 Energy Dependence

For most x-ray spectroscopists, wavelength-dispersive spectrometers based on crystals or gratings are the instrument of choice. Wavelength dispersive crystal and grating spectrometers are capable of resolving powers exceeding 1000 and count rates exceeding 100,000 counts per second. However, simultaneous measurement of arbitrary energies can be difficult.

STJ detectors are inherently broad-band spectrometers, with potential applications ranging from optical to gamma-ray energies. [79, 80] Detector design would be optimized for a given energy range, e.g. optical, VUV and soft x-ray, hard x-ray and gamma ray. Once optimized, the detector can simultaneously analyze photons over the selected range. However, the resolving power and linearity must be established over the range. This subsection presents example spectra and analyzes the linearity and resolving power over nearly 2 decades in energy from 0.1 to 8 keV.

Origins of Non-linearity

The effects of self-recombination on the STJ signal were discussed in the previous sub-section. If enough athermal quasiparticles are confined in a small volume, such as the quasiparticle traps of the LLNL STJ detector, the loss rate due to self-recombination will dominate other losses through normal metal regions or recombination with other quasiparticles. This results in a non-exponential decay of the quasiparticle concentration with a sharp drop at early times, as illustrated in figure 5.7. A charge-sensitive integrating amplifier, which is standard in high-resolution spectroscopy, would see extremely non-linear response. [81] In contrast, an ideal current-sensitive amplifier would be able to measure the initial quasiparticle concentration which, in the absence of non-linear effects in the quasiparticle creation process, is directly proportional to the photon energy. In reality the finite bandwidth of the pre-amplifier and the use of shaping amplifiers makes some non-linearity inevitable. The linearity of an ideal current amplifier, non-ideal or shaping amplifier and charge-integrating amplifier are shown schematically in figure 5.8.

The self-recombination model of the previous section can be used to estimate the linearity of the STJ detector. The time-dependent current is given by expressions analogous to equations 5.14 and 5.15[a].

$$\frac{dI}{dt} = -bI - cI^2 \qquad 5.16$$

$$I(t) = \left[\left(\frac{c}{b} + I_0^{-1}\right)e^{bt} - \frac{c}{b}\right]^{-1} \qquad 5.17$$

[a] Equation 5.17 is, in fact, the fitting template for the parameters plotted in figure 5.5.

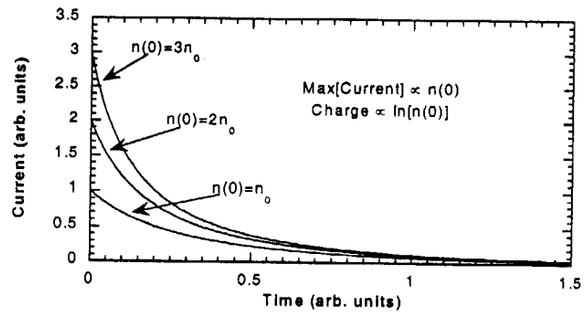

Figure 5.7: Self-recombination of athermal quasiparticles results in non-exponential decays of the output current. The fast initial decay causes the integrated charge to grow only logarithmically with the x-ray energy compared to the initial maximum current, which in turn is directly proportional to the energy and the initial quasiparticle density.

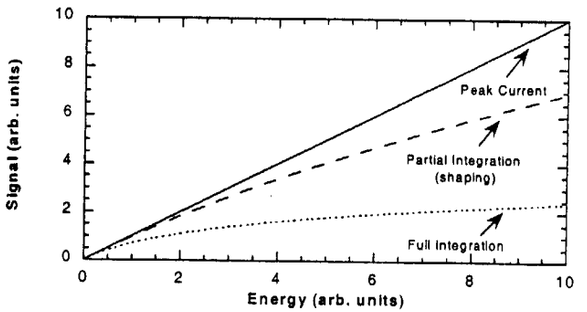

Figure 5.8: Measurement technique affects the linearity of the STJ detector response. An ideal current amplifier (solid) could accurately measure the peak current and would be perfectly linear, while an integrating amplifier (dotted) would see a logarithmic response. The current amplifiers at LLNL see an intermediate response (dashed).

The decay parameters have been written as I_0, b and c for clarity, and are defined as $I_0 = 2eAdn_0/\tau_{tunn}$, $b = 2/\tau_{loss}$ and $c = A\Delta^2\tau_{tunn}/e$. Both electrodes contain n_0Ad quasiparticles. The total charge is then

$$Q = \frac{1}{c}\ln\left(\frac{cI_0}{b} + 1\right). \qquad 5.18$$

It is useful to point out that when self-recombination has only a small effect on the quasiparticle decay, this can be expanded as a linear response with a small quadratic correction (of the correct sign):

$$Q = \frac{I_0}{b}\left(1 - \frac{cI_0}{2b}\right). \qquad 5.19$$

This is, of course, precisely the form one would use to fit a non-linear response. However, the charge fit parameters can now be related to the quasiparticle decay parameters. In addition, the logarithm model is not limited to c or I_0 being sufficiently small, as is required by a polynomial model, and can also be extrapolated more reliably than a polynomial.

Finally, consider the effect of finite amplifier bandwidth. As a very basic approximation, assume the amplifier returns some average current $<I>$ over a time t_{eff}. From equation 5.16, the peak average current near time $t = 0$ is

$$<I> = I_0\left(1 - \frac{b\tau_{eff}}{2}\right) - \frac{c\tau_{eff}I_0^2}{2}. \qquad 5.20$$

Thus, it is inevitable that a detector will exhibit some non-linearity if there is self-recombination of the athermal quasiparticles. However, the detector can be taken to be linear if any one of c, τ_{eff}, or I_0 is sufficiently small.

Figure 5.8 illustrates how the choice of measurement technique affects detector linearity. Integrating and current amplifiers are both very linear in the range 0.15-1.5 keV[8]. [81, 82] However, spectra at 6 keV typically have substantial non-linearity, and measurements in the optical and UV have uniformly reduced charge production. [83] A quadratic fit will not be adequate except over narrow energy ranges. With a current-sensitive amplifier, the detector will be fairly linear, and deviations from linear can be modeled with a quadratic over a wide range. It remains now to test the detector over a wide energy range, which follows.

Linearity Measurements

Two sets of data are presented here. The first set was measured with a "football" shaped junction with 200 nm-thick aluminum traps. In general, the larger trap is preferred for energies above 1 keV to minimize the effects of self-recombination. The radiation source was an electron impact source with various elements coating the anode, producing characteristic lines between 1 and 8 keV. The second set was measured with a "diamond" shaped junction with 50 nm-thick traps. The thinner traps are preferred for industrial analysis applications because the decay time is faster. This junction was tested with a synchrotron light source between 0.1 and 1 keV, our target range for analysis applications. Both sets were acquired with a PHA analyzer.

[8] The electrode volume in the quoted references is 50 μm × 50 μm × 250 μm.

Spectra from the 200 nm device are shown in figure 5.9. Since the x-rays are produced by direct electron excitation, a background of bremsstrahlung radiation is present in each spectrum. The carbon absorption edge in our IR filters can be seen at near 300 eV in this background. Also visible in the spectra is the peak splitting phenomena previously mentioned in this chapter. Since the absorption efficiency of the top niobium layer is less then 50% above 1 keV, each x-ray line except carbon Kα appears twice in each spectrum. Thus, each graph represents two independent spectra, which have been calibrated separately. The calibration and energy resolution given in the graphs correspond to the spectrum associated with the bottom layer, which has the better resolution. The exception, of course, is the carbon K line at 277 eV, which is completely absorbed in the top layer. With the aid of the carbon line, we were able to determine that the bottom layer produces larger pulses in addition to having better energy resolution. In addition to the lines shown, Mn Kα and Kβ at 5898 and 6490 and Cu Kα at 8037 eV were also measured. The absorption efficiency of the 160 nm and 240 nm-thick niobium films is very low at these energies; a total for both layers of 10% at 6 keV and 5% at 8 keV.

All identifiable Kα and Kβ lines were included in a weighted linear fit. The highest energy lines as well as most of the Kβ lines had only a small number of counts above the bremsstrahlung background and contributed the least to the fit. The fit and residuals are shown in figure 5.10. The bottom layer is very linear, while the top layer shows some deviation towards *larger* pulse heights. This effect has been studied by our group, [84, 85] but it has not been an easily repeatable feature.

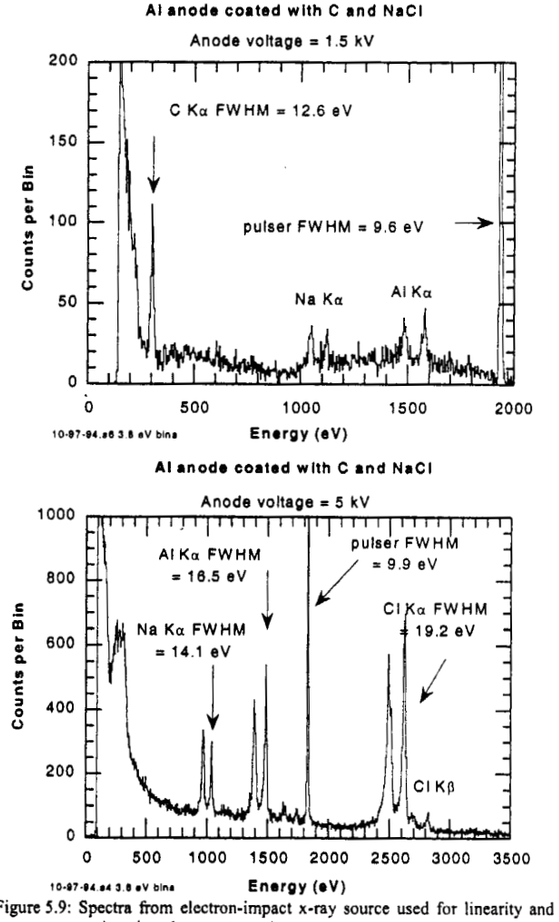

Figure 5.9: Spectra from electron-impact x-ray source used for linearity and resolution measurements (continued on next page).

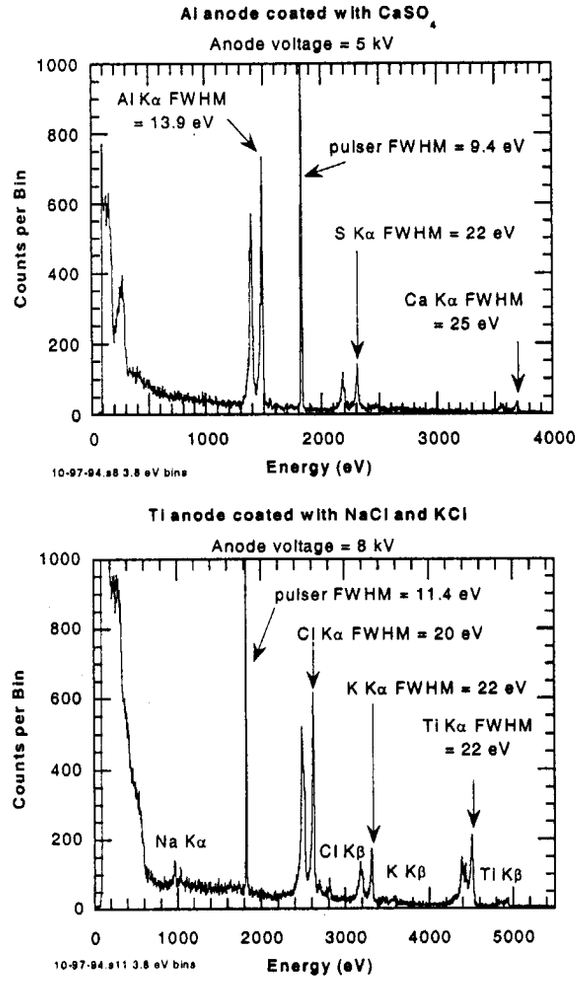

Figure 5.9: Spectra from electron-impact x-ray source used for linearity and resolution measurements (continued from previous page).

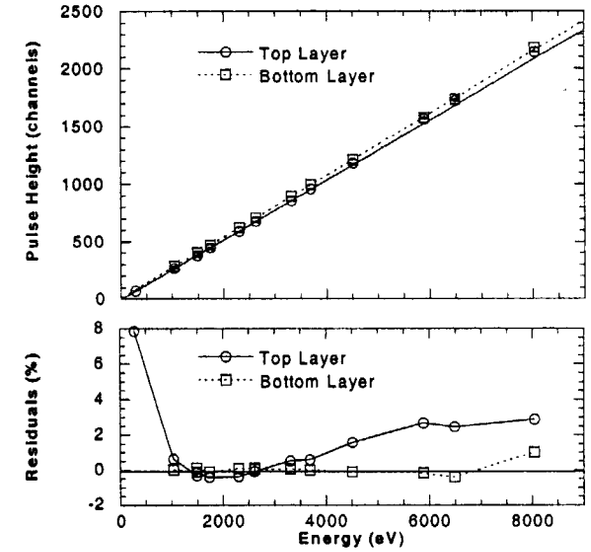

Figure 5.10: Weighted fit and residuals of fluorescent x-ray lines from an electron-impact source. The highest energy lines contributed the least to the fit. The bottom layer, which also exhibited the highest quality spectrum, is very linear. The top layer may be affected by pulse length anomalies that have been observed in the 200 nm-thick junction.

Figure 5.11 shows linearity results from the second set of data from a device with 50 nm-thick traps, which concentrates on the sub-1 keV energy range. Only the top layer is represented here. The detector response is extremely linear, although a small negative quadratic term would improve the extreme residuals. If included, this quadratic term would be a 1.25% correction to the signal amplitude per 1 keV.

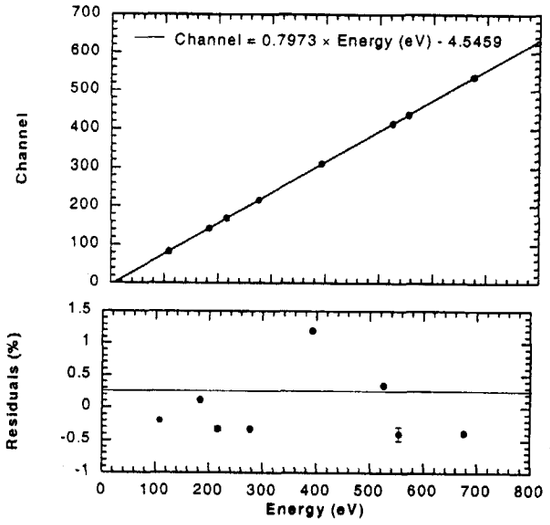

Figure 5.11: Linear fit of the response of a device with 50 nm-thick traps at low energies. Only absorptions in the top layer are considered.

5.3 Resolution

The resolving power of the detector as a function of energy is now considered. If quasiparticle cascade, trapping, and tunneling were purely Poissonian with loss-free diffusion, the spectral peak width of an x-ray line should increase with the square root of the x-ray energy. Unfortunately, this is not the case. In particular, spatial inhomogeneities can cause a certain fraction of the quasiparticles to be lost depending upon where the absorption occurred. When averaged over many absorptions, over the entire volume of the detector, this creates a noise source that grows in proportion with the

phonon energy. Possible mechanisms for such quasiparticle loss that have been previously mentioned are magnetic flux tubes, normal metallic niobium surface oxides, losses at the perimeter or losses out of the leads. However, variations in the film structure, such as impurities or grain boundaries, can create variations in the gap which can slow or trap quasiparticles within the absorber. [86]

The data sets analyzed earlier in this section for linearity will now be analyzed for peak width as a function of energy. All widths are the "intrinsic" detector width, having had the width of the electronic pulse generator subtracted in quadrature from the measured width. Note that the electronic pulse only estimates the contribution of electronic noise to the line width. During an x-ray induced pulse, the dynamic resistance of the STJ drops, thus increasing the real electronic noise contribution.

The first data set from a 200 nm-thick aluminum trap device and covering 1 to 8 keV in energy, is shown in figure 5.12. Spectral peaks attributed to top and bottom layers have been calibrated and analyzed separately. Each layer's width has been fit to a power law. This produced the interesting result that the top layer peak width varies almost linearly with energy, while the bottom layer widths vary nearly as a square root. We attribute this to layer quality. The bottom layer, although polycrystalline, is the first layer to be deposited and has the highest quality. The top layer is the fifth layer deposited and is noticeably rougher than the bottom layer when viewed with a scanning electron microscope. It may also have been affected by exposure to the atmosphere and was subjected to additional processing in order to connect the electrical lead. Other explanations, such as phonon loss through the substrate an effect due to the layer

thickness are unlikely to be the dominant effect, since these should result in a degraded *bottom* layer resolution.

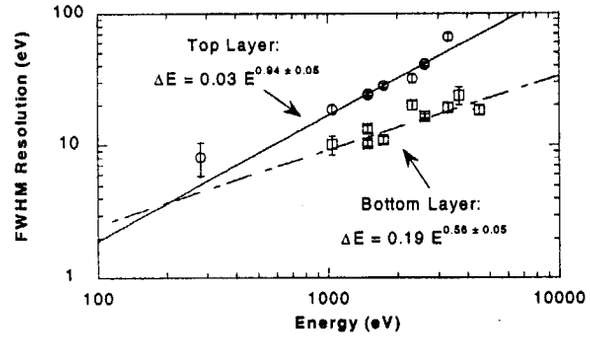

Figure 5.12: Spectral peak width of the x-ray lines in figure 5.9 from a device with 200 nm-thick traps. Peak associated with either the top or bottom niobium layer have been calibrated separately and fit to a power law energy dependence. The top layer exhibits a linear dependence that can be attributed to spatial inhomogeneities. The bottom layer exhibits a square-root dependence expected from a Poissonian counting process.

The resolution of the device with 50 nm-thick traps from the second data set is shown in figure 5.13. This data is of low-energy x rays which are usually absorbed exclusively in the top layer. The resolution appears linear with a zero intercept. An interesting effect unique to the stacked Nb-Al geometry is observable between 100 and 200 eV. This energy range is below niobium's M-absorption edge, where niobium becomes relatively transparent. As a result, nearly equal numbers of photons will be absorbed in the top niobium and top aluminum layers.

The relative Al:Nb absorption efficiencies for a 50 nm trap junction is plotted in figure 5.14. Between 80 and 200 eV, about equal numbers of photons will be absorbed in

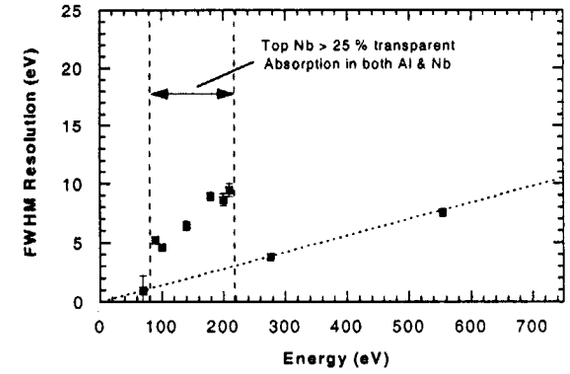

Figure 5.13: Net resolution as a function of energy for low energies. Most absorptions are in the top niobium layer and have a linear dependence. A substantial number of absorptions in the top aluminum layer in the niobium transparency window broaden x-ray lines in that region.

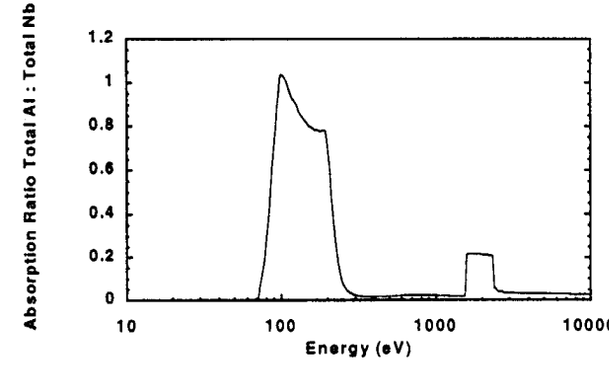

Figure 5.14: Ratio of aluminum to niobium absorption efficiency as a function of energy. The window of niobium transparency below 200 eV is below the niobium M-edge. A second window appears below the niobium L-edge at 2370 eV. Calculation is for a device with 50 nm-thick traps.

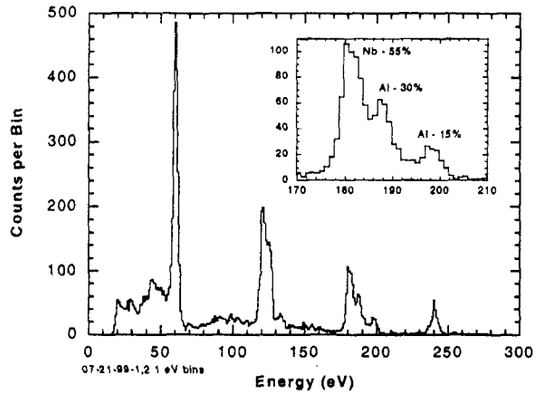

Figure 5.15: Spectrum of the 60 eV line from a grating monochromator, with 2nd, 3rd, and 4th order lines also visible at 120, 180, and 240 eV. The 120 and 180 eV lines are within the niobium transparency region and are split. The 60 and 240 eV lines are outside this region and are single lines. Inset: A close-up of the 180 "multiplet" is shown. Estimates of the peak areas from a fit to three guassian functions is also shown. These areas are consistent with the absorption efficiencies of these layers at 180 eV.

the niobium and aluminum layers. Absorptions in the aluminum generate pulses that are larger than pulses generated in the niobium and the resulting overlapped peak is much broader than expected. The observed splitting of a few percent is consistent with change in quasiparticle yield calculated in chapter 3 for differing initial layer of absorption. Unfortunately, this effect can limit the application of STJ detectors with this composition and design. For example, boron is an important dopant element in semiconductor manufacturing. The B Ka line is within this region where photons are absorbed directly in the aluminum layer and the resolution is degraded by line splitting. Development of tantalum absorbers will eliminate this problem.

A hi-resolution spectrum of the first four orders of a grating monochromator set to 60 eV is shown in figure 5.15, measured with a 70 × 70 μm^2 junction with 50 nm-thick traps. The first and fourth orders at 60 and 240 eV are outside the region of niobium transparency and are single lines. The second and third order lines at 120 and 180 eV are within this region and are split and, in the case of the 180 eV line, resolved.

This spectrum in figure 5.15 lends credence to the assumption of chapter 3 that quasiparticles are not strongly confined by a "hot-spot" effect. Consider the limiting case where the quasiparticles *are* completely confined until the cascade is completed. The aluminum gap is 0.70 meV, or half the niobium gap. Quasiparticles that are created in the niobium, have relaxed to less than 1.5 Δ_{Nb} while confined to the hot-spot, and then relax in the aluminum, will not break additional Cooper pairs in the aluminum. Thus, the number of quasiparticles resulting from an absorption in the niobium of a photon with energy E is $E/(1.7\ \Delta_{Nb})$. The number of quasiparticles resulting from an absorption in the aluminum, which is confined to the aluminum by the hot-spot, is $E/(1.7\ \Delta_{Al})$. *This is almost twice as large,* which is not what is observed. Instead, the created charge differs by only a few percent. The opposite limit, with no confinement, was treated in chapter 3. If quasiparticles and phonons are free to enter all layers at all energies, then nearly all dependence on the initial absorption layer is eliminated. The data can be explained by confinement of the highest energy quasiparticles, and some loss in the surface layer. [56]

5.4 Temperature and Magnetic Field Response

A variety of instruments may be classified as cryogenic microcalorimeters, including the STJ. The obvious commonality between these instruments is the extremely low temperature at which they operate. In general, the microcalorimeter does not distinguish

between the energy deposited by the x-ray and the thermal energy stored in the detector. The noise due to thermal fluctuations will be added to any response by the detector to an absorbed x-ray. Tunnel junctions, for example, measure the density of quasiparticles, which are produced continuously from thermal energy, in equilibrium with quasiparticle recombination. This production rate grows exponentially with temperature, and the thermal population could exceed the production due to x-rays. Also, the number of tunneling quasiparticles fluctuates so all quasiparticle current is inherently noisy. Thus, the temperature must be kept low to minimize the current due to thermally excited quasiparticles and its associated noise.

In addition to noise, the signal response of any microcalorimeter to an absorbed x-ray will depend in some way on temperature. In the case of the STJ, the current-voltage characteristic of the STJ detector will change with temperature because it directly depends on the thermal quasiparticle density. Thus, fluctuations in the temperature of the STJ can translate into fluctuations in the detector bias voltage (when biased with a constant current) and also in the detector gain (due to changes in the dynamic resistance). At sufficiently low temperatures the STJ detector is insensitive to thermal fluctuations, and can even be operated without temperature regulation. Only when the temperature rises to the point where the thermal tunneling current becomes comparable to the leakage current, and the current-voltage characteristic becomes temperature dependent, do we notice changes in the STJ response.

A general rule for STJ operation is that the average thermal energy must be less than one-tenth of the gap energy, so that the thermal quasiparticle density is negligible:

$$kT_{operate} < \Delta_{trap}/10. \qquad 5.21$$

For our devices with 50 nm aluminum traps, this corresponds to about 500 mK. This requirement is expressed in terms of the gap rather than the transition temperature because some materials may be proximitized.

Figure 5.16 is a typical plot of the current voltage characteristic of one of our devices at a temperature of 100 and 600 mK. Each point represents a stable operating point. Gaps that appear in the I-V plot are due to very high dynamic resistance regions (mostly near low voltage) or negative resistance regions due to Fiske resonances. In these regions the bias is unstable or very sensitive to electronic noise. The effect of increasing the temperature is to increase the thermal current at every voltage, decrease the bias voltage for a given bias current, and decrease the dynamic resistance everywhere. While it is easier to apply a stable current bias to a low, positive dynamic resistance, the signal-to-noise ratio decreases.

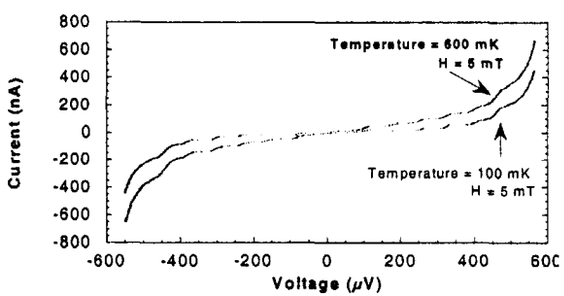

Figure 5.16: DC current-voltage characteristic of a diamond-shaped 100 μm × 100 μm tunnel junction with 50 nm traps operated at 100 and 600 mK. The energy gap is approximately 0.7 meV. The plot shows the increase in tunneling current at a given voltage due to thermal quasiparticles. This increase will grow exponentially with temperature until the junction becomes a 0.1 Ω resistor.

STJ detectors with 50 and 200 nm-thick aluminum traps were tested with x-rays from an electron-impact source. The anode of the x-ray source was coated with the

different target materials, e.g. NaCl, KCl, and graphite. The spectral resolution of the characteristic x-ray lines was measured for operating temperatures between 100 and 700 mK. Simulated pulses were injected into the detector to provide an estimate of the electronic noise. A typical spectrum is shown in figure 5.17.

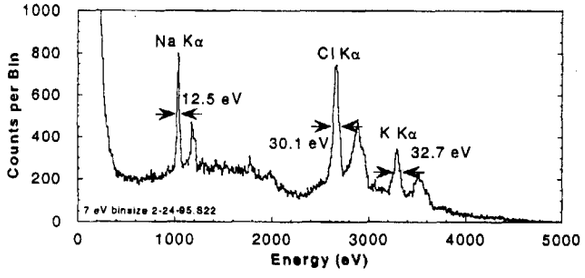

Figure 5.17: Example spectrum from the electron-impact x-ray source for the temperature stability study. Each x-ray line produces two peaks in the spectrum, corresponding to absorptions in the top and bottom niobium layers. The calibration and width for the indicate peaks are associated with the top layer. The background counts are from bremsstrahlung radiation produced by the electrons hitting the anode The detector was a 100 × 100 μm^2 football-shaped junction with 50 nm-thick traps. The temperature was 300 mK.

The width of sodium, aluminum, and chlorine Kα peaks as a function of temperature is plotted in figure 5.18. The bias current was adjusted between measurements to hold the bias voltage constant. A surprising result is the increase in resolving power (E/ΔE) with increasing temperature. Further deviating from expectations is the improved resolution at the lowest temperature with increased magnetic field. Conventional wisdom states that the applied magnetic field will create flux tubes, or regions of normal metal. It was expected that these flux tubes would increase the leakage current through the junction and decrease the dynamic resistances.

Also, the normal regions of the flux tubes can trap quasiparticles and cause them to recombine. As explained in chapter 2, a magnetic field must be applied to suppress the Josephson supercurrent through the junction. Thus, detectors are often operated at the lowest field that permitted a stable bias, usually the second or third minimum in the Josephson supercurrent. Instead we find that at the lowest temperatures a large, even excessive, magnetic field actually improved detector resolution. Three additional points in the figure 5.18 correspond to the sodium, aluminum, and chlorine peak widths at 100 mK and 20 mT. Compare this field with the critical field for bulk Al, which is 10 mT. The detector resolution is better under these conditions than almost all the other measurements at low field.

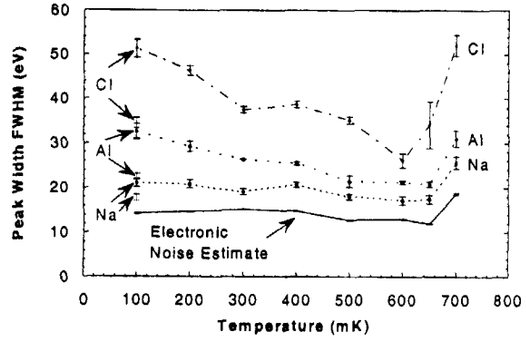

Figure 5.18: The temperature dependence of a 100 × 100 μm^2 STJ detector with 50 nm-thick traps. Thermal current dominates above 600 mK, indicating the maximum useful operating temperature for devices with 50 nm-thick traps. An additional point for each element at 100 mK represents improved performance at nearly 4 times the usual applied magnetic field.

Fiske resonances, as shown in figure 5.19, are the most likely cause of the resolution differences at high and low fields. During an absorption event the junction

approximately behaves as if it were at a much higher temperature. [24] The finite impedance of the current amplifier will result in a transient voltage drop, with an increase in current (the *load line*). It is conceivable that the voltage may jump to a Fiske resonance, then remain stuck for a moment, before continuing along the load line. This would alter the tunneling currents of the STJ since the quasiparticle DOS is voltage dependent. It could explain unusual decays that appear to be multiple exponentials. It could also alter the integrated charge, but should not affect the peak height. Also, the FET gate noise will be larger while the voltage is located on a Fiske resonance due to the

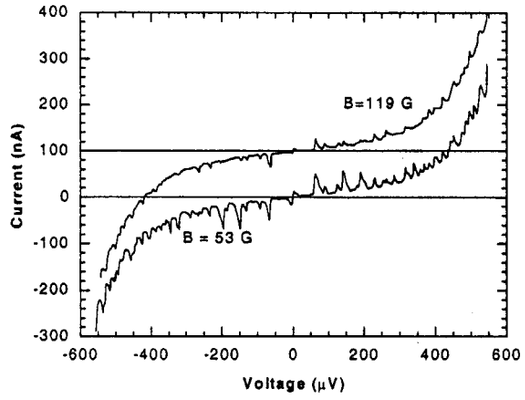

Figure 5.19: These are I-V curves of a 50 nm-thick trap, 200 × 200 μm^2 diamond junction measured with a voltage bias circuit and a chart recorder at a very slow speed (5 minutes per sweep). The I-V curve was measured with an applied magnetic field of 5.3 mT (53 G) (lower curve) and 11.9 mT (119 G) (upper curve). The high density of Fiske modes destabilizes the bias point, which is typically 400 μV for this device. The higher field helps suppress the Fiske modes and is a typical operating value at moderate temperatures. However, for best results we may apply a field up to 200 G (20 mT) at 100 mK and below.

reduced dynamic resistance. [87] A second, related, explanation is that the bias voltage is jumping to and from a nearby Fiske resonance at all times, adding high frequency noise to the baseline of the pulse. The high dynamic resistance at the lowest temperatures also makes the bias voltage susceptible to noise (either intrinsic or external RF pick-up) in the bias current, which may assist jumps to Fiske resonances.

STJs are very sensitive to magnetic fields. A sufficiently strong magnetic field suppresses the gap, the Josephson critical current, and the Fiske modes. In addition, the dynamic resistance at the bias point decreases due to flux tubes penetrating the junction. The 20 mT field is just below the point where the gap begins to be suppressed in devices with 50 nm-thick traps. It seems that at this point, one can improve bias stability by suppressing the supercurrent tunneling mechanism, but without decreasing the dynamic resistance, for a net improvement in the detector resolving power.

The junction is able to tolerate this field strength for several reasons. First, in thin-film superconductors, even type-I superconductors like aluminum, it is energetically favorable to allow the creation of discs of normal metal where magnetic flux is allowed to penetrate, instead of switching entirely to the normal state as is the behavior of bulk aluminum. Also, thin films are more tolerant of parallel fields than perpendicular fields. Second, the niobium, which has a much higher critical field, partially shields the aluminum. Third, the proximity effect has lent some of niobium's high critical field properties to the aluminum. The I-V curve at high and low field are compared at low temperature in the figure 5.20. For comparison, the I-V curve at high field and high temperature is also shown in figure 5.21. The leakage current has drastically increased as most of the junction is now an ohmic N-I-N junction.

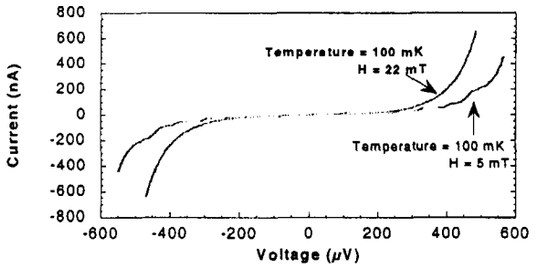

Figure 5.20: Another I-V curve of the same junction in figure 5.16, but at high field and low temperature. Almost all of the structure in the I-V curve has disappeared at high field. The gap has been reduced by about 100 μV, however, and the output signal is reduced because the dynamic resistance is less at the operating point. The best results were obtained at slightly lower field, such that the gap was not suppressed.

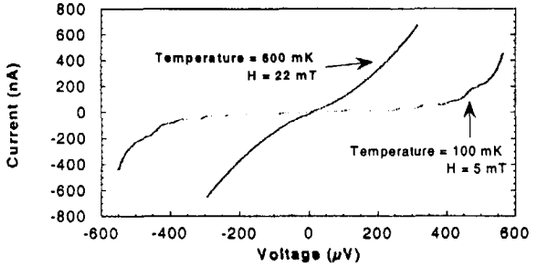

Figure 5.21: I-V curve of the same junction at high field and temperature. The temperature and the field have forced most of the junction area to be covered with normal regions.

As a result of this surprising improvement, 50 nm-thick aluminum trap junctions were subsequently operated around 8-12 mT at low temperature. Figure 5.22 shows that STJ detector response is nearly constant over a wide range of temperatures under this operating procedure. The 200 nm-thick trap devices were operated around 5 mT, because aluminum is proximitized much less in these devices

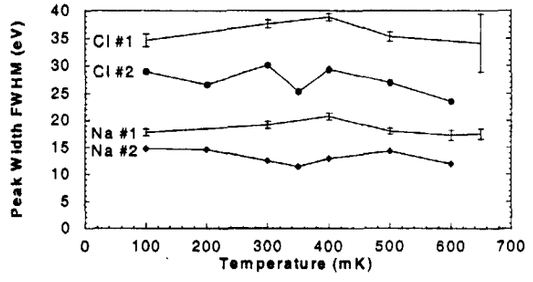

Figure 5.22: The temperature dependence of two different 50 nm-thick trap junctions. High magnetic field was applied below 300 mK. Although both junctions have the same normal resistance, junction #2 had a lower leakage current and higher dynamic resistance. Detector performance is now fairly constant over a wide temperature range through the application of additional magnetic field.

5.5 Count Rate

It is essential for a practical analysis instrument to handle very high count rates. This capability is necessary for measuring very dilute elements in a reasonable amount of time or to maximize the throughput in a semiconductor processing line. We have measured the performance of the STJ detector with FET readout with the assistance of a synchrotron radiation source at count rates exceeding 50,000 cps.

Superconductor-insulator-superconductor tunnel junctions have an intrinsic advantage over other cryogenic microcalorimeters in this respect. Most

microcalorimeters achieve superior resolving power by measuring the deposited energy in its entirety, over a relatively long time. Although clever read-out circuitry can reduce this time, [88, 89] it remains basically the amount of time required to cool to the original temperature before absorption and is determined by the heat capacity of the microcalorimeter. In contrast, SIS detectors are nearly completely insensitive to energies smaller than the gap energy. By measuring only the athermal electronic excitations, an SIS detector does not need to wait for the temperature to stabilize. Instead, its fundamental time scale is the lifetime of the quasiparticle excitation. This time scale is inversely related to the gap, which provides a mechanism for engineering the detector for high count rates. For example, our devices with 200 nm-thick aluminum traps have 5 μs decays, but devices with 50 nm-thick aluminum traps have 2 μs decays.

We tested a 50 nm-thick aluminum trap device at the synchrotron radiation facilities at SSRL. The junction size was 141 μm × 141 μm. We exposed the junction directly to the beamline monochromator which was tuned to the carbon K line at 277 eV. The count rate was controlled by adjusting aperture slits at the monochromator in the range of 5 – 10 microns. The pre-amplifier was configured with a 500 ns feedback circuit. The output of the pre-amplifier was shaped by a Canberra 2020 spectroscopy amplifier with baseline restore. The output of the spectroscopy amplifier was measured with a Tennelec PC-based Nucleus PHA card. The pile-up rejection capabilities of the spectroscopy amplifier were not implemented.

The detector performance as a function of count rate is exhibited in figure 5.23. We applied a shaping time of 3 μs at count rates below 3000 cps, which optimized detector resolution. We applied a shaping time of 1.5 μs at higher count rates to

accommodate the higher rate. The detector performance is nearly constant at low count rates, with spectral peak widths of 6 eV at the carbon K energy 277 eV. The resolution begins to degrade at higher rates due to imperfect baseline restore. At the highest rates, around 50,000 cps, resolution degrades rapidly as pile-up becomes a factor. Also, the PHA electronics experienced 50% dead time at this rate, so the input count rate was actually near 100,000 cps. This is the rate at which the junction must accommodate x-ray absorptions, or else suffer from bias instability and pile-up. However, the output count rate is quoted since that determines that rate useful data was acquired.

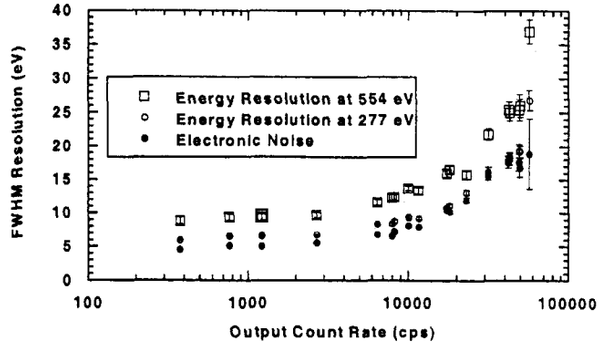

Figure 5.23: Detector resolution as a function of output count rate. Open symbols are represent monochromatic lines from the synchrotron, while solid circles are pulses injected into the amplifier during acquisition. The increase in spectral peak width with count rate is primarily due to fluctuations in the baseline. The intrinsic linewidth from the monochromator is negligible. The junction area was 141 μm × 141 μm and the trap thickness was 50 nm.

Example spectra at low (275 cps) and high (23,000 cps) count rates are shown in figure 5.24. These spectra contain monochromatic first and second order diffraction lines from the monochromator at 277 and 554 eV. The broad peak labeled "surface layer

events" are due to absorptions in the protective SiO_2 layer which was not been completely removed from this device. Each peak is 7 eV wider at 23,000 cps than at 275 cps. We attribute this to a long-lasting shifts in the baseline between pulses caused by the recharging of the 5 μF capacitor between the junction and the preamplifier. It should be noted that widths of 10-15 eV are more than adequate for semiconductor process monitoring for contamination and correct stoichiometric ratios.

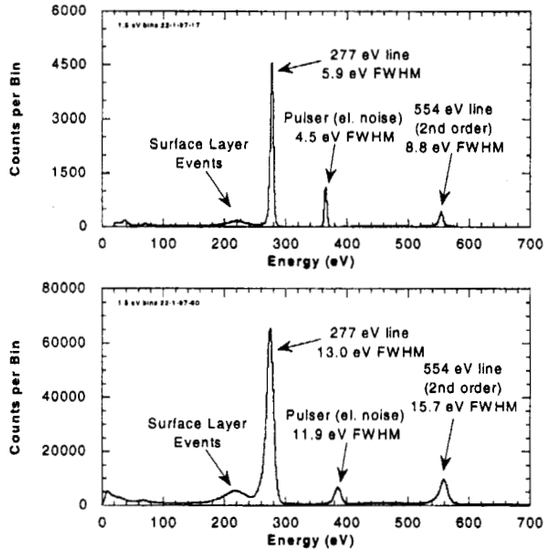

Figure 5.24: Changes in the spectrum due to count rate. The top spectrum was acquired at 275 cps, while the bottom spectrum was acquired at 23,000 cps. All peaks, including the injected pulser peak, have been broadened by about 7 eV, which is due to fluctuations in the baseline. The detector is the same one described in figure 5.23.

5.6 Conclusions

This chapter summarized the operation of the STJ as the detector in an x-ray spectrometer. Specifically, the operation of the STJ with a current-sensitive pre-amplifier has been described.

Of particular interest for understanding STJ physics was the investigation of possible variations in the pulse shape, as measured in the decay of the pulse. Two possible mechanisms for these variations were proposed, and were related to the observed pulse shape through the tunneling and recombination rates. The first mechanism is a simple asymmetry between the rate constants in one electrode relative to the rate constants in the other. This will result in a double-exponential decay in the junction current, which in turn will alter both the rise and the decay of the amplified pulse. The second mechanism is due to the self-recombination of the athermal quasiparticles. Since the probability of a quasiparticle recombining is proportional to the density of available quasiparticles, the quasiparticle population will decay non-exponentially. This non-exponential decay not only fit our measured pulses better than an exponential, but was also able to distinguish pulses caused by absorptions in different layers of the junction electrodes. With proper calibration, fits of the non-exponential decay can yield the average self-recombination and non-self-recombination loss rates.

Points of interest for the application of STJs for regular use in spectroscopy are linearity, temperature stability, and count rate. Quasiparticle self-recombination creates an inherent non-linearity in the STJ detector. The non-exponential decay results in a logarithmic dependence on the x-ray energy for the total tunneled charge. Current-sensitive detectors are much less sensitive to this effect, and we demonstrated our STJ

detectors are very linear over the individual ranges 0.1 – 1 keV and 1 – 8 keV with only a small quadratic correction. Again, it may be possible to relate the amount of non linearity to the average self-recombination loss rate.

Since the STJ is sensitive to athermal excitations, it is insensitive to changes in temperature as long as it remains below a certain temperature at which the thermal quasiparticle population becomes negligible. For devices with thinner (50 nm) aluminum traps, and hence greater energy gaps, we demonstrated very little change in the spectrometer resolution as the temperature was varied between 100 and 500 mK. Surprisingly, we found that a magnetic field actually improved the energy resolution and further reduced the small observed temperature dependence. This runs counter to the conventional wisdom that an applied magnetic field increases the quasiparticle loss rate and thus also the width of the x-ray peaks. The benefit appears to be in stabilizing the DC current bias by suppressing Fiske resonances.

Finally, we demonstrated the operation of the STJ spectrometer at high count rates using the high photon flux available on a synchrotron x-ray beamline. We were able to operate the spectrometer at rates up to 7 kcps with less than 10% increase in the peak width, using no pile-up rejection techniques. We further operated the detector to almost 30 kcps while only doubling the peak width, and 50 kcps while tripling the peak width. Even with this reduction in resolution, the STJ resolution still outperforms the best Ge detector by a nearly a factor of two. A factor of two improvement in detector resolution can be significant for many practical applications, as described in chapter 6.

Chapter 6

Application of STJ Spectrometer to Fluorescence Measurements

A major motivation for this thesis is the demonstration of the STJ spectrometer as a potentially revolutionary analysis instrument. STJ spectrometers have resolving powers greater than semiconductor detectors, and can achieve similar counting rates if the excitation is suitably intense. The areas of spectroscopy that would benefit most from the additional resolving power are x-ray fluorescence analysis (XFA) of industrial, and biological samples. Often these samples are very dilute, and require an intense light source such as a synchrotron radiation. Many of these applications are limited to the use of hard x rays by the use of semiconductor detectors, and would benefit from new techniques that use soft x rays if an adequate spectrometer was available. Currently, the only competing technology is the soft x-ray grating, which can be very inefficient.

Many applications can benefit from XFA with higher spectral resolution. An example is the special processing of modern materials in the computer and electronics industries. Microprocessors and magnetic storage media require depositions of thin alloy films with precise elemental compositions. X-ray fluorescence can determine the concentration of the elements in the sample. Measuring the elemental concentrations of only a surface layer, or as a function of depth in a multilayer, is very difficult with hard x-rays since they penetrate deeply into a sample. Soft x-rays are preferred, but the

conventional semiconductor spectrometer is not capable of resolving the x-ray lines of different elements in the soft x-rays.

Other applications need to detect very dilute elements. This includes environmental monitoring and contamination control in semiconductor processing. Very high energy resolution is required to separate weak fluorescence lines from the tails of strong fluorescence peaks of other elements. Again, it is desirable to use low-energy x-rays or electrons to excite contaminants. This allows the location of the contaminant to be determined with greater precision, and makes it easier to excite only the contaminant and not the surrounding material, e.g. the silicon substrate.

Pure research of physical chemistrys requires greater energy resolution than can be provided by any energy-dispersive detector. These applications use the very-high resolving power of a grating to study the x-ray absorption spectrum of atoms. The fraction of the incident beam that is absorbed by the sample is measured as the incident energy of the x-ray beam is slowly varied. The absorption spectrum is altered by the chemical environment of the atom being studied, e.g. though the chemical bonds to adjacent atoms. In general, these alterations will be a shift or splitting of the x-ray line. These effects are easier to detect in soft x-ray lines than in hard x-ray lines, since the electrons that directly participate in chemical bonding in transition metals primarily interact with the lower energy x-ray energy shells, e.g. L, M, or N shells.

It is very difficult to measure the absorption spectrum of a dilute element, since the transmitted beam is essentially unchanged. Instead, researchers perform fluorescence-detected x-ray spectroscopy (FDXRS). Each absorption of an x-ray may result in the emission of a *secondary fluorescence* x-ray. A photon-counter or energy-

dispersive spectrometer counts these secondary photons and the absorption spectrum is determined mathematically. All of the previously mentioned benefits of using a high-resolution STJ detector for measuring fluorescence from dilute samples apply.

An excellent example of this application is the study of photosystem II, or PSII. PSII is part of the oxygen-evolving complex in chlorophyll. It is a protein that contains four manganese atoms, with a concentration of only 100 ppm. Each atom may be in a different oxidation state. Each time PSII absorbs an optical photon of the right wavelength, the oxidation states of some or all of the manganese atoms change. After four photons have been absorbed, the enzyme dissociates two water atoms and returns to its initial state. The details of how this process works is not well understood.

We decided to adapt our cryostat to measure fluorescent samples at the Stanford Synchrotron Research Laboratory (SSRL) to demonstrate the utility of the STJ spectrometer for XRF applications. To this end, we modified our cryostat to allow samples to be inserted and removed while the cryostat was cold, and constructed a vacuum system that would be compatible with synchrotron beamline requirements. We measured an array of samples that we consider to be representative of applications that will benefit most from the capabilities of the STJ spectrometer. Examples from these experiments will be presented in this chapter. These experiments revealed issues that must be addressed in order to satisfy the most demanding applications. These issues will be discussed at the end of the chapter. In general, these problems arise from our use of a cryogenic chamber that was not designed for sample analysis, and should be correctable by using a cryostat designed for this purpose.

6.1 Sample Mounting

A sample manipulator mechanism was built to insert samples for x-ray fluorescence measurements. To maximize solid angle, the sample was positioned close to the detector. This required the sample to be cooled to 10 K or lower. For flexibility, a loadlock was constructed to allow samples to be inserted and removed without warming the cryostat.

It seemed that an acceptable loadlock could be easily constructed from available materials. In particular, it was decided that O-ring sealed components could be used since all existing flanges on the cryostat were also O-ring sealed. Unlike your average loadlock design, heat transfer via conduction or radiation was of equal, or even greater consideration than the vacuum seal. However, as will be discussed later, the vacuum quality is just as important when analyzed soft x-ray fluorescence. The resulting design in shown in figure 6.1.

Fluorescence samples were mounted or dried on a sample tip. This tip was a 4 mm diameter aluminum rod with a face that was cut at a 30° or 60° angle. The STJ junctions were positioned to the side, with room allowing for up to four chips (eight detectors) to be mounted. Incident x-rays, co-axial with the sample tip, excited the sample which fluoresced into 4π steradians, of which half were directed outwards from the sample. The samples were mounted as close as possible to maximize the solid angle intercepted by the detectors. However, it was critical that the sample tip, which was at 2 K, did not come into contact with any part of the detector mount or the crab support, which was at 0.1 K. Even an intermittent touch would at best cause the temperature to vary wildly, and at worst warm the detector to 2 K in a matter of moments.

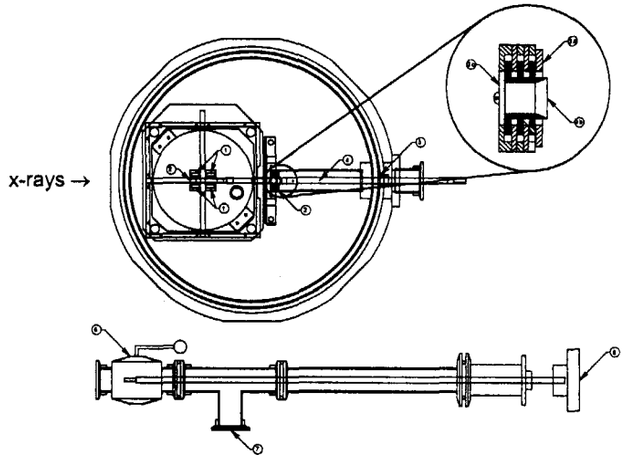

Figure 6.1: Loadlock and sample manipulator top view. ADR and cold plate have been omitted for clarity. Top left (left to right): Four detectors mounts (1) are positioned about the sample tip (2). The tip passes through a light-tight heat sink (3) and attached to a thin-wall stainless steel tube. The tip and tube are cooled as they are inserted by BeCu strips attached to the 77 K wall (4). A ball valve isolates the cryostat vacuum from the remainder of the loadlock. A Kwik-Flange tee (7) attaches the loadlock to a tribodyne vacuum pump. This tee also serves as the point of disconnection where the loadlock is dismantled. The sample tip and tube may be translated or rotated manually (8). Inset: Expanded view of the light-tight heat sink, indicating the fixed washer assembly (3a), the movable washer assembly (3b), and door (3c). Note that the manipulator arm is not tightly constrained by the heat sink.

The sample produces enormous quantities of Auger and photoelectrons compared to soft x-ray photons (ratio of 100:1). This requires an interposing filter between the sample and the detector, further complicating the positioning of the detector and sample. The edge of the sample tip, the filter, and the detector were each separated by 1 mm. This position was maintained by a guide positioned within the magnetic shield (not shown). The position of the rod was fixed at only two points: at the vacuum seal to the

room and at this guide near the detector. Because all of the guides are expected to move after being cooled, fixing the position at three or more points could result in a useless, non-co-linear arrangement.

The sample tip was screwed into a short rod of brass with external thread, which in turn was soldered to a long, thin-wall stainless-steel tube. A solid rod would conduct too much heat into the 2 K stage and cannot be used. The thin-wall tube, on the other hand, was susceptible to bending, and great care was needed when inserting it into the cryostat. Most of this tube was inserted through a larger, fixed copper tube that occupied half the length of the cryostat interior. The interior of the copper tube contained IR radiation from the 77 K shell and the room temperature loadlock, so it must be light-tight. The cold end of this tube was capped by a spring loaded door that could be pushed open by the sample tip.

The sample was guided to the door by a heat sink, shown in the upper right corner of figure 6.1. This heat sink consisted of two sets of washers interleaved with each other. One set of washers was fixed to the large copper tube. The other set was attached to a receptacle fixture that passed through the center holes of all of the washers. One end of the receptacle opened in a funnel shape to accept the sample tip and the other end had an internal thread. The sample rod was inserted into the receptacle and screwed into this thread. The thread and the interleaved washers conducted heat from the receptacle and prevented light from the warm parts of the loadlock from escaping into the 2 K workspace. In this way, the sample rod was cooled to 2 K at this point without constraining the position of the rod.

The sample rod was also heat-sunk at the 77 K wall by BeCu alloy "fingers", which contacted the rod with some springiness. The copper tube separated the 2 K and 77 K heat sinks by as much length as possible to reduce heat conduction into the LHe bath. The primary purpose of these fingers was to pre-cool the sample, and then to cool sections of the stainless steel tube as it was inserted in stages. This technique was not particularly effective, unfortunately. Both ADR and LHe hold times were much shorter when the sample rod remained inserted during the initial cooling of the cryostat.

The loadlock outside of the cryostat was constructed from standard Kwik-Flange vacuum parts, including a Kwik-Flange o-ring sealed, linear motion manipulator. A ball valve isolated the cryostat vacuum when the sample was removed from the system. A sufficiently long space between the ball valve and the manipulator feedthrough was allowed so that the stainless tube could be fully retracted into this space. Since the loadlock was constructed of Kwik-Flange vacuum parts, it could simply be disconnected at the ball valve when the sample needed to be changed.

Cryostat-Beamline Coupling

Most soft x-ray spectroscopy experiments at SSRL are constructed in UHV chambers that are directly connected to the synchrotron beamline. The useful lifetime of the electron beam is a prime consideration, and is limited by the collisions with gas molecules in the ring. The maximum allowable pressure at a user's radiation port is 5×10^{-9} Torr. Although the pressure in our cryostat is probably less than 10^{-8} Torr in the center, where gasses should be rapidly adsorbed onto the cold walls and into the charcoal, the pressure is much higher in the room-temperature sections. Our solution was to separate the HV of the cryostat from the UHV of the synchrotron with a window gate valve, manufactured

by VAT. [66] The window valve contained a 1200 Å polyimide film which is reasonably transparent to x rays.

The resulting configuration is shown in figure 6.2. The UHV section, located generally on the left, was maintained below 5×10^{-9} Torr by a Starcell 500 ion pump. The UHV section was isolated from the HV section by the VAT valve when the beam is in use, or by a standard gate valve when the beam is closed. The HV section was evacuated continuously through a flexible line to a turbo pump. The HV section also contained a linear manipulator arm. This arm could be used to insert phosphor in the beam for alignment purposes, or NiF_2 or gold foil for measurement of the beam intensity with a channeltron (not shown). A 0.005" and 0.001" thick aluminum foil were also on the arm to attenuate the zero-order or scattered light from the monochrometer.

Finally, the cryostat was attached to the HV section with another gate valve, a ceramic spool to provide electrical isolation, and a short bellows. The cryostat itself was mounted on a manipulator that allowed two degrees of rotational freedom (pitch and yaw) and one degree of translation perpendicular to the beamline. The height of the entire system could be adjusted with jack-screws. The center of rotation for both pitch and yaw was located at the intersection of the 77 K shield and the beam. The cryostat was positioned until the detector or sample tip were located in the beamline. Initial positioning was performed at room temperature with the cryostat cover replaced with 1.25" thick plexiglass plate. Final positioning was performed while the detector was operating and observing the count rate within an appropriate energy band.

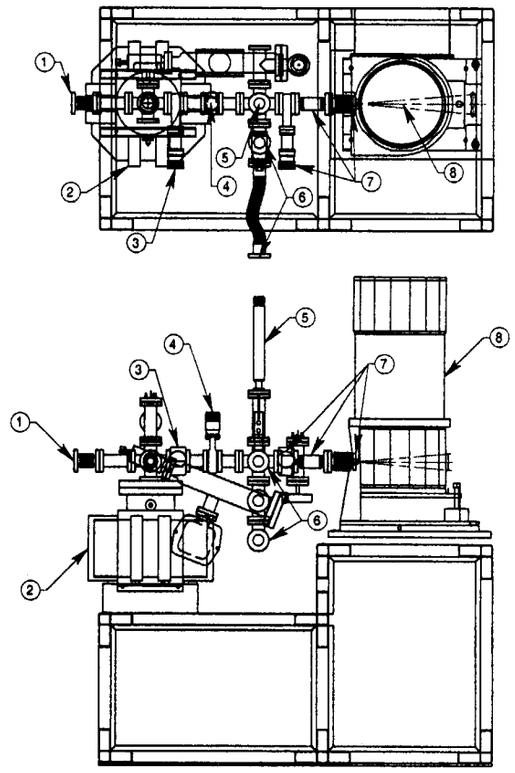

Figure 6.2: Vacuum and support structure for mating the cryostat to the SSRL beamline. The UHV section attaches to the SSRL beamline at (1). The UHV vacuum is maintained by an ion pump (2). The UHV and HV sections are separated by a windowless gate valve (3) or by a window valve (4) that contains a thin film. A manipulator arm (5) can lower foils, meshes, NiF_2 powder, or phosphor into the beam. An assembly of valves (6) allows the vacuum spaces to be evacuated or backfilled with N_2 gas. A gate valve, ceramic spool, and a short bellows (7) completes the connection between the beamline and the cryostat (8). The cryostat may be rotated in yaw and pitch about the beam entry point.

6.2 High-Resolution X-Ray Fluorescence Spectra Gallery

This section demonstrates the capability of the STJ spectrometers to detect transition and light elements through x-ray fluorescence. It focuses on fluorescence from industrial and biological samples in the soft x-ray energy region below 1 keV in. This is a difficult task, since the carbon, nitrogen, and oxygen K x rays from these samples can completely obscure x rays in the same energy region from elements with low concentrations. A selection of spectra are presented here that are the first demonstrations of an STJ spectrometer measuring fluorescent samples on a synchrotron. As an aid, table 6.1 lists important transitions from selected transition elements with energies in our region of interest. The transition orbitals and spectroscopy notation are also listed. Figure 6.3 illustrates the relationship between the energy levels of the first row of transition elements and their observed x-ray lines, as well as possible sensitivities to the chemical environment.

Level	Notation	Ti-22	Cr-24	Mn-25	Fe-26	Co-27	Ni-28	Cu-29
$1s_{1/2}$	K	4966.4	5989.2	6538.0	7111.2	7709.5	8331.6	8980.3
$2s_{1/2}$	L_I	563.7	694.6	769.0	846.1	925.6	1008.1	1096.0
$2p_{1/2}$	L_{II}	461.5	583.7	651.4	720.8	793.8	870.6	953
$2p_{3/2}$	L_{III}	455.5	574.5	640.3	707.4	779.0	853.6	933
$3s_{1/2}$	M_I	60.3	74.1	83.9	92.9	100.7	111.8	119.8
$1s_{1/2}$-$2p_{3/2}$	K α_1	4510.8	5414.7	5898.75	6403.84	6930.32	7478.15	8047.78
$1s_{1/2}$-$2p_{1/2}$	K α_2	4504.9	5405.5	5887.65	6390.84	6915.30	7460.89	8027.83
$1s_{1/2}$-$3p_{1/2}$ $1s_{1/2}$-$3p_{3/2}$	K $\beta_{1,3}$	4931.8	5946.7	6490.45	7057.98	7649.43	8264.66	8902.9
$2p_{1/2}$-$3s_{1/2}$	L ι	395.3	500.3	556.3	615.2	677.8	742.7	811.1
$2p_{3/2}$-$3s_{1/2}$	L η	401.3	510.2	567.5	628	694	762	832
$2p_{3/2}$-$3d_{3/2}$ $2p_{3/2}$-$3d_{5/2}$	L $\alpha_{1,2}$	452.3	572.8	637.4	705.0	776.2	851.5	929.7
$2p_{1/2}$-$3d_{3/2}$	L β_1	458.4	582.8	648.8	718.5	791.4	868.8	949.8

Table 6.1: List of major x-ray energy levels and transitions of selected transition elements, from the CRC Handbook of Chemistry and Physics, 71st ed. Values obtained from x-ray absorption are used when given. Note that transitions involving the 3p and 3d levels are very sensitive to the local atomic environment.

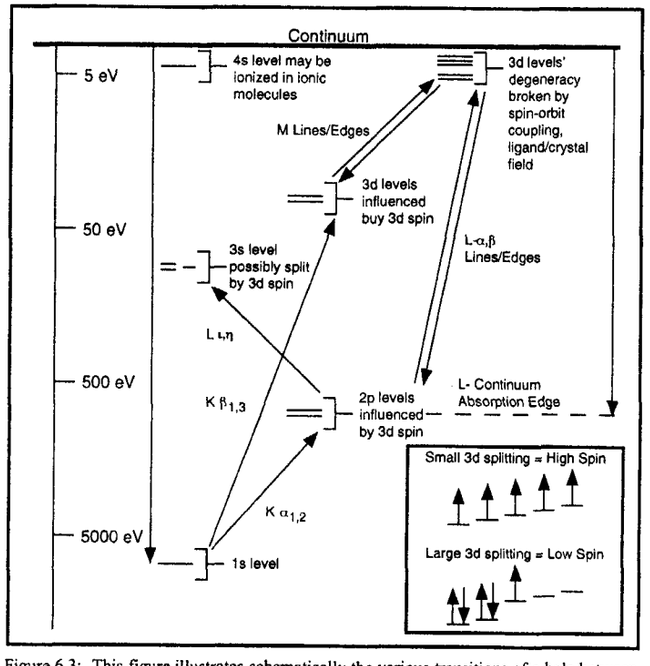

Figure 6.3: This figure illustrates schematically the various transitions of a hole between the levels of an early transition metal. An approximate energy scale is indicated on the left. The 4s and 3d electrons are the valence electrons, and are affected by adjacent atoms. These orbitals are either ionized or shifted in energy. Depending on the symmetry of the molecule or crystal, the 3d electrons may be shifted into two or more nearly degenerate bands. If the band separation is large enough, it will be energetically favorable for the electrons to form pairs. Otherwise, the electrons will attempt to have parallel spins. Inset: Illustration of the concept of high spin and low spin. The 3p and 2p orbitals, and to a lesser degree the 3s orbital, overlap the 3d orbitals and may feel the effect of several aligned spins. The resulting shifts in energy will be reflected in splitting and shifts in the K and L x rays. L x rays directly involve the valence states and are much more sensitive to the ligand/crystal field.

Ferredoxin

Ferredoxin is an important metalloprotein found in bacteria, plants, and animals. In humans it is found in the mitochondria and functions as an electron carrier during the production of steroid hormone. [90, 91] The active site in human ferredoxin is a cluster two iron and two sulfur atoms [2Fe-2S], a model of which is illustrated in figure 6.4. It is known that the cluster environment is maintained by ligand bonds to four cysteine molecules. Both irons are high-spin Fe(III) in the oxidized state. In the reduced state, one of the irons is Fe(II). However, it is not known which iron carries the electron, i.e. which cysteines bond to the reduced iron atom. X-ray absorption spectroscopy can provide a site specific probe of the iron bonds. A sample spectrum taken with a 200 × 200 μm junction is shown in figure 6.5. The resolution in this spectrum is 10.9 eV. This is sufficient to begin to resolve the 13 eV splitting of the iron 2p levels.

Figure 6.4: Models illustrating the structures of 2Fe-2S (left) and 4Fe-4S (right) active centers of ferredoxin. In the 2Fe-2S structure, the Fe atoms are bonded to each other and the two sulfurs of the complex, as well as to sulfur atoms belonging to cysteine amino acids in the surrounding enzyme. In the 4Fe-4S structure, the four Fe atoms bond to each other in a tetrahedron. The four S atoms bond to the three Fe atoms of each triangular face of the tetrahedron. Each Fe atom has one remaining bond to a S atom belonging to a cysteine molecule.

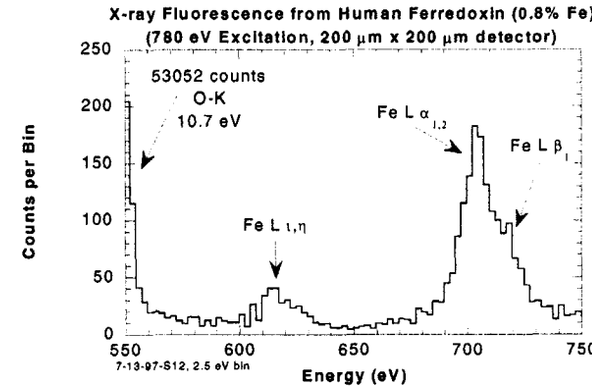

Figure 6.5: Fluorescence spectrum of ferredoxin. Acquisition time was 1500 seconds.

Hydrogenase

Hydrogenase is another essential metalloprotein found in almost all living organisms. Hydrogenase manages the dissociation of H_2 into protons and the reverse. This single task has many purposes, e.g. the temporary storage of energy, the creation of an ion gradient, or a proton supply to absorb electrons from other reactions. [92] It is one of the five known metalloprotein that has Ni at the active site. It also contains at least one Fe-S cluster. A model is shown in figure 6.6 and a sample spectrum is shown in figure 6.7. Both iron and nickel fluorescence are detected simultaneously with the single monochromatic excitation at 950 eV. Since the excitation energy is closer to the nickel L-to-continuum absorption edges (at 854 and 871 eV) than the corresponding iron edges (at 707 and 721 eV), the nickel fluorescence peaks are stronger than the iron fluorescence peaks despite there being a lower concentration of nickel. Some of the excitation beam

struck the copper detector mounts, resulting in the strong copper peaks in the spectrum. The sodium originates from the sample preparation solution.

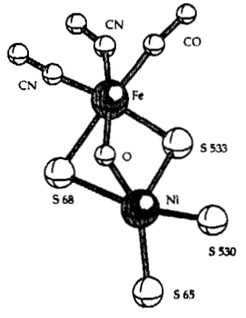

Figure 6.6: Proposed structure of the Fe-Ni complex of hydrogenase. [93] Numbers indicate positions along the protein chain.

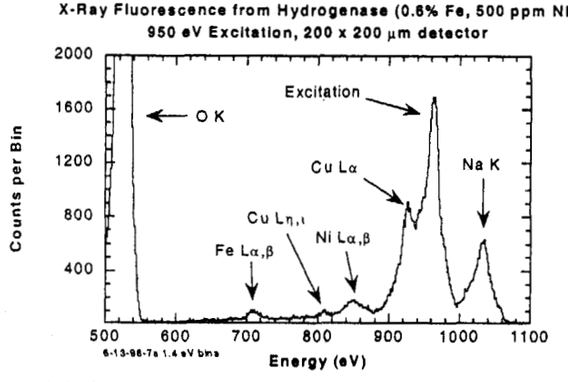

Figure 6.7: Hydrogenase spectrum. Acquisition time was 1.5 hours. Note that the excitation by 950 eV x-rays excites Fe and Ni unequally, so the peak heights will not correspond directly to the concentration. The oxygen peak contains 310,000 counts. The resolution was 12.9 eV FWHM.

IBM Disk

Researchers at IBM are interested in the fluorescence spectrum from a magnetic hard-drive storage disc measured with our detectors. This sample is interesting because it contains so many transition elements. The superior resolving power the STJ spectrometer has nearly resolved the $L\alpha_{1,2}$ and $L\beta_1$ lines of cobalt and nickel, making any fitting or deconvolution of the two lines a simple task. Also, many weaker lines such as the $L\iota,\eta$ and $L\beta_{3,4}$ are visible or are beginning to appear. Magnetic disk surfaces could be analyzed by TXRF (total-reflection XRF) for surface contamination, or GXRF (grazing-incidence XRF) for measuring film stoichiometry. Also, inelastic magnetic scattering in the magnetic materials could be studied. Note that the spectral peak heights do not correspond to the elemental concentrations since there is considerable re-absorption and re-excitation occurring. The IBM disk spectrum is shown in figure 6.8.

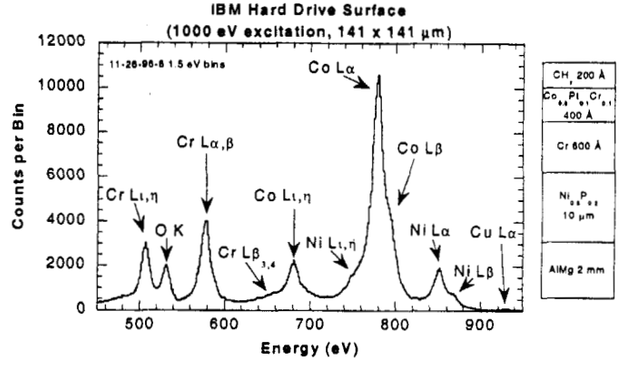

Figure 6.8: Surface of an IBM hard drive disc. The disc is an AlMg substrate coated with the following layers: 10 μm NiP, 60 μm Cr, 40 nm $Co_{80}Pt_{10}Cr_{10}$, and 20 nm of a polymer coating. Acquisition time was 500 seconds. Resolution was 12-15 eV.

Ti-N

Titanium-nitride is used as an insulating diffusion barrier for tungsten interconnects in aluminum-based VLSI technology. The stoichiometry must be very precise, or the TiN layer will either fail to insulate or fail to prevent diffusion of the tungsten into the silicon dioxide or other layers. Accurately measuring the Ti:N ratio with x-rays in a single measurement is nearly impossible given the proximity of the N K (392 eV) and Ti L (452 eV). Current techniques measure the Ti K (4510 eV) instead, but this requires separate spectrometers and possibly separate sources as well. Excitation of Ti K by high-energy electrons has worse spatial and depth resolution and excites a volume much greater than the structure being examined. If a spectrometer capable of discerning N K and Ti L was available, low-energy electrons could be used to excite only the Ti-N structure.

Two graphs are shown below with different size junctions. The capacitance, and hence the area, of our junctions determines the level of electronic noise output by our FET pre-amplifier. While a practical analysis instrument will likely try to maximize its collecting area, very demanding applications may require the best achievable energy resolution. The two spectra shown in figure 6.9 were measured with 141 × 141 μm and 70 × 70 μm junctions. The larger junction had an estimated electronic noise contribution of 5.2 eV, while the smaller junction had and estimated 4.1 eV electronic noise. Notice that the Ti L signal would be completely overwhelmed by the combined oxygen and nitrogen x-rays if a Ge detector were used, and deconvolution would be much too imprecise to return an accurate Ti:N ratio.

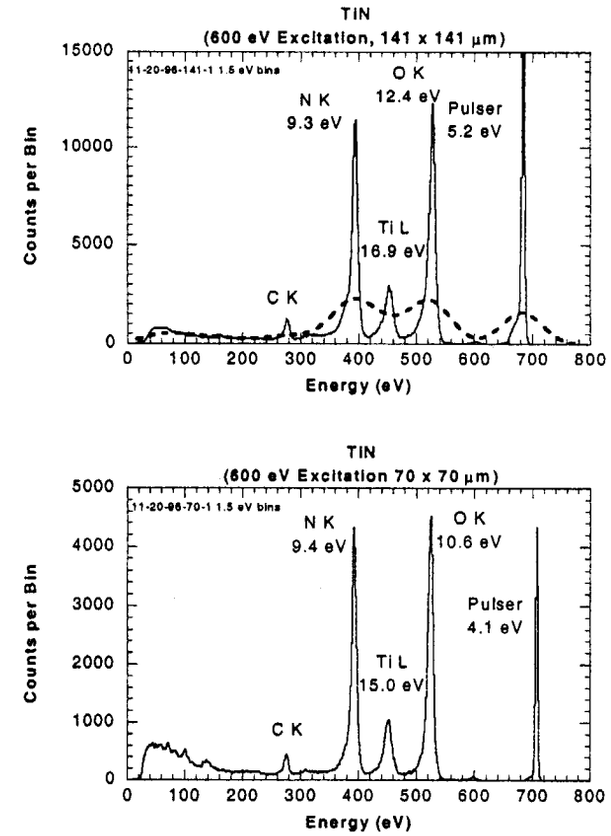

Figure 6.9: TiN measured 141x141 and 70x70 μm junctions. The Ti L signal would be completely overwhelmed by the N and O K lines if a 90 eV FWHM Ge detector was used (dashed). Note that Ti L an unresolved multiplet of several lines.

BN

Boron is an important dopant in semiconductor processing. As such, the concentration must be carefully controlled. Ordinarily XRF would not be considered for this task because the fluorescence efficiency of boron is extremely low. However, the combination of a bright source light the synchrotron and the tall, narrow spectral peaks produced by the STJ spectrometer make is a viable alternative.

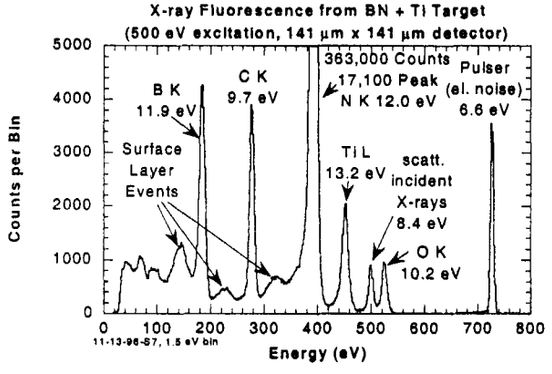

Figure 6.10: BN and Ti target. Artifacts labeled as surface layer events are absorptions in the protective silicon dioxide that covers each detector. Removal of this layer is still the least developed step of our process and is sometimes incomplete. The unusually broad B K line is the result of absorptions in both the niobium and aluminum layers, which occurs between 100 and 200 eV (see section 5.3).

6.3 Thompson (dipole) Scattering

The ability to acquire a high-resolution spectrum of fluorescent radiation is a powerful feature of the STJ detector. It allows rejection of counts from strong lines near the region of interest, and provides direct information about the fluorescing atoms. However, it is difficult to take advantage of this for the weakest, most dilute fluorescent targets. Figure 6.11 is a thirty-minute exposure of a PSII sample, which contains ~100 ppm of Mn ion. Besides the strong carbon and oxygen lines, there is also a peak of elastically scattered light from the sample. This scatter peak would completely swamp the Mn fluorescence if the excitation energy was not so far above the Mn L lines. Unfortunately, the most valuable information about the Mn ions is obtained by scanning the excitation energy through the L-line resonances rather than analyzing their fluorescence peaks.

Clearly, it would be best if this scatter peak could be reduced or eliminated. The beam from a synchrotron bending magnetic is almost completely polarized in the plane of the synchrotron ring. Reduction of the scatter peak could possibly be achieved if the detector and target are correctly aligned with respect to the beam polarization. It cannot, however, be eliminated. The detector is only 4 mm from the fluorescence target, so the target subtends a wide angle no matter how they are aligned. Some optimization should be possible despite this condition.

The first attempts to convert our cryostat into a fluorescence chamber used a highly slanted target and shown in figure 6.12a. This would cause the incident beam to be distributed over a large sample area at a shallow angle. The shallow angle would cause most of the absorption to occur near the surface, so that re-absorption of emitted

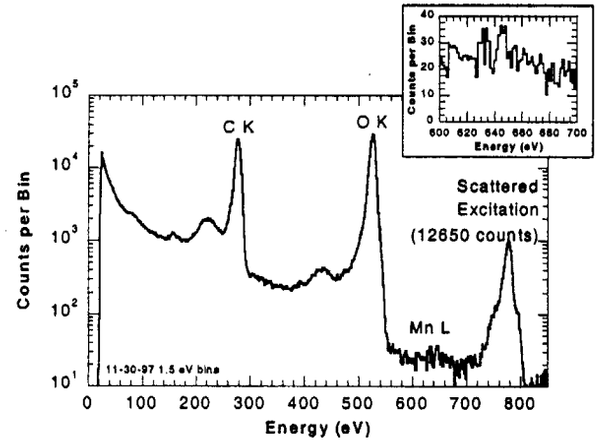

Figure 6.11: A thirty-minute exposure of PSII. The anticipated location of Mn Lα,β is indicated, although the apparent peaks there have marginal statistical significance. By generously allowing up to 40 counts in the Mn peaks and allowing for a fifty-fold increase in Mn L x-rays when excited on resonance, one can expect the peak of scattered incident light to still contain 6 times more counts. Note that the energy scale is a linear calibration between the carbon and oxygen lines, so the apparent manganese peaks are slightly shifted to lower energy.

photons would be lessened. Unfortunately, this also increased the solid angle subtended by the fluorescence target as seen by the detector, and the scattered signal was very strong. Subsequent measurements were made with the tips of figure 6.12b. These tips presented a face nearly perpendicular to the beam and only a (relatively) narrow ellipse to the detector.

A numerical integration program was written to calculate the geometric contribution to the amount of light scattered from the entire surface of the target, as well as the total fluorescence from the surface. The fluorescence intensity was determined by

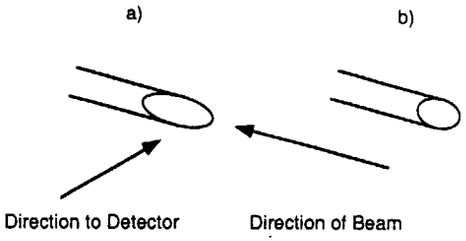

Figure 6.12: Two cuts of 4 mm diameter cylindrical sample tips used for fluorescence. Tip a) is a sharp, pointed cut with a surface normal of 60° with respect to the incident beam. Tip b) is a blunt, flat cut with a surface normal of 30° with respect to the incident beam.

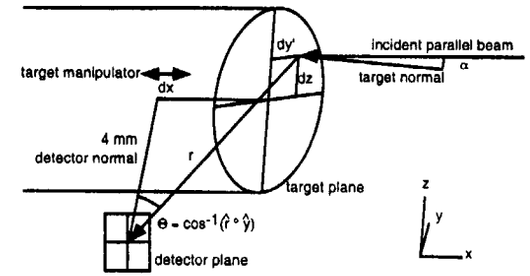

Figure 6.13: Geometry for the calculation of electric dipole scattering of the incident beam. The relative intensities of the fluorescent and scattered radiation are calculated for different target positions (dx) by integrating over the target face (dy' and dz). Two target face angles of 30° and 60° were compared. Note that the detector is taken to be a point.

a cosine term due to foreshortening of the detector and an r^2 term due to the highly variable distance between the different regions of the target and the detector. The scattered intensity also was determined by a dipole $\sin^2$ term. The dipole approximation is valid when the photon momentum is negligible and the wavelength is larger than the size of the oscillator, which is taken here to be the size of an atom. [94] This

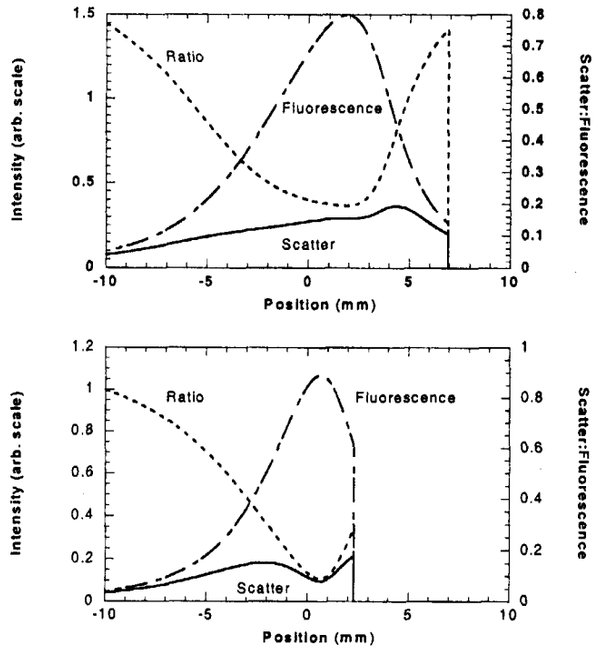

Figure 6.14: Predictions of the relative intensity of scattered and fluorescent light based on geometrical considerations. The top graph represents the broad tip cross-section "a", while the bottom graph represents the narrow cross-section tip "b". Both intensities are enhanced near zero where the detector is illuminated at normal incidence and the near-edge of the tip makes its closest approach. Scatter intensity is depressed near zero where the direction of emission is nearly coincident with the incident polarization vector. This depression is broad and weak because the tip is an extended source; however, tip "b" is sufficiently narrow to cause a minimum in the scatter intensity. All intensities drop to zero when the tip is pushed completely past the detector.

approximation should remain valid for photons with energies below 1 keV. The resulting position dependent intensity is integrated incoherently over the target surface, as shown in equation 6.1.

$$I_{scatter} \propto \cos\alpha \int_{target} \cos\theta(\bar{r})\sin^2\theta(\bar{r})\frac{dA}{r^2}$$
$$I_{fluorescence} \propto \cos\alpha \int_{target} \cos\theta(\bar{r})\frac{dA}{r^2} \qquad 6.1$$

Here, $\theta(r)$ is the angle made with the detector normal. which lies in the plane of polarization and r is the distance from the detector (a point) and a point on the target surface. Each integral should describe how the corresponding intensity should vary with the insertion position of the target tip and the ratio gives a measure of contrast between scattered and fluorescent light. The resulting curves are shown in figure 6.14.

Distance has the greatest effect on intensity. The graphs show that in all cases the maximum intensity is reached over a fairly narrow range of positions. The position was set by a 20 turns per inch thread. Since the target must face the detector, the position could be set to within 1.3 mm, which was adequate but not ideal. The edge of the target tip is just 2 mm from the detector at closest approach. Both scatter and fluorescence intensities increase near the zero position, but the scatter intensity drops when the near-edge is directly above the detector. The original design, tip "a", was much too broad, and there was substantial scatter from most of the target tip at any given position. The revised tip produces a narrow minimum in the scatter intensity, but the expected improvement in contrast is only a disappointing factor of two.

This model was tested at SSRL with tip "b" but we found that the scatter intensity was essentially constant over the range of useful positions. No measurable improvement in the ratio of fluorescence to scattering was noted, either. This could be attributed to several reasons:

1. the position setting was too course and the optimum position was missed,
2. the beam polarization may be rotated,
3. the exit path of a fluorescence x-ray travels through too much material when positioned at the predicted optimum position to show an increase,
4. the alignment of the cryostat ensures that x-rays pass through all windows and strike the target, but the target-detector vector may no longer be aligned with the polarization vector, or
5. the target is still too broad.

It may be possible to take the orientation of the polarization into account in future cryostat designs and alignment mechanisms. Alternatively, the beam could be collimated or focused to a small point, a technique that is already required for such tasks as quantitative analysis.

It appears that the scatter peak must be tolerated for the time being. Many experiments can be performed by exciting above the continuum edge; e.g. L-ι,η measurements require it. For FDXAS, the scatter peak shape can be measured with a long exposure and the subtracted from each spectrum. For FDXAS of the most dilute samples, such as PSII, the STJ detector can be operated as a single-channel analyzer in the same fashion as semiconductor detectors with an analysis window that covers the entire absorption spectrum. Unlike a germanium detector operated in this mode, a STJ

detector is still capable of rejecting the enormous oxygen background, reducing the Poissonian fluctuations in the window by a factor of 10.

6.4 Gas adsorption

Self-absorption of emitted x-ray photons by the sample matrix, by adsorbed gasses, and by the analyte species itself is a major obstacle to successful spectroscopy of soft x-ray emissions. This motivated the initial use of sample tips that positioned the target so that it was illuminated at a shallow angle, e.g. figure 6.12a, before being modified to minimize Thompson scattering. Even so, it has been very difficult for our system to measure dilute elements. We have observed a decline in fluorescence x-ray intensity over time in almost every measurement which cannot be accounted for by the slow decay of the incident beam intensity from the synchrotron. This decline is attributed to the continuous adsorption of gasses, particularly water vapor, on the target, filters, and detector.

It is an unfortunate fact that our cryostat was designed for cryogenic detector testing, not sample analysis in a UHV environment. The cryostat is seemingly entirely constructed out of materials that are antithetical to UHV vacuum technology: unbaked aluminum shells, layer upon layer of tightly wrapped superinsulation, brasses, lead-tin solders, epoxies, GE varnish, greased O-ring seals, and uncountable pieces of sticky polyester tape! The use of these materials is acceptable in a cryostat, since all surfaces except the outer-most aluminum shell are cooled to LN_2 or LHe temperatures. These surfaces, along with a piece of activated charcoal on the LHe stage, adsorb almost all of the residual gas in the cryostat when cooled. What remains is not effective at transporting heat and is ignored.

From the point-of-view of soft x-ray spectroscopy, this residual gas is an enormous headache. Evidence for this is available from an experiment that attempted to generate a rough absorption spectrum of MnO. A complete fluorescence spectrum was measured every 4 eV between 632 eV and 658 eV. Additional passes provided data at intermediate energies, as well as at the anticipated L resonance energies. The SSRL beamline used for this measurement, 10-1, does not have a sensor to allow simultaneous, or near simultaneous, measurement of the incident beam intensity after the final optical element. Therefore, the synchrotron beam current substituted for the incident beam intensity. Also, we intended to use the intensity of the oxygen line to correct for changes in the incident beam intensity.

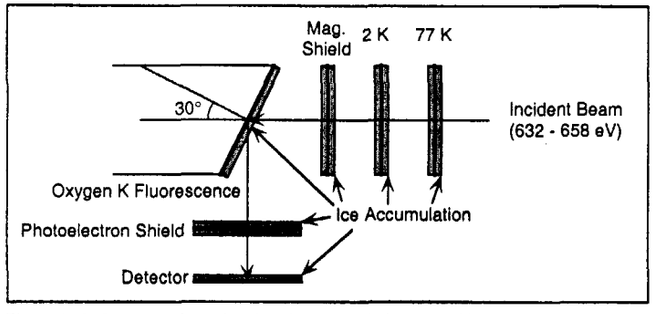

Figure 6.15: Geometry for estimating the accumulation rate of ice on cold surfaces, e.g. IR filters, the target sample, and the detector itself.

The time dependence of the total area of the O K line is shown in figure 6.16. The intensity of the oxygen line decreased by a factor of 5 in only 2.5 hours. This decay was fit by an exponential with a half-life of 77 minutes. The reduction in intensity at each time was compared to the expected attenuation resulting from identical water layers on the target, detector, and each filter. The oxygen fluorescence intensity, accounting for

changes in synchrotron electron current, the incident energy, which was varied during the experiment, and the geometric arrangement of the target and detector, is given below:

$$I(t) \propto I_0(t)\exp\left\{-\left[d(t)-d(0)\right]\left[\left(3+\csc(\theta)\right)/\alpha_{t-K}+\left(6+\sec(\theta)\right)/\alpha_{E(t)}\right]\right\}. \qquad 6.2$$

In this expression, $\alpha_{E(t)}$ is the attenuation length of oxygen at the energy $E(t)$, $\alpha_{O\text{-}K}$ is the attenuation length at the oxygen K line (525 eV), I_0 is the synchrotron electron current normalized to the first measurement, and $\theta = 30°$ is angle of the sample tip surface normal relative to the beam.

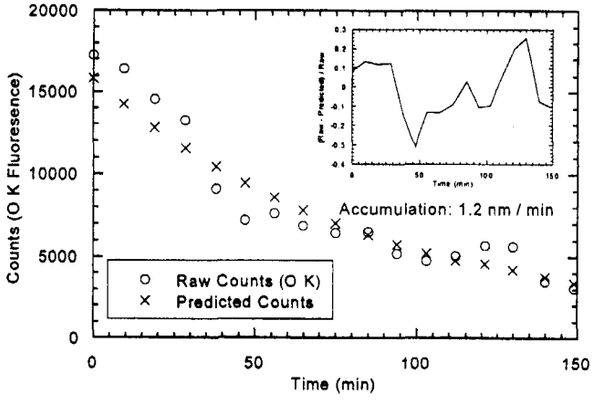

Figure 6.16: Circle symbols: the uncorrected intensity of the oxygen line during an FDXAS experiment. The incident energy was stepped over the range of 632 to 658 eV several times during the experiment. After correcting for changes in beam intensity and energy, an exponential decline in intensity remains. This decline is attributed to the accumulation of ice on all cold surfaces. Assuming identical layers of density = 0.9 g/cm^3, the accumulation rate is 1.2 nm/min or one monolayer every 15.5 seconds. Cross symbols: the projected observed counts. Inset: The residuals scaled to the measured counts.

An exponential fit to the attenuation caused by identical oxygen layers growing at a constant rate on all cold surfaces as a function of time is also plotted in figure 6.16. This attenuation corresponds to a layer growth of 1.2 nm of ice per minute. An important heuristic in vacuum technology states that each 1×10^{-6} Torr of partial pressure results in 0.5 monolayers of water per second of adsorption. [95] The modeled adsorption rate corresponds to an average partial pressure of 1.3×10^{-7}. This calculation was repeated for nitrogen, but it is very transparent at these energies and cannot account for the attenuation of the oxygen line at any reasonable accumulation rate. Thus, we conclude that the attenuation is due to water from the outer aluminum shell or from external leaks.

A factor that may contribute to leakage is the fact that our loadlock design was not very robust, and seemed to develop leaks after a few days of use due to wear of the O-rings. Thus, while both the cryostat and loadlock would pass helium leak checks, and detectors could be operated at the synchrotron in the direct-illumination configuration, the combined cryostat and loadlock in the fluorescence configuration would invariably begin to leak during an experiment. It was not noticeably leaking at the time of the measurement described above, however.

We have attempted to bake the outer shell of the cryostat to desorb water from its surface. Even if the cryostat is leak free, the poor vacuum in the cryostat at room temperature could cause an enormous amount of material to freeze onto the detector, target, and filters during the initial cooling of the cryostat, and will continue to deposit water on at least the LN2 filter, if not everywhere. The baking of the cryostat must be done with extreme care because the FAA paramagnetic salt irreversibly loses its crystalline structure when heated above 40 °C. [96, 97] While the salt pill can be kept

thermally isolated and monitored by a thermometer, other cryostat components are not so fortunate. An O-ring or epoxy seal always failed after baking, resulting in lost beam time and tedious repair.

In summary, it seems that the only reasonable solution is to use a UHV capable cryostat, with a hard seal loadlock and bake-able components. Constructing a separate UHV vacuum space within the cryostat is precluded by the conflicting requirements for precise positioning the target and for thermal isolation. We have recently built two new cryostats with UHV-compatible cold extensions to the exterior of the main body of the cryostat. This "snout" can be inserted into existing UHV XFA analysis chambers with the STJ and filters attached. This has eliminated the gas absorption problem.

6.5 Conclusions

This chapter demonstrated that the STJ spectrometer can be operated at a synchrotron facility to measure x-ray fluorescence from industrial and biological samples. In particular, metalloproteins containing trace amounts of transition metals can be studied in the soft x-ray region without interference from the intense oxygen fluorescence. The most dilute samples with fluorescence nearest the oxygen fluorescence line and edge, such as manganese in PSII, still remain out of reach. Some of the difficulties arise from outgassing and leaks of the detector chamber. There was a clear accumulation of water on all cold surfaces, which absorbs manganese x rays. Measuring such samples as PSII will require a custom designed cryostat that will maintain the sample, detector, and all intervening IR filters in a UHV environment. Finally, the background due to artifacts, line-shape tails, and scattered x rays also need to be reduced.

Appendix A

Details of Quasiparticle Cascade Calculations

A.1 Discrete Calculation

The discrete calculation is a fast alternative to repeated Monte Carlo calculations for calculating the cascade statistics. The energy of quasiparticles and phonons is first restricted to discrete values.

$$\begin{aligned} \omega_n &= \Delta + n\delta \quad n > 0 \\ \Omega_n &= n\delta \qquad n > 1 \\ \delta &= \Delta/10 \end{aligned} \tag{A.1}$$

The probability distribution for producing a given number of fully-relaxed quasiparticles is explicitly calculated for each possible initial quasiparticle or phonon energy. The cascade statistics for an initial x-ray-induced phonon population is calculated using these distributions.

This calculation is essentially recursive. The probability $P_s(\omega_i - \omega_f; \omega_i)$ of a quasiparticle with energy ω_i relaxing to an energy between ω_f and $\omega_f+\delta$ is calculated using equation 3.6. Likewise, the probability $P_{pb}(\omega;\Omega)$ of a phonon with energy Ω breaking a Cooper pair to produce a quasiparticle with energy between ω and $\omega+\delta$ is calculated using equation 3.7. The probability of a specific outcome, for a cascade starting with a single quasiparticle or phonon, can be calculated by summing the probabilities of all paths leading to the desired outcome. The probability of a given path

is the product of the probabilities for each specific relaxation or pair-breaking outcome. This calculation can be done quickly using the techniques of dynamic programming.

Dynamic programming accelerates recursive calculations by storing the results of the recursive sub-calculations. The total post-cascade quasiparticle count for the lowest energies are defined to be one quasiparticle for an initial quasiparticle with energy $\Delta \le \omega_i < 3\Delta$, and zero quasiparticles for an initial phonon with energy $\Omega < 2\Delta$.

$$\begin{aligned} D_{qp}(n;\omega) &= \mathbf{1} \quad \omega < 3\Delta \\ D_{ph}(n;\Omega) &= \mathbf{0} \quad \Omega < 2\Delta \end{aligned} \tag{A.2}$$

$\mathbf{n} \equiv$ distribution with 100% probability for n quasiparticles i.e. discrete delta function

Each of these quasiparticle outcome distributions (QODs) for the given energy ranges has a single outcome, with a probability of 100%. A quasiparticle with initial energy 3Δ has a small probability of emitting a phonon with energy 2Δ. The final QOD now has two outcomes: one quasiparticle with the probability of emitting a sub-gap phonon, or three quasiparticles with the probability of emitting a 2Δ phonon.

$$D_{qp}(n;\omega) = \left[\sum_{\Omega_i \le \omega - \Delta} P_s(\Omega_i) D_{ph}(n;\Omega_i) \right] * \mathbf{1} \tag{A.3}$$

This expression contains the discrete convolution operator, *. The sum of two discrete random variables is itself a random variable. The probability distribution of the sum is the convolution of the distributions of the summed variables:

$$\begin{aligned} D_{x+y}(x+y=n) &= \sum_{k,l} D_x(x=k) D_y(y=l) \delta_{k+l,n} = \sum_k D_x(x=k) D_y(y=n-k) \\ &= D_x * D_y \end{aligned} \tag{A.4}$$

A similar calculation is performed for an initial phonon with energy $2\Delta+\delta$, which requires the previously defined distributions for quasiparticles with energies Δ and $\Delta+\delta$. Since further phonon emission is possible from the two created quasiparticles, the QOD for the initial phonon is the convolution of the QODs for the created quasiparticles.

$$D_{ph}(n;\Omega) = \sum_{\Delta \le \omega_i \le \Omega/2} P_{ph}(\omega_i)\left[D_{qp}(n;\omega_i) * D_{qp}(n;\Omega-\omega_i)\right] \qquad \text{A.5}$$

Given this value, the QOD for a quasiparticle with energy $3\Delta+\delta$ may now be calculated. This process continues until quasiparticle distributions for all acoustic phonons energies have been calculated.

This technique was used to produce figures 3.2, and 3.7. However, it does not always reproduce the Monte Carlo results for a complete cascade, as presented in figure 3.6 and table 3.1. The two methods generally agree on estimates for epsilon, but the discrete calculation usually underestimates the value of the Fano factor. For example, using the electron-phonon coupling function of niobium generates estimates of $\varepsilon = 1.61$ and $F = 0.18$ which are similar to the Monte Carlo results. Using the functions for lead gives $\varepsilon = 1.55$ and $F = 0.08$, compared to $\varepsilon = 1.59$ and $F = 0.14$ using Monte Carlo. Further comparisons are shown in table A.1. Also, the discrete calculation was even more sensitive to the slightly perturbed α^2F functions of chapter 3 than the Monte Carlo calculations. This seems to be depressing the values of ε and F for non-Debye models.

Two other possible factors were considered. First, the separation between energy values, δ, was decreased to $\Delta/20$ with no change. Second, the Monte Carlo calculation contains some fluctuations in the initial phonon population. These fluctuations should

have a negligible effect on the Fano factor. Nevertheless, a calculation using random phonon populations and the QODs of the discrete calculation was performed with little change in the statistics. Since the Monte Carlo technique is conceptually more similar to the physical cascade process, it is the opinion of the author that the discrete calculation results should be considered qualitative and the Monte Carlo results should be used for more precise calculations.

Material	Δ (meV)	Monte Carlo		Discrete Calc.	
		ε/Δ	F ($10^3\,\sigma_F$)	ε/Δ	F
Debye-BCS	1.55	1.69	0.208 (3)	1.69	0.211
Nb	1.55	1.71	0.214 (2)	1.61	0.182
NbZr	1.83	1.74	0.223 (4)	1.65	0.193
Pb	1.40	1.59	0.140 (2)	1.55	0.080
Pb deposited at 2K	1.39	1.76	0.251 (5)	1.70	0.152
Pb as above, annealed	1.35	1.63	0.155 (3)	1.58	0.084
$Pb_{0.9}Cu_{0.1}$	1.33	1.91	0.284 (4)	1.89	0.203
In	0.56	1.68	0.210 (3)	1.58	0.174
bcc Ta	0.72	1.76	0.230 (5)	1.65	0.200
Al	0.17	1.70	0.216 (4)	1.59	0.180

Table A.1: Comparison of cascade statistics generated by Monte Carlo simulation and by summing discrete probabilities. The Monte Carlo calculations required 10000 repetitions and takes about 30 minutes, while the discrete calculations complete in a few seconds. The discrete calculations consistently predict smaller values of ε and F.

A.2 Monte Carlo Calculation

Material Parameters

The multilayer calculation must calculate the relative rates of the competing inelastic-scattering and ballistic-propagation processes. Table A.2 below contains the material parameters used in calculating these rates. These parameters are defined in Kaplan (1976) [13] and Kaplan (1979). [98] The values are also the same, with a few exceptions. The electron density of states and Fermi velocity for niobium have been taken from Soukoulis and Papaconstantopoulos. [99]

Parameter		Nb	Al
$N(0)$	states meV^{-1} m^{-3} spin^{-1}	53.2×10^{24} [a]	12.2×10^{24} [b]
$Z_1(0)$		1.94 [c]	1.43 [b]
b	meV^{-2}	4.0×10^{-3} [b]	$4 \times 0.317 \times 10^{-3}$ [bde]
Δ	meV	1.55 [f]	0.17 [f]
T_c	K	9.2 [f]	1.2 [f]
N_{ph}	ions m^{-3}	5.527×10^{28} [b]	6.02×10^{28} [b]
$<\alpha^2>_{av}$	meV	4.6 [b]	1.93 [b]
T_{Debye}	K	275 [b]	428 [b]
v_F	m s^{-1}	5.7×10^{5} [g]	2.0×10^{6} [h]
c_L	m s^{-1}	5140 [i]	6650 [i]
c_T	m s^{-1}	2170 [i]	3260 [i]
τ_0^*	ns	0.0201 [c]	24.2 [c]
τ_0^{ph*}	ns	0.0129 [c]	0.198 [c]

Table A.2: Material constants used in the cascade Monte Carlo calculations. Note that branch imbalance relaxation in aluminum is observed to be 4 times faster than predicted by Kaplan. This effect has been absorbed into the b factor, but omitted from $<\alpha^2>_{av}$. Also, the definitions of τ_0^* and τ_0^{ph*} differ slightly from that of Kaplan.

The electron-phonon renormalization factor for niobium has been computed from the α^2F function of niobium. The inelastic quasiparticle scattering rate has been increased by a factor of 4 in accordance with the observations of Chi and Clarke. [12] Finally, be aware that the characteristic times τ_0^* and τ_0^{ph*} of this work (denoted by the asterisk) differ from Kaplan's definitions. [13]

$$\tau_0^* = \frac{\hbar Z_1(0)}{2\pi b \Delta^3} \qquad \text{A.6}$$

$$\tau_0^{ph*} = \frac{\hbar N_{ph}}{4\pi N(0) < \alpha^2 >_{av} \Delta} \qquad \text{A.7}$$

[a] Soukoulis and Papaconstantopoulos (1979)[99]
[b] Kaplan (1976)[13]
[c] this work
[d] Chi and Clarke (1979)[12]
[e] Kirtley (1980)[100]
[f] CRC Handbook of Chemistry and Physics, 70th ed.[101]
[g] Weber (1991)[102]
[h] Kittel, Introduction to Solid State Physics, 2nd ed.[103]
[i] Kaplan (1979)[98]

In these expressions, Δ is the actual gap of the material, which may be proximitized. These coefficients were obtained by changing the variable of integration in equations (8) and (27) of the preceding reference to a dimensionless variable relative to Δ. At the same time, the substitutions $\alpha^2F(\Omega) = b\Omega^2$ and $\alpha^2(2\Delta) = <\alpha^2>_{av}$ have been applied.

Estimation of Tc

The gap of a superconductor depends on the nature of the electron-phonon coupling. Therefore, the superconducting gap was estimated for each of the perturbed α^2F functions used to generate figure 3.6 using the semi-empirical model of Carbotte: [50]

$$\omega_{ln} = \exp\left[\frac{2}{\lambda}\int_0^{\Omega_m} \frac{\alpha^2F(\Omega)\ln\Omega}{\Omega} d\Omega\right], \qquad \text{A.8}$$

$$kT_c = \frac{\omega_{ln}}{1.2}\exp\left[\frac{-1.04(1+\lambda)}{\lambda - \mu^*(1+0.62\lambda)}\right], \text{ and} \qquad \text{A.9}$$

$$\frac{2\Delta}{kT_c} = 3.53\left[1 + 12.5\left(\frac{T_c}{\omega_{ln}}\right)^2 \ln\left(\frac{\omega_{ln}}{2kT_c}\right)\right]. \qquad \text{A.10}$$

Material	Measured		Predicted		ω_{ln}	λ
	Δ	T_c	Δ	T_c		
Nb	1.55	9.2	1.45	8.66	11.876	0.9385
NbZr	1.83	10.9	1.35	10.1	8.526	1.3456
Pb	1.40	7.2	1.28	6.71	4.907	1.5559
Pb_{2K}	1.39	7.2	-	-	2.8596	-
Pb_{300K}	1.35	7.2	-	-	4.3588	-
$Pb_{0.9}Cu_{0.1}$	1.33	6.5	-	-	1.3137	-
In	0.56	3.4	0.53	3.24	5.849	0.8078
Ta (bcc)	0.72	4.1	0.71	4.46	10.131	0.7261
Al	0.17	1.20	0.18	1.20	25.073	0.3987

Table A.3: Moments of α^2F and predicted Δ and T_c for the materials studied in chapter 3, using the semi-empirical model of Carbotte.

The prediction is typically within 10%, for both weak-coupling superconductors like aluminum and strong-coupling superconductors like lead. Much of the error is due to the renormalized Coulomb pseudopotential μ^* being fixed to a value of 0.1.

Electron Transport

First, the range of contiguous layers that a quasiparticle is energetically allowed to enter is determined. Then, the probability of relaxing in a given layer is calculated. This probability is directly proportional to scattering rate of the quasiparticle and the layer thickness, and inversely proportional to the quasiparticle group velocity.

$$P_i \propto \frac{\tau_{s,i}^{-1}(\omega) d_i}{v_{F,i}\sqrt{1-(\Delta_i/\omega)^2}} \qquad \text{A.11}$$

This expression assumes that each quasiparticle enters and exits each accessible layer many times. This assumption is valid when the right hand side of equation (A.11) is much less than 1. For 200 nm niobium, this value is equal to 1 at 8.6 meV. This expression does not diverge at $\omega = \Delta$ when the low energy form of α^2F is quadratic.

Phonon Transport

In general, the phonons in this calculation are treated as longitudinal acoustic phonons, with averaged properties. A polarization-dependent value x is averaged as

$$< x >= (x_l + 2x_t)/3. \qquad \text{A.12}$$

This average was applied even for phonons with energies above the transverse Debye energy. An alternate average based on the relative densities of states,

$$< x >= \left(\frac{2x_t}{c_t^2} + \frac{x_l}{c_l^2}\right) \Big/ \left(\frac{2}{c_t^3} + \frac{1}{c_l^3}\right)^{2/3}, \qquad \text{A.13}$$

was rejected since it could lead to transmission probabilities greater than 1. This average could only be applied to phonons below the transverse Debye energy.

The interface transmissions $\eta_{l,t}$ for both polarizations were obtained from table II in Kaplan [98] and averaged as above. The presence of the AlO_x barrier was ignored, and perfect Al-to-Al transmission was assumed.

Coherence factors for quasiparticle-phonon interaction are mixed in character, energy dependent, and not well defined. [104] Therefore, the coherence factors appropriate for longitudinal phonons are used exclusively. Polarization is again ignored for all phonons, even those with energies greater than the Debye energy appropriate for a given polarization and material.

These phonons propagate ballistically within a given layer and are specularly reflected at boundaries and interfaces with a given transmission probability. [105] The average escape time is

$$\tau_{esc} = \frac{4d}{\eta_{top} + \eta_{bot}} \frac{3}{c_l + 2c_t}. \qquad \text{A.14}$$

The phonon is determined to break a pair or escape according to the relative probabilities $1/\tau_0 P^{ph*}(\Omega)$ and $1/\tau_{esc}$. If a pair is broken, then two quasiparticles are created in the current layer. If the phonon escapes, then the exit interface is randomly determined from the transmission probabilities, with the probability $P_{enter \to exit}$ given below.

Preference is given to the phonon exiting the interface opposite from the one it entered. The exception is when the phonon is newly created, in which case there is no bias.

$$P_{1\to 2} = \frac{\eta_2}{1-(1-\eta_1)(1-\eta_2)}$$
$$P_{1\to 1} = \frac{(1-\eta_2)\eta_1}{1-(1-\eta_1)(1-\eta_2)} \qquad \text{A.15}$$
$$P_{center\to 1,2} = \frac{(1-\eta_{2,1}/2)\eta_{1,2}}{1-(1-\eta_1)(1-\eta_2)}$$

The apparent increase in quasiparticle lifetime due to recombination phonons being re-adsorbed and breaking Cooper pairs was mentioned in chapter 5. The effective lifetime τ_r^* of a quasiparticle with a recombination rate τ_r^{-1} is estimated to be

$$\tau_r^* = \left(1+\tau_{esc}/\tau_0^{ph*}\right)/\tau_r^{-1} \qquad \text{A.16}$$

Random Number Selection

The source for uniform random numbers is the IEEE drand48() library function, which is supplied with most C compilers. The uniform distribution is transformed into the arbitrary distributions describing quasiparticle and phonon dynamics using two methods. The primary method is the acceptance-rejection, or von Neumann, method. A pair of uniform variates x and y are generated, one over the domain of the desired probability distribution P, and the other over the range. If $0 \le y < P(x)$, then the value x is returned. Otherwise, a new pair is generated. This method is exact for any probability distribution that can be loosely bounded. The singularity in the BCS DOS can be handled by a change of variable, with the effect that values of x near the singularity are selected more

frequently. The range can always be calculated explicitly for all the probability distributions used in this thesis.

The acceptance-rejection method is usually successful. However, the calculations using a model phonon DOS would inevitably stall. This occurs when the phonon peak is located at low energies, but is much taller than the Debye α^2F curve. The BCS variable transformation preferentially causes large values of x (phonon energy) to be selected, while the tall peak at low energy causes values of y larger than the value of the probability function at large x to be selected. As a result, almost every random pair results in rejection.

After 1000 rejected attempts, an alternate method is used. A uniform random variant y is calculated. Then, the definite integral, I, of the normalized probability P is calculated to a specified endpoint x. The value x is adjusted until $I(x)$ and y are approximately equal and x is determined to 8 decimals. This method converges in fewer than 5 iterations.

Spline Representation

As an experiment, the α^2F, DOS, and coherence factor functions of real materials were represented by spline polynomials, as opposed to tabulated values. The spline segments are defined by the value and second derivative of the modeled function at certain values of the independent variable. This representation had many advantages and one disadvantage. The advantages were:

- α^2F functions in the literature are scanned at high-resolution, and then are easily fit by splines so that there is no observable error between the scanned and spline curves,

- very compact storage, requiring 10 – 30 points despite containing peaks with high curvature and discontinuous slopes,
- rapid and accurate calculation of probability integrals and moments of α^2F, including ω_{ln}, and
- many primitive math functions may be performed in the spline representation which are used to construct the scattering and pair-breaking probability distributions, including addition and multiplication with a constant or ω^n.

The disadvantage to using the spline representation is the complexity of multiplying two functions. The product of two cubic spline segments is a sixth-order polynomial. This was approximated by a cubic segment with the same second derivative as the sixth-order polynomial at the endpoints. A segment endpoint in the product was located where an endpoint was located in *either* of the multiplying splines. Usually, endpoints are not coincident, so the number of point could double, or triple in the case of three multiplying factors. Coincident endpoints had to be identified and eliminated, since zero-length segments can produce division-by-zero errors. Sometimes rounding errors made coincident points distinct, which caused similar division errors. These spurious short segments also had to be identified and eliminated.

Proximity Effect

The properties of the proximitized aluminum and niobium were modeled according to the technique presented by Golubov and Houwman. [55] Their method partially linearizes the Usadel equations for the Green's functions $G(x,\omega^*)$ and $F(x,\omega^*)$, and order parameter $\Delta^*(x)$, under the assumption that one of the superconductors is thin relative to its coherence length. The coherence length of our aluminum is estimated to be about

350 nm, based on the residual resistivity of our aluminum films. The Golubov model can only be a rough approximation for our junctions. Attempts to model the I-V curves of the LLNL STJ junctions show this to be the case, although there are other explanations for the disagreement. [106] This model was included in the Monte Carlo simulations to account for the rounding of the BCS singularity in the DOS, as well as the small, but non-zero DOS below the gap energy of bulk niobium which is present in the proximitized niobium. This model was deemed adequate for this purpose.

The Golubov model requires as input the T_c, gap, thicknesses, and coherence lengths of the superconducting layers. It also requires two dimensionless parameters, γ_m and γ_B. The former parameter is a measure of the relative penetration of coherent electron states from one superconductor into the other. This should be a fully determined value based on the resistivities; however, it was varied so that the model predicted the measured gap energy. The latter is a measure of electron reflection at the interface. This may be caused by the Fermi velocity mismatch of the two materials, by impurities, or by grain effects. Usually, this value is small, and was taken to be zero so that there was only one free parameter.

The Golubov model outputs the complex Green's functions $G(x,\omega^*)$ and $F(x,\omega^*)$, and the real order parameter $\Delta^*(x)$. The quasiparticle DOS is simply the real part of G. The gap, $\Delta(x)$, is defined as the minimum energy where $\mathrm{Re}[G(x,\omega)]$ has an appreciable value. The Green's functions as defined by Usadel are:

$$G(x,\omega^*) = \frac{\omega^*}{\sqrt{\omega^{*2} + \Phi^2(x)}}, \text{ and} \qquad \text{A.17}$$

$$F(x,\omega^*) = \frac{\Phi(x)}{\sqrt{\omega^{*2} + \Phi^2(x)}}, \qquad \text{A.18}$$

where $\Phi(x)$ is the Usadel function. In the unproximitized limit, $\Phi(x) = \Delta^*(x) = \Delta(0)$. The parameter ω^* is a complex variable. The axis of real energy, ω, corresponds to $i\omega^*$.

It is important to note that the previously published coherence factors [18, 54, 107] cannot be used directly, as there is an inconsistency in the definition of F and G. [108] This can be seen by substituting the above definitions into those references and noting that the BCS coherence factors are not obtained in the BCS limit. For this thesis, the following substitutions were used in calculating scattering probabilities and rates:

$$N_s(\omega) = \mathrm{Re}[G(x,-i\omega)], \text{ and} \qquad \text{A.19}$$

$$N_s(\omega_2)\left(1 \pm \frac{\Delta^2}{\omega_1\omega_2}\right) \rightarrow \mathrm{Re}[G(x,-i\omega_2)]\left\{1 \mp \frac{\Delta}{\omega_1}\frac{\mathrm{Im}[F(x,-i\omega_2)]}{\mathrm{Re}[G(x,-i\omega_2)]}\right\}. \qquad \text{A.20}$$

For quasiparticle scattering, ω_1 is the initial energy and ω_2 is the final energy. For pair-breaking, ω_1 and ω_2 are the energies of the created quasiparticles. This expression is not strictly correct for pair-breaking. It *is* symmetric over interchange of ω_1 and ω_2 despite appearances, since $\omega_1 = \Omega - \omega_2$ and $\Delta \le \omega_1 \le \Omega/2$. However, the factor Δ/ω_1 is the BCS

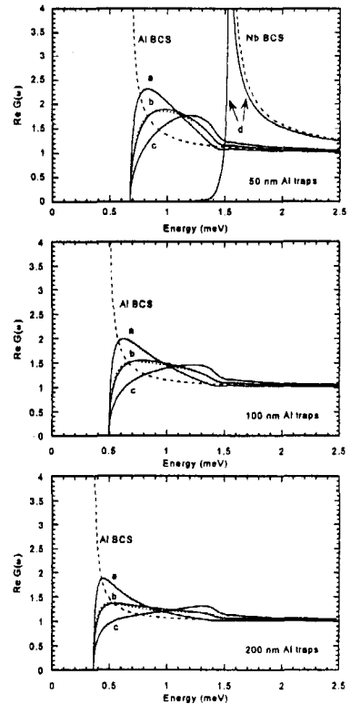

Figure A.1: Density of state functions for different thicknesses of aluminum: top) 50 nm, middle) 100 nm, bottom) 200 nm. The solid lines are the DOS in the niobium at a) 0.0, b) 0.5, c) 1.0, and d) 10.0 multiples of the niobium coherence length. The dashed lines are the BCS DOS functions for the measured gap used in the less-realistic multilayer calculation. The dotted line is the average of curves a, b, and c and was used to describe the proximitized niobium region in the more-realistic calculation. The DOS in the aluminum corresponds to curve a).

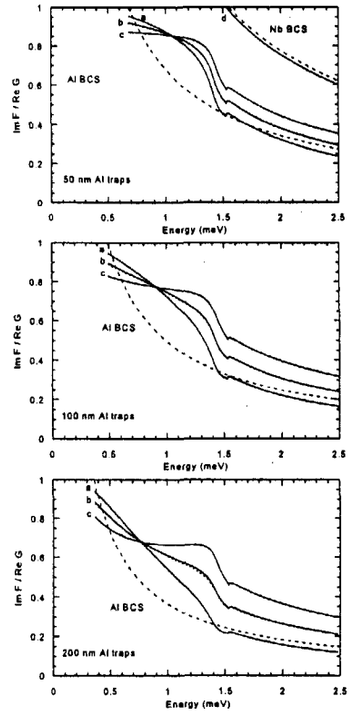

Figure A.2: The factor Im F / Re G that appears in the coherence factor for scattering and pair-breaking. The figure order and meanings of the lines and labels are the same as in figure A.3.

limit, and should be replaced by $\mathrm{Im}[F(x,-i\omega_l\,]]/\mathrm{Re}[G(x,-i\omega_l)]$ to be strictly correct. [86] The form of equation A.20 was used so that the scattering and pair-breaking probability functions could share the same factor, and to avoid an additional multiplication of spline functions.

A.3 Raw Results

The results of certain Monte Carlo runs are tabulated on the following pages. Each run contains three sections. The first section indicates the gap, layer geometry, and polarization-averaged phonon transmission of each layer, upwards through the top interface and downwards through the bottom interface. It also lists the characteristic times τ_0^*, τ_0^{ph*} and τ_{esc} as defined in equations A.6, A.7, and A.14. Absorption occurs in the layer marked by an asterisk, which is usually the top layer. Layers are numbered in ascending order, with layer 1 being the bottom layer.

The second section lists the number of pair-breaking and relaxation events that occur in each layer. The number in parentheses is the standard deviation. These events are further distinguished by whether the energy of the initial quasiparticle or phonon is above or below the niobium gap. Such events result in quasiparticles that are confined to the aluminum.

The third section summarizes the run in terms of the quasiparticle count and the cascade statistics ε and F. The total energy initially deposited as phonons is the greater of the two values, $10^4\Delta$ or $10^4\Omega_{Debye}/15$, for the designated layer of absorption. It also provides estimates of quasiparticle production based on the cascade occurring entirely in a single layer. In the confined cascade model, extra quasiparticles may be produced as quasiparticles leave the niobium and become trapped in the aluminum. This excess is

termed *trapping multiplication* and is nominally equal to 0 or 2 times the number of quasiparticles created in the niobium. The Monte Carlo summary contains a similar entry, "excess" due to "multiplication." This value is the difference between the number of quasiparticles produced, and the number that would be produced if confined to the primary absorber. This value is usually positive in a multilayer since the quasiparticles are not confined to the niobium. It can be negative, however, if an excessive amount of the phonon energy is lost into the substrate.

Simple 4-layer Model with 200 nm traps
Layer Description:

Layer	Gap	Size (nm)	Up	Down	Scatter (ns)	Breaking (ns)	Escape (ns)
1: Nb	1.55	240	0.43	0.34	0.013662	0.007702	0.396258
2: Al	0.35	200	1.00	0.80	2.758209	0.383136	0.101240
3: Al	0.35	200	0.80	1.00	2.758209	0.383136	0.101240
4: Nb*	1.55	160	0.00	0.43	0.013662	0.007702	0.474684

Cascade Events:

Layer	Pair Breaking Events				Relaxation Events			
	$\Omega < \Delta_{Abs}$		$\Omega > \Delta_{Abs}$		Not Trapped		Trapped	
1	0	(0)	22.939	(5.231)	103.596	(14.381)	0	(0)
2	2065.971	(41.757)	669.410	(25.609)	335.563	(23.793)	479.998	(22.761)
3	4614.293	(53.120)	2272.671	(41.504)	7177.321	(39.793)	2134.326	(44.846)
4	0	(0)	2708.740	(22.755)	4331.484	(40.875)	0	(0)

Summary:

Initial Energy E:	15812.5 meV	QP Count:	24708.048
ε:	0.639974 meV	Fano Factor:	0.309077 (0.015078)
Δ_{trap}:	0.35 meV	Δ_{Abs}:	1.55 meV
$\varepsilon/\Delta_{trap}$:	1.828496		
E/(1.7 Δ_{Abs}):	6000 (34)	E/(1.7 Δ_{trap}):	26575
"Excess" due to "Multiplication":		18707	

Simple 4-layer Model with 50 nm traps
Layer Description:

Layer	Gap	Size (nm)	Up	Down	Scatter (ns)	Breaking (ns)	Escape (ns)
1: Nb	1.55	240	0.43	0.34	0.013662	0.007702	0.396258
2: Al	0.70	50	1.00	0.80	0.344901	0.191568	0.02531
3: Al	0.70	50	0.80	1.00	0.344901	0.191568	0.02531
4: Nb*	1.55	160	0.00	0.43	0.013662	0.007702	0.474684

Cascade Events:

Layer	Pair Breaking Events				Relaxation Events			
	$\Omega < \Delta_{Abs}$		$\Omega > \Delta_{Abs}$		Not Trapped		Trapped	
1	0	(0)	24.000	(5.731)	70.669	(12.917)	0	(0)
2	89.664	(9.200)	512.493	(21.335)	10.553	(3.282)	0	(0)
3	131.033	(11.202)	811.188	(26.433)	700.071	(25.014)	0	(0)
4	0	(0)	2926.446	(20.197)	5547.289	(38.109)	0	(0)

Summary:

Initial Energy E:	15812.5 meV	QP Count:	8989.648
ε:	1.758968 meV	Fano Factor:	0.269174 (0.006173)
Δ_{trap}:	70 meV	Δ_{Abs}:	1.55 meV
$\varepsilon/\Delta_{trap}$:	2.512811		
E/(1.7 Δ_{Abs}):	6000 (34)	E/(1.7 Δ_{trap}):	13287 (51)
"Excess" due to "Multiplication":		2988	

100 nm Niobium Bi-layer
Layer Description:

Layer	Gap	Size (nm)	Up	Down	Scatter (ns)	Breaking (ns)	Escape (ns)
1: Nb	1.55	100	1.00	0.34	0.013662	0.007702	0.0944644
2: Nb*	1.55	100	0.00	1.00	0.013662	0.007702	0.126582

Cascade Events:

Layer	Pair Breaking Events				Relaxation Events			
	$\Omega < \Delta_{Abs}$		$\Omega > \Delta_{Abs}$		Not Trapped		Trapped	
1	0	(0)	47.203	(10.121)	0	(0)	21.252	(7.424)
2	0	(0)	2962.379	(19.833)	0	(0)	2553.419	(19.792)

Summary:

Initial Energy E:	15812.5 meV	QP Count:	6019.164
ε:	2.627026 meV	Fano Factor:	0.200458 (0.009721)
Δ_{trap}:	1.55 meV	Δ_{Abs}:	1.55 meV
$\varepsilon/\Delta_{trap}$:	1.694855		
E/(1.7 Δ_{Abs}):	6000 (34)	E/(1.7 Δ_{trap}):	6000 (34)
"Excess" due to "Multiplication":		18	

100 nm Niobium Bi-layer (free-standing)
Layer Description:

Layer	Gap	Size (nm)	Up	Down	Scatter (ns)	Breaking (ns)	Escape (ns)
1: Nb	1.55	100	1.00	0.00	0.013662	0.007702	0.126582
2: Nb*	1.55	100	0.00	1.00	0.013662	0.007702	0.126582

Cascade Events:

Layer	Pair Breaking Events				Relaxation Events			
	$\Omega < \Delta_{Abs}$		$\Omega > \Delta_{Abs}$		Not Trapped		Trapped	
1	0	(0)	47.876	(9.909)	0	(0)	21.507	(7.318)
2	0	(0)	2962.235	(20.534)	0	(0)	2553.843	(20.256)

Summary:

Initial Energy E:	15812.5 meV	QP Count:	6020.204
ε:	2.626572 meV	Fano Factor:	0.21855 (0.010527)
Δ_{trap}:	1.55 meV	Δ_{Abs}:	1.55 meV
$\varepsilon/\Delta_{trap}$:	1.694563		
E/(1.7 Δ_{Abs}):	6000 (34)	E/(1.7 Δ_{trap}):	6000 (34)
"Excess" due to "Multiplication":		19	

100 nm Aluminum Bi-layer
Layer Description:

Layer	Gap	Size (nm)	Up	Down	Scatter (ns)	Breaking (ns)	Escape (ns)
1: Al	0.17	100	1.00	0.71	24.079182	0.788810	0.0532843
2: Al*	0.17	100	0.00	1.00	24.079182	0.788810	0.0911162

Cascade Events:

Layer	Pair Breaking Events				Relaxation Events			
	$\Omega < \Delta_{Abs}$		$\Omega > \Delta_{Abs}$		Not Trapped		Trapped	
1	0	(0)	7823.049	(118.460)	0	(0)	9485.004	(217.532)
2	0	(0)	16398.074	(160.119)	0	(0)	28744.518	(271.436)

Summary:

Initial Energy E:	24610.0 meV	QP Count:	48442.246
ε:	0.508028 meV	Fano Factor:	2.342553 (0.133145)
Δ_{trap}:	0.17 meV	Δ_{Abs}:	0.17 meV
$\varepsilon/\Delta_{trap}$:	2.988398		
E/(1.7 Δ_{Abs}):	85155 (130)	E/(1.7 Δ_{trap}):	85155 (130)
"Excess" due to "Multiplication":		-36713	

100 nm Aluminum Bi-layer (free-standing)
Layer Description:

Layer	Gap	Size (nm)	Up	Down	Scatter (ns)	Breaking (ns)	Escape (ns)
1: Al	0.17	100	1.00	0.00	24.079182	0.788810	0.0911162
2: Al*	0.17	100	0.00	1.00	24.079182	0.788810	0.0911162

Cascade Events:

Layer	Pair Breaking Events				Relaxation Events			
	$\Omega < \Delta_{Abs}$		$\Omega > \Delta_{Abs}$		Not Trapped		Trapped	
1	0	(0)	17747.624	(147.354)	0	(0)	15155.525	(255.161)
2	0	(0)	24987.654	(149.290)	0	(0)	33098.998	(258.011)

Summary:

Initial Energy E:	24610.0 meV	QP Count:	85470.556
ε:	0.287935 meV	Fano Factor:	0.200600 (0.012937)
Δ_{trap}:	0.17 meV	Δ_{Abs}:	0.17 meV
$\varepsilon/\Delta_{trap}$:	1.693738		
E/(1.7 Δ_{Abs}):	85155 (130)	E/(1.7 Δ_{trap}):	85155 (130)
"Excess" due to "Multiplication":		314	

50 nm Aluminum Bi-layer

Layer Description:

Layer	Gap	Size (nm)	Up	Down	Scatter (ns)	Breaking (ns)	Escape (ns)
1: Al	0.17	50	1.00	0.71	24.079182	0.788810	0.0266422
2: Al*	0.17	50	0.00	1.00	24.079182	0.788810	0.0455581

Cascade Events:

Layer	Pair Breaking Events				Relaxation Events			
	$\Omega < \Delta_{Abs}$		$\Omega > \Delta_{Abs}$		Not Trapped		Trapped	
1	0	(0)	511.089	(101.418)	0	(0)	8766.715	(216.919)
2	0	(0)	1430.313	(138.112)	0	(0)	21827.277	(276.207)

Summary:

Initial Energy E: 24610.0 meV
QP Count: 31882.804
ε: 0.771889 meV
Fano Factor: 3.300033 (0.097850)
Δ_{trap}: 0.17 meV
Δ_{Abs}: 0.17 meV

E/(1.7 Δ_{Abs}): 85155 (130)
E/(1.7 Δ_{trap}): 85155 (130)
"Excess" due to "Multiplication": -53272

Simple 6-layer Model with 200 nm traps

Layer Description:

Layer	Gap	Size (nm)	Up	Down	Scatter (ns)	Breaking (ns)	Escape (ns)
1: Nb	1.55	210	1.00	0.34	0.013662	0.007702	0.198375
2: Nb	0.37	30	0.43	1.00	1.037696	0.032617	0.0266178
3: Al	0.37	200	1.00	0.80	2.412933	0.366387	0.101240
4: Al	0.37	200	0.80	1.00	2.412933	0.366387	0.101240
5: Nb	0.37	30	1.00	0.43	1.037696	0.032617	0.0266178
6: Nb*	1.55	130	0.00	1.00	0.013662	0.007702	0.164557

Cascade Events:

Layer	Pair Breaking Events				Relaxation Events			
	$\Omega < \Delta_{Abs}$		$\Omega > \Delta_{Abs}$		Not Trapped		Trapped	
1	0	(0)	10.545	(3.600)	52.962	(9.364)	0	(0)
2	449.119	(22.148)	118.458	(12.202)	218.591	(19.741)	108.496	(11.064)
3	523.951	(21.452)	223.171	(15.242)	179.196	(16.740)	88.950	(9.728)
4	1541.009	(35.322)	1105.424	(31.325)	4731.878	(54.930)	1138.926	(32.671)
5	3878.127	(49.297)	2576.210	(42.361)	5795.895	(61.755)	1396.778	(36.162)
6	0	(0)	2323.51	(24.176)	2986.962	(38.327)	0	(0)

Summary:

Initial Energy E: 15812.5 meV
QP Count: 25498.868
ε: 0.620126 meV
Fano Factor: 0.215591 (0.009357)
Δ_{trap}: 0.37 meV
Δ_{Abs}: 1.55 meV
$\varepsilon/\Delta_{trap}$: 1.694332
E/(1.7 Δ_{Abs}): 6000 (34)
E/(1.7 Δ_{trap}): 25413 (71)
"Excess" due to "Multiplication": 19497

Simple 6-layer Model with 100 nm traps

Layer Description:

Layer	Gap	Size (nm)	Up	Down	Scatter (ns)	Breaking (ns)	Escape (ns)
1: Nb	1.55	210	1.00	0.34	0.013662	0.007702	0.1983750
2: Nb	0.50	30	0.43	1.00	0.402163	0.023781	0.0266178
3: Al	0.50	100	1.00	0.80	0.935142	0.267127	0.0506201
4: Al	0.50	100	0.80	1.00	0.935142	0.267127	0.0506201
5: Nb	0.50	30	1.00	0.43	0.402163	0.023781	0.0266178
6: Nb*	1.55	130	0.00	1.00	0.013662	0.007702	0.1645570

Cascade Events:

Layer	Pair Breaking Events				Relaxation Events			
	$\Omega < \Delta_{Abs}$		$\Omega > \Delta_{Abs}$		Not Trapped		Trapped	
1	0	(0)	10.106	(3.157)	51.70	(10.128)	0	(0)
2	244.712	(15.503)	121.043	(12.528)	113.778	(15.372)	5.602	(2.321)
3	179.202	(13.680)	134.708	(11.698)	46.743	(7.894)	2.350	(1.533)
4	435.090	(19.926)	465.974	(22.079)	2233.044	(42.998)	39.652	(6.087)
5	2605.823	(44.238)	2581.533	(40.455)	5466.937	(50.928)	97.018	(10.054)
6	0	(0)	2438.371	(23.607)	3424.354	(40.529)	0	(0)

Summary:

Initial Energy E: 15812.5 meV
QP Count: 18433.124
ε: 0.857831 meV
Fano Factor: 0.306676 (0.015302)
Δ_{trap}: 0.50 meV
Δ_{Abs}: 1.55 meV
$\varepsilon/\Delta_{trap}$: 1.708826
E/(1.7 Δ_{Abs}): 6000 (34)
E/(1.7 Δ_{trap}): 18528 (60)
"Excess" due to "Multiplication": 12432

Simple 6-layer Model with 50 nm traps

Layer Description:

Layer	Gap	Size (nm)	Up	Down	Scatter (ns)	Breaking (ns)	Escape (ns)
1: Nb	1.55	210	1.00	0.34	0.013662	0.007702	0.198375
2: Nb	0.68	30	0.43	1.00	0.159680	0.017479	0.0266178
3: Al	0.68	50	1.00	0.80	0.371301	0.196336	0.025310
4: Al	0.68	50	0.80	1.00	0.371301	0.196336	0.025310
5: Nb	0.68	30	1.00	0.43	0.159680	0.017479	0.0266178
6: Nb*	1.55	130	0.00	1.00	0.013662	0.007702	0.164557

Cascade Events:

Layer	Pair Breaking Events				Relaxation Events			
	$\Omega < \Delta_{Abs}$		$\Omega > \Delta_{Abs}$		Not Trapped		Trapped	
1	0	(0)	8.701	(3.199)	39.781	(9.047)	0	(0)
2	30.130	(5.461)	100.208	(11.165)	23.981	(5.892)	0	(0)
3	14.224	(3.758)	66.897	(7.975)	4.984	(2.253)	0	(0)
4	28.407	(5.409)	173.398	(13.331)	489.297	(22.490)	0	(0)
5	456.758	(21.046)	2372.575	(37.477)	2397.456	(42.283)	0	(0)
6	0	(0)	2502.630	(22.247)	3670.340	(38.289)	0	(0)

Summary:

Initial Energy E: 15812.5 meV
QP Count: 11507.856
ε: 1.374061 meV
Fano Factor: 0.288971 (0.009199)
Δ_{trap}: 0.68 meV
Δ_{Abs}: 1.55 meV
$\varepsilon/\Delta_{trap}$: 2.011803
E/(1.7 Δ_{Abs}): 6000 (34)
E/(1.7 Δ_{trap}): 13618 (52)
"Excess" due to "Multiplication": 5506

Simple 6-layer Model with 200 nm traps (free-standing)
Layer Description:

Layer	Gap	Size (nm)	Up	Down	Scatter (ns)	Breaking (ns)	Escape (ns)
1: Nb	1.55	210	1.00	0.00	0.013662	0.007702	0.265823
2: Nb	0.37	30	0.43	1.00	1.037696	0:032617	0.0266178
3: Al	0.37	200	1.00	0.80	2.412933	0.366387	0.10124
4: Al	0.37	200	0.80	1.00	2.412933	0.366387	0.10124
5: Nb	0.37	30	1.00	0.43	1.037696	0.032617	0.0266178
6: Nb*	1.55	130	0.00	1.00	0.013662	0.007702	0.164557

Cascade Events:

Layer	Pair Breaking Events				Relaxation Events			
	$\Omega < \Delta_{Abs}$		$\Omega > \Delta_{Abs}$		Not Trapped		Trapped	
1	0	(0)	10.120	(3.537)	52.543	(9.547)	0	(0)
2	493.237	(23.57)	127.011	(12.496)	223.448	(19.702)	111.872	(11.004)
3	528.847	(22.438)	224.223	(14.855)	182.719	(17.379)	91.612	10.0230)
4	1542.891	(34.996)	1106.711	(31.973)	4732.306	(54.566)	1139.208	(32.501)
5	3880.470	(49.276)	2574.980	(42.064)	5792.310	(60.890)	1394.508	(35.171)
6	0	(0)	2322.875	(23.762)	2989.035	(37.677)	0	(0)

Summary:

Initial Energy E:	15812.5 meV	QP Count:	25622.73
ε:	0.617128 meV	Fano Factor:	0.199577 (0.007340)
Δ_{trap}:	0.37 meV	Δ_{Abs}:	1.55 meV
$\varepsilon/\Delta_{trap}$:	1.6816142		
$E/(1.7\ \Delta_{Abs})$:	6000 (34)	$E/(1.7\ \Delta_{trap})$:	25413 (71)
"Excess" due to "Multiplication":		19621	

Simple 6-layer Model with 100 nm traps (free-standing)
Layer Description:

Layer	Gap	Size (nm)	Up	Down	Scatter (ns)	Breaking (ns)	Escape (ns)
1: Nb	1.55	210	1.00	0.00	0.013662	0.007702	0.265823
2: Nb	0.50	30	0.43	1.00	0.402163	0.023781	0.0266178
3: Al	0.50	100	1.00	0.80	0.935142	0.267127	0.0506201
4: Al	0.50	100	0.80	1.00	0.935142	0.267127	0.0506201
5: Nb	0.50	30	1.00	0.43	0.402163	0.023781	0.0266178
6: Nb*	1.55	130	0.00	1.00	0.013662	0.007702	0.164557

Cascade Events:

Layer	Pair Breaking Events				Relaxation Events			
	$\Omega < \Delta_{Abs}$		$\Omega > \Delta_{Abs}$		Not Trapped		Trapped	
1	0	(0)	10.214	(3.620)	51.980	(0.989)	0	(0)
2	265.142	(17.464)	128.429	(12.247)	116.021	(15.216)	5.897	(2.383)
3	179.939	(13.755)	135.258	(12.233)	46.942	(7.838)	2.368	(1.518)
4	427.392	(20.398)	466.531	(20.451)	2236.123	(40.574)	40.106	(6.304)
5	2605.138	(44.078)	2578.754	(40.906)	5465.024	(48.994)	97.092	(9.770)
6	0	(0)	2439.093	(24.678)	3423.856	(39.108)	0	(0)

Summary:

Initial Energy E:	14812.5 meV	QP Count:	18491.78
ε:	0.855110 meV	Fano Factor:	0.298722 (0.007653)
Δ_{trap}:	0.50 meV	Δ_{Abs}:	1.55 meV
$\varepsilon/\Delta_{trap}$:	1.703406		
$E/(1.7\ \Delta_{Abs})$:	6000 (34)	$E/(1.7\ \Delta_{trap})$:	18528 (60)
"Excess" due to "Multiplication":		12490	

Simple 6-layer Model with 50 nm traps (free-standing)
Layer Description:

Layer	Gap	Size (nm)	Up	Down	Scatter (ns)	Breaking (ns)	Escape (ns)
1: Nb	1.55	210	1.00	0.00	0.013662	0.007702	0.265823
2: Nb	0.68	30	0.43	1.00	0.159680	0.017479	0.0266178
3: Al	0.68	50	1.00	0.80	0.371301	0.196336	0.025310
4: Al	0.68	50	0.80	1.00	0.371301	0.196336	0.025310
5: Nb	0.68	30	1.00	0.43	0.159680	0.017479	0.0266178
6: Nb*	1.55	130	0.00	1.00	0.013662	0.007702	0.164557

Cascade Events:

Layer	Pair Breaking Events				Relaxation Events			
	$\Omega < \Delta_{Abs}$		$\Omega > \Delta_{Abs}$		Not Trapped		Trapped	
1	0	(0)	8.683	(3.398)	39.546	(9.321)	0	(0)
2	32.465	(5.572)	106.115	(11.174)	24.455	(6.193)	0	(0)
3	14.181	(3.679)	67.646	(8.042)	4.927	(2.264)	0	(0)
4	28.616	(5.541)	173.342	(13.177)	488.832	(21.181)	0	(0)
5	454.766	(20.414)	2372.064	(37.617)	2396.149	(40.801)	0	(0)
6	0	(0)	2503.489	(23.330)	3671.112	(39.210)	0	(0)

Summary:

Initial Energy E:	15812 meV	QP Count:	11522.734
ε:	1.372287 meV	Fano Factor:	0.243281 (0.011210)
Δ_{trap}:	0.68 meV	Δ_{Abs}:	1.55 meV
$\varepsilon/\Delta_{trap}$:	2.009205		
$E/(1.7\ \Delta_{Abs})$:		$E/(1.7\ \Delta_{trap})$:	
"Excess" due to "Multiplication":		5521	

Golubov Proximity 6-layer Model with 200 nm traps
Layer Description:

Layer	Gap	Size (nm)	Up	Down	Scatter (ns)	Breaking (ns)	Escape (ns)
1: Nb	1.55	210	1.00	0.34	0.013662	0.007702	0.198375
2: Nb	0.35	30	0.43	1.00	1.294424	0.035111	0.0266178
3: Al	0.35	200	1.00	0.80	3.009898	0.394405	0.10124
4: Al	0.35	200	0.80	1.00	3.009898	0.394405	0.10124
5: Nb	0.35	30	1.00	0.43	1.294424	0.035111	0.0266178
6: Nb*	1.55	130	0.00	1.00	0.013662	0.007702	0.164557

Cascade Events:

Layer	Pair Breaking Events				Relaxation Events			
	$\Omega < \Delta_{Abs}$		$\Omega > \Delta_{Abs}$		Not Trapped		Trapped	
1	0	(0)	0.723	(0.963)	7.011	(3.405)	0	(0)
2	483.686	(20.869)	36.815	(6.509)	26.528	(6.322)	75.499	(9.255)
3	296.467	(17.276)	61.742	(7.870)	3.072	(1.748)	8.420	(2.999)
4	515.234	(21.548)	307.664	(17.199)	904.827	(29.224)	388.349	(19.350)
5	6022.176	(52.876)	3322.298	(44.848)	7746.536	(45.020)	3445.052	(51.385)
6	0	(0)	2857.366	(24.438)	4265.857	(42.719)	0	(0)

Summary:

Initial Energy E:	18031.8 meV	QP Count:	27808.342
ε:	0.648431 meV	Fano Factor:	0.205053 (0.012080)
Δ_{trap}:	0.35 meV	Δ_{Abs}:	1.55 /meV
$\varepsilon/\Delta_{trap}$:	1.907151		
$E/(1.7\ \Delta_{Abs})$:	6843 (36)	$E/(1.7\ \Delta_{trap})$:	31196 (78)
"Excess" due to "Multiplication":		20965	

Golubov Proximity 6-layer Model with 100 nm traps
Layer Description:

Layer	Gap	Size (nm)	Up	Down	Scatter (ns)	Breaking (ns)	Escape (ns)
1: Nb	1.55	210	1.00	0.34	0.013662	0.007702	0.1983750
2: Nb	0.50	30	0.43	1.00	0.407008	0.023876	0.0266178
3: Al	0.50	100	1.00	0.80	0.946408	0.268195	0.0506201
4: Al	0.50	100	0.80	1.00	0.946408	0.268195	0.0506201
5: Nb	0.50	30	1.00	0.43	0.407008	0.023876	0.0266178
6: Nb*	1.55	130	0.00	1.00	0.013662	0.007702	0.1645570

Cascade Events:

Layer	Pair Breaking Events				Relaxation Events			
	$\Omega < \Delta_{Abs}$		$\Omega > \Delta_{Abs}$		Not Trapped		Trapped	
1	0	(0)	2.919	(1.872)	19.500	(6.368)	0	(0)
2	237.914	(15.355)	43.298	(7.013)	45.124	(9.392)	3.055	(1.794)
3	142.203	(12.155)	55.726	(7.747)	3.436	(1.965)	0.268	(0.537)
4	220.444	(15.062)	170.408	(12.681)	596.140	(23.404)	11.956	(3.471)
5	1921.153	(40.163)	2842.585	(40.513)	7672.392	(42.383)	152.345	(12.200)
6	0	(0)	2902.620	(23.937)	4575.465	(42.859)	0	(0)

Summary:

Initial Energy E:	18031.8 meV	QP Count:	17078.54
ε:	1.055816 meV	Fano Factor:	0.325096 (0.012485)
Δ_{trap}:	50 meV	Δ_{Abs}:	1.55 meV
$\varepsilon/\Delta_{trap}$:	2.111632		
$E/(1.7\ \Delta_{Abs})$:	6843 (36)	$E/(1.7\ \Delta_{trap})$:	21213 (65)
"Excess" due to "Multiplication":	10235		

Golubov Proximity 6-layer Model with 50 nm traps
Layer Description:

Layer	Gap	Size (nm)	Up	Down	Scatter (ns)	Breaking (ns)	Escape (ns)
1: Nb	1.55	210	1.00	0.34	0.013662	0.007702	0.1983750
2: Nb	0.70	30	0.43	1.00	0.154870	0.017301	0.0266178
3: Al	0.70	50	1.00	0.80	0.360115	0.194344	0.0253100
4: Al	0.70	50	0.80	1.00	0.360115	0.194344	0.0253100
5: Nb	0.70	30	1.00	0.43	0.154870	0.017301	0.0266178
6: Nb*	1.55	130	0.00	1.00	0.013662	0.007702	0.1645570

Cascade Events:

Layer	Pair Breaking Events				Relaxation Events			
	$\Omega < \Delta_{Abs}$		$\Omega > \Delta_{Abs}$		Not Trapped		Trapped	
1	0	(0)	2.525	(1.809)	13.605	(5.458)	0	(0)
2	60.468	(7.917)	58.914	(8.226)	7.163	(3.248)	0	(0)
3	15.409	(3.869)	41.891	(6.601)	0.285	(0.533)	0	(0)
4	18.663	(4.366)	86.183	(9.112)	104.014	(10.242)	0	(0)
5	217.030	(14.551)	2526.598	(40.128)	2661.763	(45.042)	0	(0)
6	0	(0)	2920.832	(24.456)	4522.572	(43.274)	0	(0)

Summary:

Initial Energy E:	18031.8 meV	QP Count:	11897.026
ε:	1.515656 meV	Fano Factor:	0.251739 (0.015805)
Δ_{trap}:	0.69 meV	Δ_{Abs}:	1.55 meV
$\varepsilon/\Delta_{trap}$:	2.196603		
$E/(1.7\ \Delta_{Abs})$:	6843 (36)	$E/(1.7\ \Delta_{trap})$:	15372 (55)
"Excess" due to "Multiplication":	5053		

Golubov Proximity 6-layer Model with 200 nm traps (free-standing)
Layer Description:

Layer	Gap	Size (nm)	Up	Down	Scatter (ns)	Breaking (ns)	Escape (ns)
1: Nb	1.55	210	1.00	0.00	0.013662	0.007702	0.2658230
2: Nb	0.35	30	0.43	1.00	1.294424	0.035111	0.0266178
3: Al	0.35	200	1.00	0.80	3.009898	0.394405	0.1012400
4: Al	0.35	200	0.80	1.00	3.009898	0.394405	0.1012400
5: Nb	0.35	30	1.00	0.43	1.294424	0.035111	0.0266178
6: Nb*	1.55	130	0.00	1.00	0.013662	0.007702	0.1645570

Cascade Events:

Layer	Pair Breaking Events				Relaxation Events			
	$\Omega < \Delta_{Abs}$		$\Omega > \Delta_{Abs}$		Not Trapped		Trapped	
1	0	(0)	0.711	(0.956)	7.177	(3.409)	0	(0)
2	594.159	(23.903)	39.332	(6.754)	26.833	(6.480)	77.484	(9.603)
3	385.846	(19.832)	61.990	(7.907)	3.071	(1.827)	8.711	(2.935)
4	603.317	(24.541)	308.251	(17.158)	906.258	(28.024)	388.203	(19.228)
5	6062.161	(54.076)	3323.886	(46.743)	7743.394	(44.563)	3446.345	(53.410)
6	0	(0)	2855.68	(24.722)	4265.312	(43.708)	0	(0)

Summary:

Initial Energy E:	18031.8 meV	QP Count:	28470.702
ε:	0.633346 meV	Fano Factor:	0.220281 (0.009256)
Δ_{trap}:	meV	Δ_{Abs}:	1.55 meV
$\varepsilon/\Delta_{trap}$:	1.862782		
$E/(1.7\ \Delta_{Abs})$:	6843 (36)	$E/(1.7\ \Delta_{trap})$:	31196 (78)
"Excess" due to "Multiplication":	21627		

Golubov Proximity 100 nm traps (free-standing)
Layer Description:

Layer	Gap	Size (nm)	Up	Down	Scatter (ns)	Breaking (ns)	Escape (ns)
1: Nb	1.55	210	1.00	0.00	0.013662	0.007702	0.2658230
2: Nb	0.50	30	0.43	1.00	0.407008	0.023876	0.0266178
3: Al	0.50	100	1.00	0.80	0.946408	0.268195	0.0506201
4: Al	0.50	100	0.80	1.00	0.946408	0.268195	0.0506201
5: Nb	0.50	30	1.00	0.43	0.407008	0.023876	0.0266178
6: Nb*	1.55	130	0.00	1.00	0.013662	0.007702	0.1645570

Cascade Events:

Layer	Pair Breaking Events				Relaxation Events			
	$\Omega < \Delta_{Abs}$		$\Omega > \Delta_{Abs}$		Not Trapped		Trapped	
1	0	(0)	2.971	(1.977)	19.723	(6.217)	0	(0)
2	389.555	(19.102)	45.838	(7.313)	45.358	(9.872)	3.182	(1.828)
3	178.172	(13.483)	55.718	(7.393)	3.537	(1.912)	0.256	(0.512)
4	254.362	(15.607)	170.535	(12.754)	595.308	(22.690)	11.767	(3.347)
5	2021.176	(41.094)	2843.062	(41.709)	7672.565	(22.690)	153.132	(11.915)
6	0	(0)	2901.894	(24.698)	4579.733	(43.260)	0	(0)

Summary:

Initial Energy E:	18031.8 meV	QP Count:	17726.566
ε:	1.017219 meV	Fano Factor:	0.345940 (0.010960)
Δ_{trap}:	0.50 meV	Δ_{Abs}:	1.55 meV
$\varepsilon/\Delta_{trap}$:	2.034438		
$E/(1.7\ \Delta_{Abs})$:	6843 (26)	$E/(1.7\ \Delta_{trap})$:	21213 (65)
"Excess" due to "Multiplication":	10883		

Golubov Proximity 6-layer Model with 50 nm traps (free-standing)
Layer Description:

Layer	Gap	Size (nm)	Up	Down	Scatter (ns)	Breaking (ns)	Escape (ns)
1: Nb	1.55	210	1.00	0.00	0.013662	0.007702	0.2658230
2: Nb	0.70	30	0.43	1.00	0.154870	0.017301	0.0266178
3: Al	0.70	50	1.00	0.80	0.360115	0.194344	0.0253100
4: Al	0.70	50	0.80	1.00	0.360115	0.194344	0.0253100
5: Nb	0.70	30	1.00	0.43	0.154870	0.017301	0.0266178
6: Nb*	1.55	130	0.00	1.00	0.013662	0.007702	0.1645570

Cascade Events:

Layer	Pair Breaking Events				Relaxation Events			
	$\Omega < \Delta_{Abs}$		$\Omega > \Delta_{Abs}$		Not Trapped		Trapped	
1	0	(0)	2.669	(1.851)	13.789	(5.628)	0	(0)
2	106.838	(10.013)	64.669	(8.430)	7.360	(3.134)	0	(0)
3	21.107	(4.556)	41.431	(6.647)	0.273	(0.546)	0	(0)
4	23.932	(4.607)	86.103	(9.359)	103.960	(10.516)	0	(0)
5	248.308	(15.389)	2526.673	(39.296)	2660.431	(42.705)	0	(0)
6	0	(0)	2920.358	23.988	4520.854	(41.507)	0	(0)

Summary:

Initial Energy E:	18031.8 meV	QP Count:	12086.176
ε:	1.491936 meV	Fano Factor:	0.247038 (0.0054224)
Δ_{trap}:	0.69 meV	Δ_{Abs}:	1.55 meV
$\varepsilon/\Delta_{trap}$:	2.162226		
$E/(1.7\ \Delta_{Abs})$:	6843 (36)	$E/(1.7\ \Delta_{trap})$:	15372 (55)
"Excess" due to "Multiplication":		5242	

Absorption Layer Dependence: Simple 6-layer 50 nm traps
Absorption in Layer 1 (Base): E = 15812.5 meV

Layer	Pair Breaking Events				Relaxation Events			
	$\Omega < \Delta_{Abs}$		$\Omega > \Delta_{Abs}$		Not Trapped		Trapped	
1	0	(0)	2659.09	(22.686)	4249.676	(36.641)	0	(0)
2	298.596	(16.609)	1854.472	(34.347)	1717.085	(36.535)	0	(0)
3	18.547	(4.205)	127.172	(11.096)	351.395	(17.903)	0	(0)
4	9.109	(2.974)	50.733	(7.304)	3.712	(2.014)	0	(0)
5	19.997	(4.459)	79.487	(9.591)	18.336	(5.223)	0	(0)
6	0	(0)	5.167	(2.643)	21.491	(6.391)	0	(0)

QP Count:	10244.756	$\varepsilon/\Delta_{trap}$:	2.204961
ε:	1.543473 meV	Fano Factor:	0.317102 (0.017718)

Absorption in Layer 2: E = 15812.5 meV

Layer	Pair Breaking Events				Relaxation Events			
	$\Omega < \Delta_{Abs}$		$\Omega > \Delta_{Abs}$		Not Trapped		Trapped	
1	0	(0)	1818.579	(24.144)	4268.028	(39.263)	0	(0)
2	297.679	(16.569)	2718.479	(36.764)	1715.698	(37.181)	0	(0)
3	18.367	(4.322)	130.797	(11.508)	350.821	(18.851)	0	(0)
4	9.058	(3.095)	52.163	(7.125)	4.456	(2.171)	0	(0)
5	20.520	(4.600)	83.318	(11.023)	21.493	(6.170)	0	(0)
6	0	(0)	7.294	(3.295)	26.519	(8.033)	0	(0)

QP Count:	10312.508	$\varepsilon/\Delta_{trap}$:	2.19047
ε:	1.533332 meV	Fano Factor:	0.314511 (0.012013)

Absorption in Layer 3: E = 24610 meV

Layer	Pair Breaking Events				Relaxation Events			
	$\Omega < \Delta_{Abs}$		$\Omega > \Delta_{Abs}$		Not Trapped		Trapped	
1	0	(0)	2915.771	(42.835)	6411.565	(84.350)	0	(0)
2	425.157	(20.996)	2746.397	(52.083)	2487.449	(52.155)	0	(0)
3	27.589	(5.198)	939.140	(19.652)	508.554	(23.005)	0	(0)
4	15.821	(3.973)	173.243	(14.640)	72.983	(11.471)	0	(0)
5	78.996	(10.040)	473.329	(43.320)	357.712	(41.635)	0	(0)
6	0	(0)	274.515	(31.402)	589.384	(64.464)	0	(0)

QP Count:	16140	$\varepsilon/\Delta_{trap}$:	2.178246
ε:	1.524772 meV	Fano Factor:	0.320448 (0.017639)

Absorption in Layer 4: E = 24610 meV

Layer	Pair Breaking Events				Relaxation Events			
	$\Omega < \Delta_{Abs}$		$\Omega > \Delta_{Abs}$		Not Trapped		Trapped	
1	0	(0)	306.751	(32.384)	708.011	(70.611)	0	(0)
2	75.691	(9.492)	426.344	(34.881)	284.942	(31.032)	0	(0)
3	17.711	(4.193)	189.490	(14.333)	58.559	(9.494)	0	(0)
4	31.833	(5.557)	1003.829	(20.837)	664.777	(25.164)	0	(0)
5	497.845	(22.420)	3464.106	(59.178)	3246.217	(60.046)	0	(0)
6	0	(0)	2658.352	(41.851)	5518.237	(76.192)	0	(0)

QP Count:	17343.904	$\varepsilon/\Delta_{trap}$:	2.027061
ε:	1.418942 meV	Fano Factor:	0.264242 (0.014660)

Absorption in Layer 5: E = 15812.5 meV

Layer	Pair Breaking Events		Relaxation Events	
	$\Omega < \Delta_{Abs}$	$\Omega > \Delta_{Abs}$	Not Trapped	Trapped
1	0 (0)	10.758 (4.057)	43.518 (10.515)	0 (0)
2	22.972 (4.706)	100.119 (11.127)	23.721 (5.944)	0 (0)
3	10.772 (3.233)	67.143 (8.356)	4.803 (2.328)	0 (0)
4	21.757 (4.492)	175.346 (13.138)	456.737 (20.577)	0 (0)
5	351.647 (18.563)	3207.958 (41.216)	2235.487 (41.694)	0 (0)
6	0 (0)	1661.569 (24.780)	3664.425 (39.850)	0 (0)

QP Count: 11260.082 $\varepsilon/\Delta_{trap}$: 2.006139

ε: 1.404297 meV Fano Factor: 0.268893 (0.007751)

Absorption in Layer 6 (Counter): E = 15812.5 meV

Layer	Pair Breaking Events		Relaxation Events	
	$\Omega < \Delta_{Abs}$	$\Omega > \Delta_{Abs}$	Not Trapped	Trapped
1	0 (0)	8.243 (3.230)	37.401 (9.141)	0 (0)
2	22.634 (4.755)	96.963 (10.519)	20.782 (5.475)	0 (0)
3	10.553 (3.265)	66.369 (7.980)	4.260 (2.134)	0 (0)
4	21.802 4.707	170.902 (12.384)	457.257 (19.528)	0 (0)
5	353.050 (17.479)	2345.168 (36.919)	2240.566 (40.708)	0 (0)
6	0 (0)	2503.977 (22.272)	3648.740 (39.393)	0 (0)

QP Count: 11199.322 $\varepsilon/\Delta_{trap}$: 2.017023

ε: 1.411916 meV Fano Factor: 0.240725 (0.010031)

Appendix B

Magnetic Field Calculations

SIS tunnel junctions used for quasiparticle detection require the application of a magnetic field to suppress the tunneling of Cooper pairs (the Josephson supercurrent). A magnetic field tangential to the junction plane spatially modulates the supercurrent, and certain field strengths result in little or no net supercurrent. However, thin superconducting films are easily penetrated by fields that are perpendicular to the film. The penetrating flux is concentrated into *flux tubes* (or *discs*) where the superconductivity is suppressed. Quasiparticles can become trapped or lost in these regions. When a flux tube penetrates an electrode of an SIS tunnel junction, a small NIS or NIN junction is created at the flux tube. This increases the leakage current of the junction and decreases the dynamic resistance, resulting in reduced signal-to-noise ratio.

The STJ detector mount was constructed to reduce, but not necessarily eliminate, perpendicular field components. Even assuming perfect alignment of the detector with the magnet, a perpendicular field may exist for the following reasons: there is a gap in the solenoid to admit x-rays, the detector is usually not in the precise center of the field, and a cryogenic, high-permeability magnetic shield modifies the solenoid field. Since the effect of the magnetic shield cannot be easily measured, this appendix calculates the field using numerical methods.

Ordinarily, such computations involve three-dimensional dependence of vector quantities. However, by taking advantage of the cylindrical symmetry and the boundary properties of the magnetic shield material, the problem can be well-approximated by a simple two-dimensional Laplacian potential problem. The field is calculated in the vertical-radial (z-ρ) plane with Dirichlet boundary conditions on three boundaries, and Neumann boundary conditions on the $\rho = 0$ boundary.

First, the total magnetic field is decomposed into the solenoid field, B_{sol}, and the induced field, B_{ind}. The solenoid field can be calculated at any point in space using the law of Biot-Savart. After analytic integration over the z variable, this is a one-dimensional integral that can be evaluated numerically, or rewritten as elliptic integral functions if available. The induced field, on the other hand, is entirely determined by the static, induced currents at the problem's boundaries. It is therefore a solution to Laplace's equation and is the magnetic analogy to the electrostatic potential problem.

The permeability of the magnetic shield at 2 K is approximately 60,000. [58] The magnetic shield can therefore be considered to be an equipotential surface with less than 0.01% error. A magnetic scalar potential at the magnetic shield can be defined by computing the line integral along the shield surface. The magnetic scalar potential is single-valued since integration along the central axis is not allowed. Since the magnetic shield is an equipotential surface (defined to be zero), the potentials of the solenoid field and the induced field are equal and opposite at the magnetic shield boundary.

The magnetic shield problem is thus defined as:

$$B_{total} = B_{sol} + B_{ind}, \tag{B.1}$$

$$B_{ind}(\vec{r}) = \frac{aB_0}{4\pi}\int_0^{2\pi} d\theta' \left[\int_{z_1}^{z_2} \frac{\hat{\theta}\times(\vec{r}-\vec{r}')}{|(\vec{r}-\vec{r}')|^3} dz' + \int_{z_3}^{z_4} \frac{\hat{\theta}\times(\vec{r}-\vec{r}')}{|(\vec{r}-\vec{r}')|^3} dz' \right], \tag{B.2}$$

$$\vec{r}' = a\hat{\rho} + \theta'\hat{\theta} + z'\hat{z}$$

$$B_{ind}(\vec{r}) = -\nabla \Phi_{ind}(\vec{r}), \text{ with} \tag{B.3}$$

$$\nabla^2 \Phi_{ind}(\vec{r}) = 0 \text{ (cylindrical coordinates)}, \tag{B.4}$$

and with the boundary conditions

$$\Phi_{ind}(\vec{r}) - \int_C \vec{B}_{ind} \cdot d\vec{l} = 0, \vec{r} \text{ on } \vec{C} \equiv \{z = 0, z = z_{max}, \rho = \rho_{max}\}$$

$$\left.\frac{\partial \Phi_{ind}(\vec{r})}{\partial \rho}\right|_{\rho=0} = 0 \tag{B.5}$$

The parameters a and z_1 through z_4 are the radius and endpoints of the solenoid coils (see figure B.1). The parameters z_{max} and ρ_{max} are the height and radius of the magnetic shield. The geometry is shown in figure B.1. Values for these parameters are given in table B.1. The value B_0 is the on-axis field of an equivalent solenoid of infinite length.

The scalar potential was evaluated on a grid of 40 by 40 points, shown schematically in figure B.1. These points were offset from the origin by one-half of the lattice spacing to avoid the singularity at the $\rho = 0$ boundary. The differential equation was discretized using the standard finite-difference expressions that include only the nearest neighboring points. These expressions were modified to directly incorporate the boundary condition for points adjacent to the boundary, while correctly accounting for the half-lattice spacing between the boundary and the point being computed. For

Parameter	Value	Parameter	Value
coil 1 bottom (z_1)	1.55 cm	coil radius (a)	3.46 cm
coil 1 top (z_2)	5.28 cm	shield radius (ρ_{max})	5.08 cm
coil 2 bottom (z_3)	6.48 cm	shield height (z_{max})	11.2 cm
coil 2 top (z_4)	10.2 cm	detector plane offset	0.889 cm

Table B.1: Size and position of the magnetic coils, magnetic shield, and the offset from the central axis of the plane in which the STJ detector is mounted.

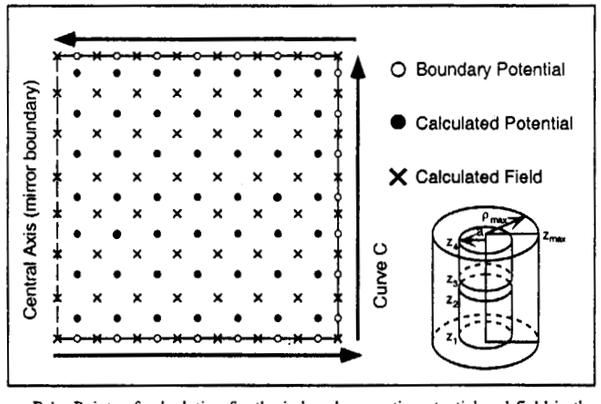

Figure B.1: Points of calculation for the induced magnetic potential and field in the ρ-z plane. The boundary potential is calculated by integrating the solenoid field along the path C. The internal potential is calculated by solving the finite-difference form of Laplace's equation. The induced field is then calculated from the finite-difference gradient of the potential. All finite-difference expressions have a modified form near the boundary because of the half-lattice spacing of the boundary points.

example, the first and second normal derivatives at the radial surface of the magnetic shield have the finite-difference expressions:

$$\left.\frac{\partial\Phi(\rho,z)}{\partial\rho}\right|_{\rho=\rho_{max}-\delta\rho/2} = \frac{4\Phi(\rho+\delta\rho/2,z)-3\Phi(\rho,z)-\Phi(\rho-\delta\rho,z)}{3\delta\rho}+O\left[(\delta\rho)^3\right]$$
$$\left.\frac{\partial^2\Phi(\rho,z)}{\partial\rho^2}\right|_{\rho=\rho_{max}-\delta\rho/2} = \frac{4}{3}\frac{2\Phi(\rho+\delta\rho/2,z)-3\Phi(\rho,z)+\Phi(\rho-\delta\rho,z)}{(\delta\rho)^2}+O\left[(\delta\rho)^3\right] \quad \text{B.6}$$

where $\Phi(\rho+\delta\rho/2,z)$ is the known boundary value. The complete system of finite-difference equations was accurate to third-order or better. The gradient of the scalar potential was computed using similar expressions to obtain the ρ and z components of the induced field. These calculations and following figures were computed using the IDL [109] programming language, which in turn uses the sparse linear systems routines presented in Numerical Recipes. [110]

The calculated fields are shown in the following figures. Each field is plotted twice: once with vectors indicating field direction and magnitude, and once with streamlines of constant length. All vector figures have the same magnitude scale, in which the on-axis solenoid vectors are approximately $0.75B_0$. The streamline figures better indicate how the magnetic shield affects the field, and how the field deviates from the parallel ideal. Figure B.2 is a plot of the solenoid field calculated from the Biot-Savart law. The field deviates from the ideal field of an infinite solenoid at the ends and near the gap in the coils. There will be a non-zero component perpendicular to the STJ junction if there is a non-zero radial component. A typical detector is located at a height of 5.75 cm and radius of 1.5 cm, and should experience a perpendicular component.

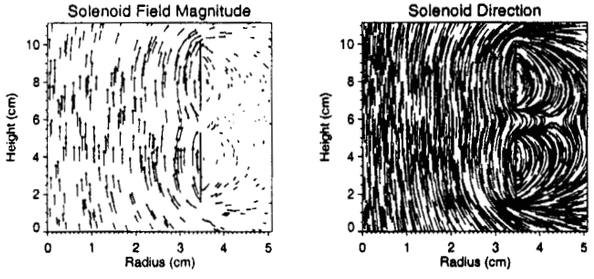

Figure B.2: Solenoid Field: The figure on the left plots 400 randomly placed vectors directed along the field with length proportional to the field strength. The figure on the right plots 2000 streamline segments. The two vertical lines at 3.5 cm indicate the solenoid current surfaces.

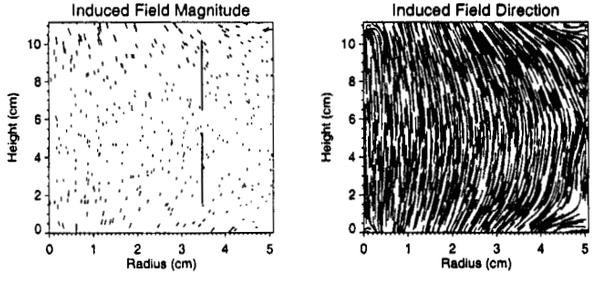

Figure B.3: Induced Field: The main effect of the magnetic shield is eliminate the component tangent to the magnetic shield.

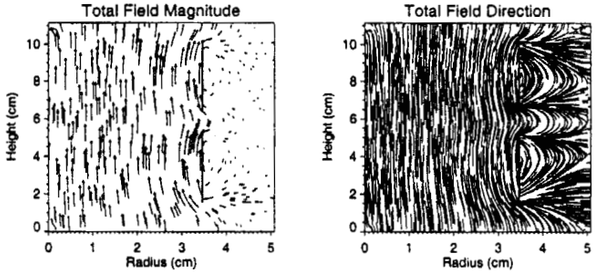

Figure B.4: Combined solenoidal and induced magnetic fields: The magnetic shield has strengthened and made parallel the near-axis field to approximate the infinite solenoid.

Figure B.3 is a plot of the induced field. The induced field cancels the component of the solenoid that is tangent to the magnetic shield. Most of its field is located near the top and bottom surfaces. Figure B.4 is the actual field within the magnetic shield. The magnetic shield has strengthened and made parallel the near axis-field so that it closely approximates the infinite solenoid. However, the distortion near the solenoid gap remains almost as strong.

These calculations must be projected into the detector coordinate system to determine what effect the radial field component will have. The STJ detectors are mounted on a cold extension which is co-axial with the magnet and shield. The detectors are translated off-axis by the thickness of this cold extension, the mounting plate, and the detector substrate. In addition, up to 4 detectors may be mounted in a horizontal line on the mounting plate. In the cylindrical geometry of this calculation, the detectors are on a secant line that is offset 0.9 cm from the axis (see figure 4.9). Figure B.5 below plots the strength of the perpendicular component in units of B_0, with and without a magnetic

shield. It shows that about 2% of the applied field may appear as a perpendicular field for a typical detector mounting. This increases to 10% if the shield is omitted.

Figure B.6 shows the magnetic field that is within the plane of the junction. This is not a critical factor for junction performance. However, the expected suppression of the Josephson current assumes a parallel, vertical, and uniform field of a particular strength. A typical detector mounting will see some slight non-uniform field if the shield is omitted.

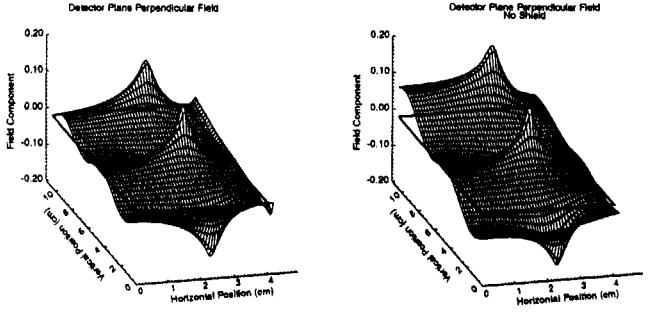

Figure B.5: Surface plot of the perpendicular component of the magnetic field at the detector plane, with and without the magnetic shield. Values at negative and positive horizontal positions are equal.

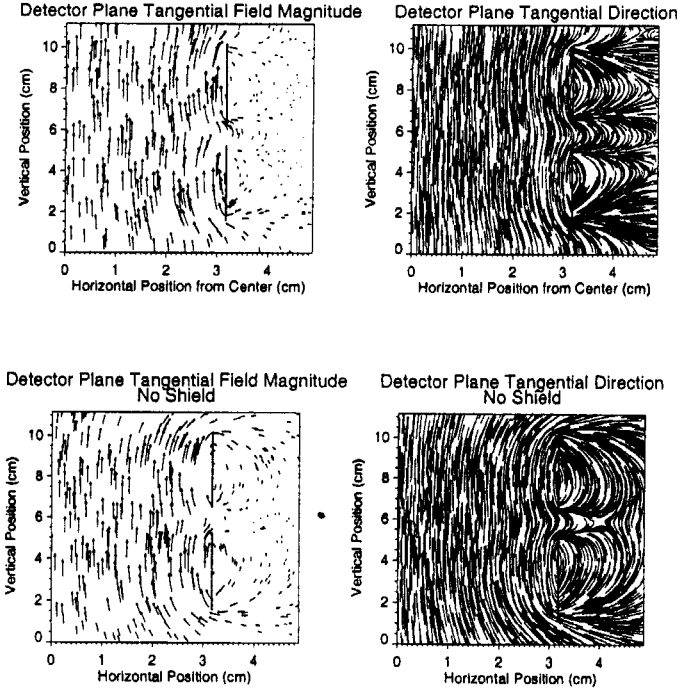

Figure B.6: Tangential Fields in the plane of the detector, with and without the magnetic shield. A typical detector will be located 1 cm from the center of the detector mount.

Appendix C

Derivation of Tunneling Noise

If each quasiparticle tunnels exactly once, the resolution of the STJ spectrometer is limited by the fluctuations in the number of particles created, by spatial dependence in the detector, and by the electronic noise of the amplifier circuit. Electronic noise is often the dominant noise source because the tunneling current is very small. However, by creating quasiparticle traps on both sides of the tunnel barrier, it is possible for quasiparticles to tunnel repeatedly during their lifetime. This increases the total tunneled charge and can reduce the relative contribution of electronic noise in the amplifier circuit. However, since the actual number of times a quasiparticle will tunnel will fluctuate about a mean value, the total measured charge must fluctuate between nominally identical x-ray absorption events. Multiple tunneling designs offer a trade-off between increased signal size and increased tunneling shot noise.

C.1 Full Integration, Symmetric Junction

Previous works have derived the noise due to multiple tunneling with complete integration. Mears, *et al.* [10] considered the probability of a quasiparticle with average lifetime τ_r tunneling exactly n times and then recombining at time t:

$$p(n,t) = \frac{e^{-t/\tau_r}}{\tau_r} P_P(n; t/\tau_t), \qquad \text{C.1}$$

where $P_P(n;\mu)$ is the Poisson distribution with mean μ, τ_r is the lifetime and τ_t is the inverse tunneling rate. The lifetimes and tunneling rates of the two junction electrodes are taken to be identical on both sides. The probability of tunneling exactly n times during the pulse is found by integration:

$$P(n,\infty) = \int_0^\infty p(n,t')dt' = \frac{\tau_r^n \tau_t}{(\tau_r + \tau_t)^{n+1}}. \qquad \text{C.2}$$

This probability distribution has mean $\langle n \rangle_{av} = \tau_r/\tau_t$, and variance $\langle n \rangle_{av}(1+\langle n \rangle_{av})$. The Fano-like noise term is $F' = (1+1/\langle n \rangle_{av})$. The average number of tunnels $\langle n \rangle_{av}$ is equal to the charge multiplication due to multiple tunneling. The noise term F' is always greater than one and much greater than the fluctuations in number of initially created quasiparticles, characterized by $F \sim 0.2$.

C.2 Full Integration, Asymmetric Junction

Goldie *et al.* [33] derived an expression for the case where the quasiparticle decay and tunneling rates may not be identical for quasiparticles on both sides of the barrier. Given the probability of tunneling from layer i ($i = 1,2$):

$$P_i = \frac{\tau_{t_i}^{-1}}{\tau_{t_i}^{-1} + \tau_{r_i}^{-1}}, \qquad \text{C.3}$$

and the probability of being lost in layer i, $1-P_i$, the probability distribution of a quasiparticle initially in layer 1 that tunnels exactly n times is:

$$P(n,\infty) = \begin{cases} P_1(1-P_2)(P_1P_2)^{(n-1)/2} & \text{n odd} \\ (1-P_1)(P_1P_2)^{n/2} & \text{n even} \end{cases}. \qquad \text{C.4}$$

This probability distribution has mean $\langle n\rangle_{av} = P_1(1+P_2)/(1-P_1P_2)$ and variance $[P_1-P_1^2+3P_1P_2+P_1^2P_2]/(1-P_1P_2)^2$. The Fano-like noise term is $F' = [1-P_1+3P_2+P_1P_2]/[P_1(1+P_2)^2]$.

C.3 Partial Integration, Symmetric Junction

The preceding calculations are of the total accumulated charge noise after an infinitely long integration of the tunnel current. By contrast, an ideal current-measuring amplifier should be able to measure the initial quasiparticle current without either gain or noise due to multiple tunneling. A realistic current amplifier or a shaping amplifier will have some limited integration. I now extend these calculations to finite integration windows.

First, equation C.2 is re-written to include only the tunneling events that occur before a time t (not to be confused with the t in equation C.1, which is now the variable of integration t'):

$$P(n,t) = \int_0^t \frac{e^{-t'/\tau_r}}{\tau_r} P_p(n;t'/\tau_t)dt' + P_p(n;t/\tau_t)e^{-t/\tau_r}. \qquad \text{C.5}$$

The moments of this function with respect to n are readily obtained by first calculating the moment generating function of $P(n,t)$:

$$f(s,t) = \sum_{k=0}^{\infty} s^k P(k;t) = \frac{1+\langle n\rangle_{av}(1-s)\exp\{-[1+\langle n\rangle_{av}(1-s)]t/\tau_r\}}{1+\langle n\rangle_{av}(1-s)}. \qquad \text{C.6}$$

The average charge accumulated by time t and the variance about this average is calculated from the moment generating function:

$$Q(t) = eN\langle n\rangle_{av}\left(1-e^{-t/\tau_t}\right), \qquad \text{C.7}$$

$$\sigma_Q^2(t) = e^2N\left[\langle n\rangle_{av} + \langle n\rangle_{av}^2 - e^{-t/\tau_r}\left(2\langle n\rangle_{av}^2\frac{t}{\tau_r} + \langle n\rangle_{av}\right) - \langle n\rangle_{av}^2 e^{-2t/\tau_r}\right], \qquad \text{C.8}$$

where N is the mean number of quasiparticles in the trap and $\langle n\rangle_{av} = \tau_r/\tau_t$ as previously defined. The average current at time t, and a measure of the distribution of current about this average for different current pulses is obtained by differentiating with respect to t:

$$I(t) = \frac{eN}{\tau_t}e^{-t/\tau_r}, \qquad \text{C.9}$$

$$S_I^2(t) = \frac{e^2N}{\tau_t}e^{-t/\tau_r}\left[1+2\langle n\rangle_{av}\left(\frac{t}{\tau_r}-1+e^{-t/\tau_r}\right)\right]. \qquad \text{C.10}$$

The noise term F' is defined as $\sigma_Q^2(t) / (Q^2(t) / N)$.

C.4 Partial Integration, Asymmetric Junction

Samedov has recently introduced a formalism that will allow one to compute the moments of the multiple tunneling distribution function for arbitrary rate constants. [111] He considers an equivalent system: an infinite multilayer in which quasiparticles can tunnel in only one direction, through successive layers. The function $f(s,t)$ for this system is:

$$\begin{aligned} f(s,t) = {} & 1 + \frac{(s-1)\Gamma_t^{(l)}}{\Gamma^2 - (\Delta\Gamma)^2 - \Gamma_t^{(l)}\Gamma_t^{(r)}s^2} \times \\ & \left\{\left(\Gamma + \Delta\Gamma + \Gamma_t^{(r)}s\right)\left[1 - e^{-\Gamma t}\cosh\left(t\sqrt{(\Delta\Gamma)^2 + \Gamma_t^{(l)}\Gamma_t^{(r)}s^2}\right)\right] - \right. \\ & \left[\sqrt{(\Delta\Gamma)^2 + \Gamma_t^{(l)}\Gamma_t^{(r)}s^2} + \frac{\Gamma\left(\Delta\Gamma + \Gamma_t^{(r)}s\right)}{\sqrt{(\Delta\Gamma)^2 + \Gamma_t^{(l)}\Gamma_t^{(r)}s^2}}\right] \times \\ & \left. e^{-\Gamma t}\sinh\left(t\sqrt{(\Delta\Gamma)^2 + \Gamma_t^{(l)}\Gamma_t^{(r)}s^2}\right)\right\} \end{aligned} \qquad \text{C.11}$$

where $\Gamma_t^{(l,r)}$ is the tunnel rate from the left and right electrodes, $\Gamma_r^{(l,r)}$ is the quasiparticle removal rate in the left and right electrode, $\Gamma = [\Gamma_r^{(l)} + \Gamma_r^{(r)}]/2$, and $\Delta\Gamma = [\Gamma_r^{(r)} - \Gamma_r^{(l)}]/2$. For symmetric junctions, this function reduces to

$$f(s,t) = 1 + \frac{(s-1)\Gamma_t}{\Gamma_r - \Gamma_t s}\left[1 - e^{-\Gamma_r t} e^{\Gamma_t s t}\right], \qquad \text{C.12}$$

while for infinite integration it is simply

$$f(s,\infty) = 1 + \frac{(s-1)\Gamma_t^{(l)}\left(\Gamma_r^{(r)} + \Gamma_t^{(r)} s\right)}{\Gamma_r^{(l)}\Gamma_r^{(r)} - \Gamma_t^{(l)}\Gamma_t^{(r)} s^2}. \qquad \text{C.13}$$

These functions can be used to calculate the mean and variance of the charge and current for arbitrary values of the loss rates, tunnel rates, and integration window. However, care must be taken that the following definition for $\Gamma_r^{(l,r)}$ is used:

$$\Gamma_r^{(l,r)} = \frac{1}{\tau_r^{(l,r)}} + \frac{1}{\tau_t^{(l,r)}}. \qquad \text{C.14}$$

Note that equation C.13 can be re-written using Goldie's notation as[a]:

$$f(s,\infty) = 1 + \frac{(s-1)P_t(1 + P_r s)}{\left(1 - P_t P_r s^2\right)}. \qquad \text{C.15}$$

All of the various limits for $I(t)$, $Q(t)$, $S_I^2(t)$, $\sigma_Q^2(t)$, and F' described in this appendix follow directly from equations C.11 through C.15, with equation C.11 applicable to the most general case.

[a] Equation (18) of reference [111] incorrectly defines P_1 and P_2 as their reciprocals and so differs from equation C.15. The results of Goldie are properly obtained from equation C.15.

Appendix D

Setup Procedures for SSRL

D.1 Baking Procedure

The vacuum cart (see figure 6.2) must be baked after being exposed to air to attain the required UHV conditions. Care must be taken since many of the components use Viton O-ring gaskets. The vacuum system is wrapped with six heating tapes and thermocouples. The heating controller is turned on and all gate valves except the backfill valve are opened. The setpoints are adjusted until thermocouples 1-5 read 200 degrees Celsius and thermocouple 6 (nearest the backfill gate valve) reads 160 degrees Celsius. The ion-pump heater is also turned on. The vacuum system is pumped on continuously by the auxiliary turbopump. When the vacuum pressure reaches 1×10^{-6} Torr the HV and UHV pressure sections are isolated by the windowless gate valve. The ion pump is turned on and the ion pump heater is turned off. The initial baking continues for at least 24 additional hours.

Subsequent baking sessions, e.g. following venting the HV section to replace the cryostat isolation gate valve or the manipulator arm, are performed with all gate valves closed with the exception of the window valve and the valve to the auxiliary turbo pump. In this situation, all heater settings are adjusted so that no thermocouple exceeds 160 degrees Celsius. The ion pump continues to pump on the UHV section as usual.

D.2 Alignment and Focusing

The vacuum cart must be aligned with the beam after being attached to the beamline and attaining the required UHV vacuum. This was done by attaching a window flange at the approximate location of the STJ detectors. The beam is positioned by adjusting the cart jack screws until the beam spot is centered in the crosshairs of the fluorescent window. On beamline 10-1, it is important that this procedure is performed **only** with diffracted light from the monochromator, as that beam is too intense to safely use zero-order light. Beamline 1-1 requires the use of zero-order light, however.

Beamline 10-1 has a small beam with low divergence. In general, it is not necessary to adjust the focus of this beamline. The beamline 1-1 focus is adjustable from one to several meters by means of a flexible mirror. The curvature of the mirror is adjusted by a screw on an edge of the mirror, while three other screws adjust the position of the mirror. The vertical position of the beam and the focal length must be adjusted simultaneously to keep the beam in the center of the window crosshairs. The focusing is performed with zero-order light. The photodiode, positioned after the refocusing mirror, should be adjusted to pass the light reflected from the monochromator but block other light paths, particularly the path collinear with the exit and entrance slit. Adjusting the curvature of the mirror projects the patterns shown in figure D.2 on the phosphor window.

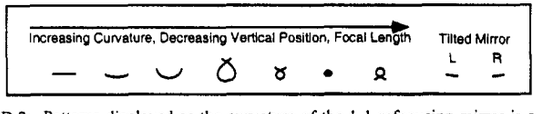

Figure D.2: Patterns displayed as the curvature of the 1-1 refocusing mirror is adjusted. Minimum spot size is 0.3 x 1.0 mm.

At this point, the cart is taken to be correctly positioned. For the second, optional stage of aligning the cryostat, a 1.25" Plexiglas plate is fastened the bottom of the cryostat, with the lids to each temperature stage cylinder omitted. Phosphor is placed at the detector location, or on a sample tip. The cryostat is mounted on the cart, evacuated, and cooled to 77 K to reduce the pressure below the required 5×10^{-6}. At this point, the beam is opened and the cryostat is manipulated to located the beam on the fluorescence target or a detector. As before, the monochromator on 10-1 must not be set to zero-order, while on 1-1 zero-order should be used. Further refinements are made during the actual experiment by observing the count rate of on the STJ detector.

D.3 Photodiode and Channeltron

Two instruments are available to assist with intensity measurements and calibration, the photodiode and the channeltron. Both instruments measure the production of photoelectrons, and their high-voltage wiring is described in figure D.3. The photodiode is simply a metal electrode exposed to the beam, which emits photoelectrons. The electrode is mounted on a linear manipulator with several stations which includes: a through-opening, a stainless steel grid, and a gold foil. It is also coated with phosphor so the beam is visible when it illuminates the electrode. A nearby ring electrode, biased at +100 V (beamline 1-1) or +75 V (beamline 10-1), collects the emitted electrons. The emitter is grounded through a Keithley electrometer which measures the photocurrent. The electrometer output is input to a voltage-to-frequency converter and finally a CAMAC hex scaler. The beamline software can automatically scan the monochromator position and record the electron intensity. The absolute intensity of the beam may be determined with the gold foil, given the photon-to-electron conversion efficiency for a

given energy. The stainless steel grid allows continuous, relative intensity measurements to be performed during an experiment since it does not block the entire beam.

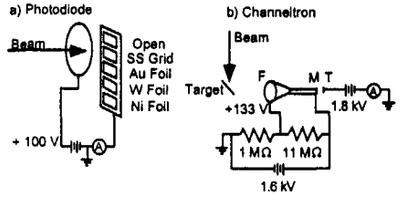

Figure D.3: Schematic of bias and measurement circuits for the photodiode and channeltron. The Channeltron leads are labeled (F)ront, (M)iddle, and (T)ail. The electrometer input is the non-ground input to the ammeter. The 1.8 kV supply is a battery with an isolated negative pole.

The photodiode at beamline 10-1 is similar. It is positioned before the final focusing mirror, however, and its readings do not reflect absorption or scattering by this mirror. This error is believed to be approximately 2-3% overall, but may be greater near oxygen or carbon edges.

The channeltron is an electron amplifier. It is a horn or funnel made from slightly conductive glass and coated with a material that readily releases electrons. The glass horn is biased from a few hundred volts near the opening to over 1 kV at the opposite end. An incoming electron will strike the coated surface of the horn, producing secondary electrons. These electrons are accelerated by the field within channeltron, eventually striking the coated surface and again producing more electrons. The electrons exit the rear of the channeltron and strike a collecting plate. Again, the current produced is measured by an electrometer. The channeltron detects Auger electrons and photoelectrons emitted by a target. The channeltron could be damaged by the high

electron current if it is ever operated while the monochromator is set to zero-order, however.

D.4 Beamline Energy Calibration

The frequent use of 10-1 for high-resolution x-ray absorption spectroscopy (see chapter 6) almost guarantees that the monochromator will be calibrated within 1 eV, which is sufficient for the simple fluorescent spectra in this thesis. We did not have to calibrate 10-1, but did operate the channeltron to determine the calibration technique for future XAS experiments. The monochromator is recalibrated by identifying edge features in the photoelectron emission spectrum detected with the channeltron and entering their correct energies into the monochromator software. Future experiments should carefully select the target material for well-defined and well-documented edge features that bracket the region of interest.

Beamline 1-1 is more general purpose, with simpler control software, and needs to be recalibrated after changing the grating or as a result of operator error (e.g. encountering a physical stop). The "grasshopper" monochromator has only a single degree of freedom, since mechanism links together the tilt of the optical elements to keep the emerging beam at a constant angle as the grating angle is changed. To calibrate the monochromator, the grating must first be set to the zero-order (reflective) position. To locate zero-order, the monochromator is moved to approximately the correct position, either from knowledge of a prior setting or from physical markings on the mechanism. The photodiode is raised into place so that the beam will strike one of the foils (preferably gold). The control software is instructed to scan the monochromator over the range of a few hundred motor steps. This range should include the zero-order position, at

which the photodiode output should peak, and a flash of fluorescent light from the photodiode phosphor should be observed. To complete the calibration, the monochromator is moved to the zero-order position, and the control software's internal variables are reset to those defined to match zero-order. At this point, the beamline should be calibrated to within 1 eV.

Appendix E

The Role of Energy Resolution in Detection Limits

Two radiation peaks of equal intensity are considered to be resolved if they are separated by at least the FWHM of the peaks. But if one of the x-ray sources is much less intense than the other, it may be not detected. An x-ray line (the *analyte*) must produce a statistically significant number of counts above the background counts in an x-ray spectrum to be identified. This is called the *detection limit* of the analyte element. Determination of the intensity of the analyte line requires even more counts, which establishes the *quantitation limit*. An intense line nearby will increase the background count so that the statistical requirements are not met. This is called *interference*. Interference is an important problem in elemental spectral analysis.

There are several ways to deal with interference. [112] Usually, the analyst will adjust the excitation to excite the analyte element more than the background element, or interpose a filter that absorbs the x-rays from the background element more than x-rays from the analyte element. However, this may reduce the overall intensity below practical limits. Often, one simply abandons trying to measure the particular line subject to interference and instead measures another line that is free from interference. This usually means measuring x-rays from a higher-energy shell, e.g. K lines instead of L lines. Analysis of surfaces or small particles requires low-energy excitation, however. Chemical bonding is best studied by measuring the specific x-ray lines with the greatest

sensitivity to bonding. Measuring alternative x-ray lines is not always an option. Another solution is to improve the energy resolution of the detector. Use of a wavelength-dispersive spectrometer may be precluded by cost, efficiency or space. An energy-dispersive solution has been unavailable until the development of cryogenic spectrometers like the microcalorimeter and the STJ.

The proper definition of the detection limit depends on the experimental method. One may, for example, presume the existence of two overlapping x-ray lines and fit them to the line profiles. Detection of the analyte element then depends on the chi-square statistic of the fit. Or, one may declare a peak to be present if the peak to background ratio exceeds a certain value. The dependence of the detection limit on the spectrometer energy resolution is derived below using the second technique.

In the absence of interference, the counts per bin in the analyte line peak must exceed three times the fluctuation in the number of background counts per bin for a 95% confidence interval that the detection is correct, as shown in figure E.1. [112] The background is determined either by the number of counts to either side of the proposed analyte line in the same spectrum, by fitting the background counts in the spectrum to some expected distribution, or by measuring for an equal amount of time a "blank" sample that has been prepared identically, but does not contain the analyte element. If the bin size is allowed to decrease as the peak width ΔE_{FWHM} decreases in direct proportion, then the minimum detectable intensity of the analyte line decreases as $(\Delta E_{FWHM})^{1/2}$. This is the detection limit of the analyte element. The detection limit is also inversely proportional to $t^{1/2}$, so the detection limit for a given measurement is determined by the time available to make the measurement.

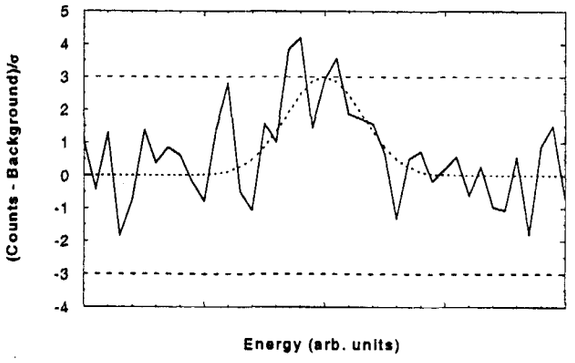

Figure E.1: Simulated spectrum (solid) of a very weak x-ray line (dotted) superimposed on a background. The background fluctuates with standard deviation σ. Almost all of the background fluctuations are contained within 3σ. If the counts in any bin exceed 3σ, there is a 95% probability that a peak is present.

Consider now the presence of an interfering x-ray line. Although most of the counts in the interfering peak are confined within $2\Delta E_{FWHM}$, the tails of the peak may dominate other background counts at the energy of the analyte peak if the interfering line is intense enough. The relative intensities of the analyte element, I_A, and the background element, I_B, at the detection limit is

$$\frac{I_A}{I_B} = \frac{3}{\sqrt{t}} \frac{\sqrt{\int_{z-\delta/2}^{z+\delta/2} f(z')dz'}}{\int_{-\delta/2}^{\delta/2} f(z')dz'}. \qquad \text{E.1}$$

The parameter z is the energy separation of the peaks relative to the HWHM of the spectrometer, $2(E_A-E_B)/\Delta E_{FWHM}$. The parameter δ is the similarly reduced bin size. The function $f(z')$ is the normalized line shape as a function of the reduced energy. The

analyte line must be weak and/or distant relative to the interfering line so that the intensity I_B can be determined. The peak fitting technique must be applied if this condition is not met.

For the weakest analyte intensities, the actual bins that comprise the analyte peak may be combined to form a single bin which is more likely to meet the detection requirement. The optimal bin size is a function of the expected analyte and background intensities, since including bins with very few analyte counts will increase the background fluctuations more than the analyte signal.

First, assume the line shape is that of a Lorentzian function, with slowly decaying tails. The STJ has a slowly decaying tail on the low energy side regardless of the actual x-ray line shape due to quasiparticle and phonon losses. For a Lorentzian line shape,

$$f(z) = \left[\pi\left(z^2 + 1\right)\right]^{-1}. \qquad \text{E.2}$$

Figure E.2 shows the relative intensities at the detection limit as a function of the reduced separation for bin sizes equal to $\Delta E_{FWHM}/2$ and ΔE_{FWHM}. The time dependence has been factored out of the graph. The detection limit decreases linearly as ΔE_{FWHM} for a Lorentzian line shape.

For contrast, consider the Gaussian line shape. The tails of the Gaussian function decay very quickly. As a result, the benefits of even a small improvement in resolving power are very large. The STJ usually has a Gaussian tail on the high-energy side. This makes the STJ spectrometer a particularly useful instrument for detecting chromium, manganese, and iron L lines, as well as the fluorine K line in the presence of an intense oxygen line. The Gaussian line shape function is

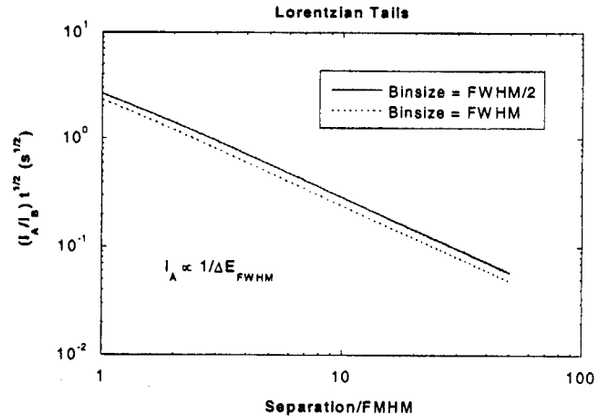

Figure E.2: The analyte intensity detection limit in the present of a Lorentzian tail as a function of peak separation.

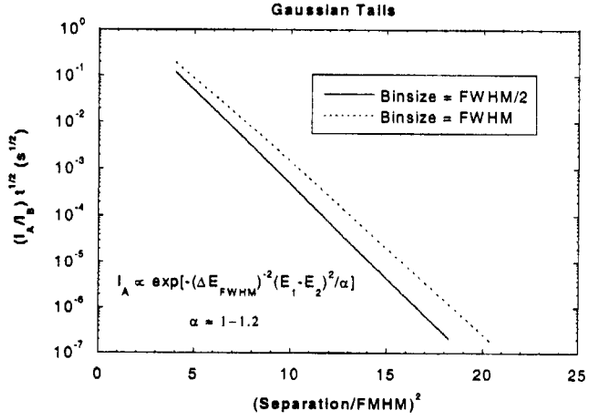

Figure E.3: The analyte intensity detection limit in the present of a Gaussian tail as a function of peak separation.

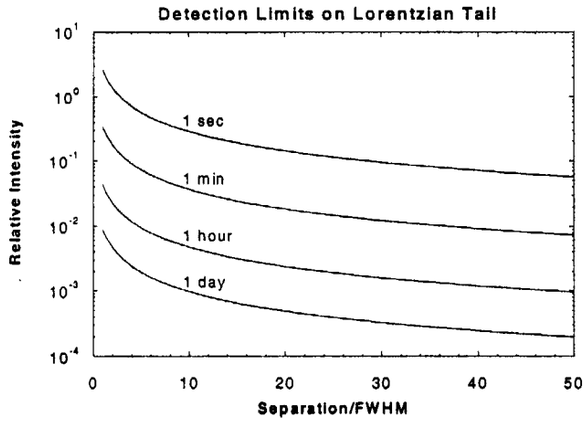

Figure E.4: The analyte intensity detection limit in the presence of a Lorentzian tail as a function of peak separation for specific measurement times.

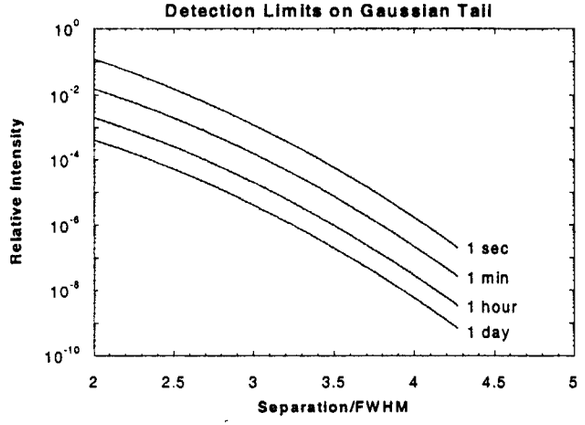

Figure E.5: The analyte intensity detection limit in the presence of a Gaussian tail as a function of peak separation for specific measurement times.

$$f(z) = (\ln 2/\pi)^{1/2} e^{-z^2 \ln 2}. \qquad \text{E.3}$$

Figure E.3 indicates the detection limit for a Gaussian line shape. Figures E.4 and E.5 plot the detection limit for a selection of acquisition times versus the reduced separation on a semi-log scale for Lorentzian and Gaussian line shapes, respectively. Quantitation limits are approximately three times greater than the detection limits. To convert these detection limit intensities into concentrations, one must take into account relative excitation efficiencies, fluorescence efficiencies, multiple absorption and excitation within the sample itself, and the absorption efficiency of the detector.

References

1. Joy, D.C., *Modeling the Energy Dispersive X-ray Detector*, in X-ray spectrometry in electron beam instruments, D.B. Williams, J. Goldstein, and D.E. Newbury, Editors. 1995, Plenum Press: New York. p. 53-66.
2. McCarthy, J.J., *The Effect of Detector Dead Layers on Light Element Detection*, in X-ray spectrometry in electron beam instruments, D.B. Williams, J. Goldstein, and D.E. Newbury, Editors. 1995, Plenum Press: New York. p. 67-82.
3. Labov, S.E., *et al. Assessment of low temperature X-ray detectors. Sixth International Workshop on Low Temperature Detectors.* 1995. Beatenberg/Interlaken, Switzerland, Nucl. Inst. Meth. A, **370**: 65-8.
4. Wollman, D.A., *et al., High-resolution, energy-dispersive microcalorimeter spectrometer for X-ray microanalysis.* Journal of Microscopy, **188**: p. 196-223 (1997).
5. Friedrich, S., *et al. High resolution tunnel junction extreme ultraviolet detectors limited by quasiparticle counting statistics. 1998 Applied Superconductivity Conference.* 1998. Palm Desert, CA, USA, IEEE Trans. Appl. Supercond., **9**(2): 3330-3, (1999).
6. Reed, S.J.B., *Wavelength Dispersive Spectrometry: A Review*, in X-ray spectrometry in electron beam instruments, D.B. Williams, J. Goldstein, and D.E. Newbury, Editors. 1995, Plenum Press: New York. p. 221-238.
7. Irwin, K.D., *et al. A Mo-Cu superconducting transition-edge microcalorimeter with 4.5 eV energy resolution at 6 keV. 8th International Workshop on Low Temperature Detectors.* 1999. Dalfsen, Netherlands, Nucl. Inst. Meth. A, **444**: 184-7.
8. Wollman, D.A., *et al. Superconducting transition-edge-microcalorimeter X-ray spectrometer with 2 eV energy resolution at 1.5 keV. 8th International Workshop on Low Temperature Detectors.* 1999. Dalfsen, Netherlands, Nucl. Inst. Meth. A, **444**: 145-50.
9. Booth, N.E., *Quasiparticle trapping and the quasiparticle multiplier.* Appl. Phys. Lett., **50**(5): p. 293-5 (1987).
10. Mears, C.A., S.E. Labov, and A.T. Barfknecht, *Energy-resolving superconducting X-ray detectors with charge amplification due to multiple quasiparticle tunneling.* Appl. Phys. Lett., **63**(21): p. 2961-3 (1993).
11. Rickayzen, G., *The theory of Bardeen, Cooper, and Schrieffer*, in Superconductivity, R.D. Parks, Editor. 1969, Marcel Dekker Inc: New York, NY, USA. p. 51-112.
12. Chi, C.C. and J. Clarke, *Quasiparticle branch mixing rates in superconducting aluminum.* Phys. Rev. B, **19**(9): p. 4495-509 (1979).

13. Kaplan, S.B., *et al., Quasiparticle and phonon lifetimes in superconductors.* Phys. Rev. B, **14**(11): p. 4854-73 (1976).
14. Barfknecht, A.T., R.C. Ruby, and H.L. Ko. *A simple and robust niobium Josephson junction integrated circuit process. 1990 Applied Superconductivity Conference.* 1990. Snowmass, CO, USA, IEEE Trans. Magn., **27**(2): 3125-8, (1991).
15. Ukibe, M., *et al., Quantitative evaluation of the intrinsic X-ray peak probability of a superconducting tunnel junction with the cascade process model of primary photoelectrons.* Nucl. Inst. Meth. A, **402**(1): p. 95-103 (1998).
16. Chang, J.J. and D.J. Scalapino, *Nonequilibrium superconductivity.* J. Low Temp. Phys., **31**(1-2): p. 1-32 (1978).
17. Zehnder, A., *Response of superconductive films to localized energy deposition.* Phys. Rev. B, **52**(17): p. 12858-66 (1995).
18. Brink, P.L., Ph.D. thesis,*Non-Equilibrium Superconductivity induced by X-ray Photons*, 1995, Oxford: Oxford, UK. p. 240.
19. Gray, K.E., *A superconducting transistor.* Appl. Phys. Lett., **32**(6): p. 392-5 (1978).
20. de Korte, P.A.J. *Superconductive Tunnel Junctions for X-ray Spectroscopy. Proceedings of the SPIE.* 1992, **1743**: 24-35.
21. Martin, J., *et al., Imaging of vortices in superconductors by electron beam scanning.* Appl. Phys. Lett., **73**(3): p. 378-80 (1998).
22. Tinkham, M., Introduction to superconductivity, New York: McGraw Hill, 1996.
23. Ruggiero, S.T. and D.A. Rudman, Superconducting devices, Boston: Academic Press, 1990.
24. Segall, K., personal communication.
25. Friedrich, S., in preparation
26. Fano, U., Phys. Rev., **72**(47): p. 26 (1946).
27. Kurakado, M. and H. Mazaki, *Possibility of a high-resolution nuclear radiation detector using a superconductor. I. Mean energy loss per excess quasiparticle.* Nucl. Inst. Meth. A, **185**(1-3): p. 141-7 (1981).
28. Rando, N., *et al., The properties of niobium superconducting tunneling junctions as X-ray detectors.* Nucl. Inst. Meth. A, **313**(1-2): p. 173-95 (1992).
29. Verhoeve, P. *UV/optical imaging spectroscopy with cryogenic detectors. 8th International Workshop on Low Temperature Detectors.* 1999. Dalfsen, Netherlands, Nucl. Inst. Meth. A, **444**: 435-40, (2000).
30. Hiller, L.J., *Ensemble Current Fluctuations in S-I-S Superconducting Tunnel Junctions Due To Multiple Tunneling of Quasiparticles.* in preparation
31. Jochum, J., *et al., Electronic noise of superconducting tunnel junction detectors.* Nucl. Inst. Meth. A, **338**(2-3): p. 458-66 (1994).
32. van den Berg, M.L., *et al. Inhomogeneous response of superconducting tunnel junctions with a killed electrode for X-ray spectroscopy. 1996 Applied Superconductivity Conference.* 1996. Pittsburgh, PA, USA, IEEE Trans. Appl. Supercond., **7**(2): 3363-6, (1997).
33. Goldie, D.J., *et al., Statistical noise due to tunneling in superconducting tunnel junction detectors.* Appl. Phys. Lett., **64**(23): p. 3169-71 (1994).

34. Booth, N.E., *et al. Superconducting tunnel junctions and quasiparticle trapping. Fifth International Workshop on Low-Temperature Detectors.* 1993. Berkeley, CA, USA, Journal of Low Temperature Physics, **93**: 521-32.
35. Brink, P.L., *et al. The effect of hotspot formation on quasiparticle yields in superconducting aluminium films. Fifth International Workshop on Low-Temperature Detectors.* 1993. Berkeley, CA, USA, Journal of Low Temperature Physics, **93**: 555-60.
36. Le Grand, J.B., *et al., A superconducting tunnel junction X-ray detector with performance limited by statistical effects.* Appl. Phys. Lett., **73**(9): p. 1295-7 (1998).
37. Hettl, P., *et al. High-resolution X-ray spectroscopy with superconducting tunnel junctions. European Conference on Energy Dispersive X-Rays Spectrometry (EDXRS-98).* 1998. Bologna, Italy, X-Ray Spectrometry, **28**: 309-11, (1999).
38. de Korte, P.A.J. *Cryogenic imaging spectrometers for X-ray astronomy. 8th International Workshop on Low Temperature Detectors.* 1999. Dalfsen, Netherlands, Nuc. Inst. Meth. A, **444**: 163-9, (2000).
39. Ovchinnikov, Y.N. and V.Z. Kresin, *Nonstationary state of superconductors: Application to nonequilibrium tunneling detectors.* Phys. Rev. B, **58**(18): p. 12416-21 (1998).
40. Kozorezov, A.G., *et al., Quasiparticle-phonon downconversion in nonequilibrium superconductors.* Phys. Rev. B, **61**(17): p. 11807-19 (2000).
41. Burnell, G., P.A. Warburton, and M.G. Blamire, *Inelastic quasiparticle scattering and multiplication in superconductors.* J. Appl. Phys., **76**(2): p. 1105-10 (1994).
42. Eliashberg, G.M., *Inelastic electron collisions and nonequilibrium stationary states in superconductors.* Zh. Eksp. Teor. Fiz., **61**(3): p. 1254-72 (1971).
43. Scalapino, D.J., *The Electron-Phonon Interaction and Strong-Coupling Superconductors*, in Superconductivity, R.D. Parks, Editor. 1969, M. Dekker: New York. p. 449-560.
44. McMillan, W.L. and J.M. Rowel, *Tunneling and Strong-Coupling Superconductivity*, in Superconductivity, R.D. Parks, Editor. 1969, M. Dekker: New York. p. 561-614.
45. Porter, F.S., *et al. Epitaxial base layer Nb superconducting tunnel junctions with Ta absorbers. Sixth International Workshop on Low Temperature Detectors.* 1995. Beatenberg/Interlaken, Switzerland, Nucl. Inst. Meth. A, **370**: 50-2.
46. Friedrich, S., *et al., Experimental quasiparticle dynamics in a superconducting, imaging X-ray spectrometer.* Appl. Phys. Lett., **71**(26): p. 3901-3 (1997).
47. Verhoeve, P., *et al., High-resolution X-ray spectra measured using tantalum superconducting tunnel junctions.* Appl. Phys. Lett., **72**(25): p. 3359-61 (1998).
48. Pippard, A.B., *Ultrasonic Attenuation in Metals.* Phil. Mag., **46**: p. 1104-1114 (1955).
49. Keck, B. and A. Schmid, *Superconductivity and electron-phonon interaction in impure simple metals.* J. Low Temp. Phys., **24**(5-6): p. 611-29 (1976).
50. Carbotte, J.P., *Properties of boson-exchange superconductors.* Rev. Mod. Phys., **62**(4): p. 1027-157 (1990).
51. Khotkevich, A.V. and I.K. Ianson, Atlas of point contact spectra of electron-phonon interactions in metals, Boston: Kluwer Academic, 1995.

52. Wolf, E.L. and R.J. Noer, *Mcmillan-Rowell tunneling spectroscopy in the Nb-Zr system.* Solid State Communications, **30**(6): p. 391-3 (1979).
53. Knorr, K. and N. Barth, *Electron tunneling into disordered thin films.* J. Low Temp Phys., **4**(5): p. 469-84 (1971).
54. Golubov, A.A., *et al., Quasiparticle lifetimes and tunneling times in a superconductor-insulator-superconductor tunnel junction with spatially inhomogeneous electrodes.* Phys. Rev. B, **49**(18): p. 12953-68 (1994).
55. Golubov, A.A., *et al., Proximity effect in superconductor-insulator-superconductor Josephson tunnel junctions: theory and experiment.* Phys. Rev. B, **51**(2): p. 1073-89 (1995).
56. Friedrich, S., *et al. Line-Splitting in High-Resolution Superconducting Tunnel Junction EUV Detectors. 2000 Applied Superconductivity Conference.* 2000. Virginia Beach, VA, USA, IEEE Trans. Super., in press.
57. Infrared Laboratories, 1808 E. 17th Street, Tucson, AZ 85719-6505, USA, http://www.irlabs.com/.
58. Boll, R., Soft magnetic materials : fundamentals, alloys, properties, products, applications, London ; Philadelphia: Heyden, 1979.
59. Pobell, F., Matter and methods at low temperatures, Berlin ; New York: Springer-Verlag, 1996.
60. Timbie, P.T., G.M. Bernstein, and P.L. Richards. *Development of an adiabatic demagnetization refrigerator for SIRTF. Eighth Space Cryogenic Workshop.* 1989. Pasadena, CA, USA, **30**: 271-5.
61. Goodfellow, Inc., 800 Lancaster Avenue, Berwyn, PA 19312-1780 USA, http://www.goodfellow.com/.
62. Friedrich, S., *et al. Temperature profile of IR blocking windows used in cryogenic X-ray spectrometers. SPIE.* 2000, **4140**: 452-458.
63. Lebow Company, 5960 Mandarin Ave., Goleta, CA 93117, USA, http://www.lebowcompany.com/.
64. CASINO, http://www.gme.usherb.ca/casino/.
65. Luxel Corporation, P.O. Box 1879, Friday Harbor, WA 98250, USA, http://www.luxel.com/.
66. VAT, Inc., 500 West Cummings Park, Suites 5450-5650, Woburn MA 01801,USA, http://www.vat.ch/.
67. X-Ray Interactions with Matter, http://www-cxro.lbl.gov/optical_constants/.
68. Hass, G., ed. Physics of thin films: advances in research and development., Academic Press: San Diego, CA, 1973.
69. Stockwell, W., *et al. Low noise front end electronics for dilution refrigerator experiments. Fifth International Workshop on Low-Temperature Detectors.* 1993. Berkeley, CA, USA, J. Low Temp. Phys., **93**: 755-60, (1993).
70. Szymkowiak, A.E., *et al. Signal processing for microcalorimeters. Fifth International Workshop on Low-Temperature Detectors.* 1993. Berkeley, CA, USA, J. Low Temp. Phys., **93**: 281-5, (1993).
71. Twerenbold, D., *Giaever-type superconducting tunnelling junctions as high-resolution X-ray detectors.* Europhysics Letters, **1**(5): p. 209-14 (1986).
72. Twerenbold, D. and A. Zehnder, *Superconducting Sn/Sn-oxide/Sn tunneling junctions as high resolution X-ray detectors.* J. Appl. Phys., **61**(1): p. 1-7 (1987).

73. Kraus, H., *et al.*, *High-resolution X-ray detection with superconducting tunnel junctions.* Europhysics Letters, **1**(4): p. 161-6 (1986).
74. Luiten, O.J., *et al. Quasiparticle lifetimes and tunnel times in SIS junctions for X-ray spectroscopy. Sixth International Workshop on Low Temperature Detectors.* 1995. Beatenberg/Interlaken, Switzerland, Nucl. Inst. Meth. A, **370**: 72-4.
75. Ohkubo, M., *et al., Asymmetric response of superconducting niobium-tunnel-junction X-ray detectors.* Phys. Rev. B, **54**(13): p. 9484-90 (1996).
76. Ohkubo, M., *et al., Double peak phenomenon in superconducting tunnel junction X-ray detectors.* J. Appl. Phys., **85**(1): p. 595-9 (1999).
77. Blamire, M.G., *Deconvolution of tunneling density of states from superconductor-insulator-superconductor current versus voltage data.* Physica C, **211**(3-4): p. 467-74 (1993).
78. Mears, C.A., S.E. Labov, and A.T. Barfknecht. *High-resolution superconducting X-ray detectors with two aluminum trapping layers. Fifth International Workshop on Low-Temperature Detectors.* 1993. Berkeley, CA, USA, J. Low Temp. Phys., **93**: 561-6, (1993).
79. Peacock, T., *et al., Recent developments in superconducting tunnel junctions for ultraviolet, optical and near infrared astronomy.* Editions de Physique, Astronomy & Astrophysics Supplement Series, **127**(3): p. 497-504 (1998).
80. Twerenbold, D., *Cryogenic particle detectors.* Reports on Progress in Physics, **59**(3): p. 349-426 (1996).
81. Verhoeve, P., *et al., Response of niobium-based superconducting tunnel junctions in the soft-X-ray region 0.15-6.5 keV.* Phys. Rev. B, **53**(2): p. 809-17 (1996).
82. Rando, N., *et al., Response linearity of Nb tunnel junction detectors for photon energies from 1.5 to 6.4 keV.* J. Appl. Phys., **76**(4): p. 2490-3 (1994).
83. Poelaert, A., *et al., Strong nonlinear response of superconducting tunnel junctions due to localized traps.* Phys. Rev. Lett., **82**(6): p. 1257-60 (1999).
84. Labov, S.E., *et al. Low-energy response of superconducting tunnel junction X-ray spectrometers. 1994 Applied Superconductivity Conference.* 1994. Boston, MA, USA, IEEE Trans. Appl. Supercond., **5**(2): 3034-7, (1995).
85. Mears, C.A., *et al. High-resolution superconducting X-ray spectrometers with aluminum trapping layers of different thicknesses. 1994 Applied Superconductivity Conference.* 1994. Boston, MA, USA, IEEE Trans. Appl. Supercond., **5**(2): 3069-72, (1995).
86. Poelaert, A., Ph.D. thesis,*Superconducting tunnel junctions used as photon detectors,* 1999, University of Twente: Twente, NL. p. 162.
87. Friedrich, S., *et al. Fiske modes in superconducting tunnel junction detectors. 8th International Workshop on Low Temperature Detectors.* 1999. Dalfsen, Netherlands, Nucl. Inst. Meth. A, **444**: 151-5, (2000).
88. Galeazzi, M., *et al. An Electronic Feedback System for Improving the Counting Rate of Cryogenic Thermal Detectors. Seventh International Workshop on Low Temperature Detectors.* 1997. Munich, DE. Max Planck Institute for Physics: Munich. p. E4, (1997).
89. Nam, S.W., *et al. A new biasing technique for transition edge sensors with electrothermal feedback. 1998 Applied Superconductivity Conference.* 1998. Palm Desert, CA, USA, EEE Trans. Appl. Supercond., **9**(2): 4209-12, (1999).

90. Xia, B., *et al., Human Ferredoxin - Overproduction in Escherichia Coli, Reconstitution in Vitro, and Spectroscopic Studies of Iron-Sulfur Cluster Ligand Cystein-to-Serine Mutants.* Biochemistry, **35**(29): p. 9488-9495 (1996).
91. Xia, B., B.F. Volkman, and J.L. Markley, *Evidence for oxidation-state-dependent conformational changes in human ferredoxin from multinuclear, multidimensional NMR spectroscopy.* Biochemistry, **37**(11): p. 3965-3973 (1998).
92. Lancaster, J.R., The Bioinorganic chemistry of nickel, New York, N.Y.: VCH, 1988.
93. Volbeda, A., *et al., Crystal structure of the nickel-iron hydrogenase from Desulfovibrio gigas.* Nature, **373**(6515): p. 580-7 (1995).
94. Jackson, J.D., Classical electrodynamics, New York: Wiley, 1975.
95. Hoffman, D.M., B. Singh, and J.H. Thomas, eds. Handbook of vacuum science and technology., Academic Press: San Diego, CA, 1998.
96. Hagmann, C., D.J. Benford, and P.L. Richards, *Paramagnetic salt pill design for magnetic refrigerators used in space applications.* Cryogenics, **34**(3): p. 213-19 (1994).
97. Wilson, G.W. and P.T. Timbie, *Construction techniques for adiabatic demagnetization refrigerators using ferric ammonium alum.* Cryogenics, **39**(4): p. 319-22 (1999).
98. Kaplan, S.B., *Acoustic matching of superconducting films to substrates.* J. Low Temp. Phys., **37**(3-4): p. 343-65 (1979).
99. Soukoulis, C.M. and D.A. Papaconstantopoulos, *Effects of disorder on properties of A15 materials.* Phys. Rev. B, **26**(7): p. 3673-81 (1982).
100. Kirtley, J.R., *et al., Quasiparticle energy distribution and relaxation times in a tunnel-injected superconductor.* Phys. Rev. B, **22**(3): p. 1218-32 (1980).
101. Lide, D.R., CRC handbook of chemistry and physics, Boca Raton, FL.: CRC Press, 1990.
102. Weber, H.W., *et al., Anisotropy effects in superconducting niobium.* Phys. Rev. B, **44**(14): p. 7585-600 (1991).
103. Kittel, C., Introduction to solid state physics, New York: Wiley, 1986.
104. Ginsburg, D.M. and L.C. Hebel, *Nonequilibrium properties: comparison of experimental results with predictions of the BCS theory,* in Superconductivity, R.D. Parks, Editor. 1969, M. Dekker: New York. p. 193-257.
105. Gray, K.E., *Steady state measurements of the quasiparticle lifetime in superconducting aluminium.* J. Phys. F, **1**(3): p. 290-308 (1971).
106. Bruijn, M., personal communication, 17 November 1995.
107. Golubov, A.A. and E.P. Houwman, *Quasiparticle relaxation rates in a spatially inhomogeneous superconductor.* Physica C, **205**(1-2): p. 147-53 (1993).
108. Poelaert, A., personal communication, 1 June 1999.
109. Research Systems, Inc., 4990 Pearl East Circle, Boulder, CO 80301, USA, http://www.rsinc.com.
110. Press, W.H., Numerical recipes in FORTRAN: the art of scientific computing, 2nd ed, New York: Cambridge University Press. 963, 1992.
111. Samedov, V.V. *Superconducting tunnel junction signal caused by quasielectron multitunneling. 8th International Workshop on Low Temperature Detectors.* 1999. Dalfsen, Netherlands, Nucl. Inst. Meth. A, **444**: 59-63, (2000).

112. Bertin, E.P., Principles and practice of X-ray spectrometric analysis, New York: Plenum Press, 1975.